Imperial College London

# Sensorisation of a Novel Biologically Inspired Flexible Needle

Vani Virdyawan

Department of Mechanical Engineering
Imperial College London

September 2018

This thesis is submitted for the degree of Doctor of Philosophy at Imperial College London

## Declaration of Originality

I, Vani Virdyawan, hereby confirm that the works presented in this thesis are my own, except where stated otherwise by reference or acknowledgement.

Vani Virdyawan

8th September 2018

## Copyright Declaration

The copyright of this thesis rests with the author and is made available under a Creative Commons Attribution Non-Commercial No Derivatives licence. Researchers are free to copy, distribute or transmit the thesis on the condition that they attribute it, that they do not use it for commercial purposes and that they do not alter, transform or build upon it. For any reuse or redistribution, researchers must make clear to others the licence terms of this work.

# Abstract

Percutaneous interventions are commonly performed during minimally invasive brain surgery, where a straight rigid instrument is inserted through a small incision to access a deep lesion in the brain. Puncturing a vessel during this procedure can be a life-threatening complication. Embedding a forward-looking sensor in a rigid needle has been proposed to tackle this problem; however, using a rigid needle, the procedure needs to be interrupted if a vessel is detected. Steerable needle technology could be used to avoid obstacles, such as blood vessels, due to its ability to follow curvilinear paths, but research to date was lacking in this respect.

This thesis aims to investigate the deployment of forward-looking sensors for vessel detection in a steerable needle. The needle itself is based on a bioinspired programmable bevel-tip needle (PBN), a multi-segment design featuring four hollow working channels. In this thesis, laser Doppler flowmetry (LDF) is initially characterised to ensure that the sensor fulfils the minimum requirements for it to be used in conjunction with the needle.

Subsequently, vessel reconstruction algorithms are proposed. To determine the axial and off-axis position of the vessel with respect to the probe, successive measurements of the LDF sensor are used. Ideally, full knowledge of the vessel orientation is required to execute an avoidance strategy. Using two LDF probes and a novel signal processing method described in this thesis, the predicted possible vessel orientations can be reduced to four, a setup which is explored here to demonstrate viable obstacle detection with only partial sensor information.

Relative measurements from four LDF sensors are also explored to classify possible vessel orientations in full and without ambiguity, but under the assumption that the vessel is perpendicular to the needle insertion axis. Experimental results on a synthetic grey matter phantom are presented, which confirm these findings.

To release the perpendicularity assumption, the thesis concludes with the description of a machine learning technique based on a Long Short-term memory network, which enables a vessel's spatial position, cross-sectional diameter and full pose to be predicted with sub-millimetre accuracy. Simulated and *in-vitro* examinations of vessel detection with this approach are used to demonstrate effective predictive ability. Collectively, these results demonstrate that the proposed steerable needle sensorisation is viable and could lead to improved safety during robotic assisted needle steering interventions.

# Acknowledgements

My research and this thesis would not be finished without the support that I received during my PhD in the Mechatronics in Medicine Lab (MIM LAB) at Imperial College London. Therefore, I would like to express my sincere gratitude to:

- My supervisor, Ferdinando Rodriguez y Baena, for his guidance in all the time of research and writing this thesis. He encouraged me to be an independent researcher and to learn new skills. I also really appreciated his advice for me as a new father.
- Matthew Oldfield who helped me to make the detail of my research during the first half of my Phd, Josh Giles and Richard J van Arkel, who helped me to develop the idea of my first conference paper, Riccardo Secoli, who helped me to use the steerable needle actuation box, Stefano Galvan who helped me to set-up the machine learning software, and Phil Wilson who helped to manufacture my set-up.
- Michael Rau and Oxford Optronics that gave the loan of the laser Doppler monitor and advice relating to its use.
- Past and present MIMLAB members who created an excellent research environment: Thomas Watts, Arnau Garriga Casanovas, He Liu, Hisham Iqbal, Wenbo Zhan, Fabio Tatti, William Blyth, Alexander Leibinger, Chris Burrows, Stuart Bowyer, Marlene Pinzi, and Eloise Matheson.
- Directorate General Of Higher Education of Indonesia that gave me the scholarship to pursue my PhD, and European Union's Horizon 2020 research and innovation program EDEN2020 that funded my research.
- My parents, Purwono Subagyo and Sri Haryati, and families who supported and prayed for me from the other side of the world.
- Finally, my beloved wife, Qorry Aina, who always accompanies me and shares my aspiration. And also, my dear daughter, Alisha Nalavary Virdyawan, who was born at the beginning of my fourth year, who always cheers me up with her gentle smile.

# Contents

**Declaration of Originality** **3**

**Copyright Declaration** **4**

**Abstract** **5**

**Acknowledgements** **6**

**Contents** **7**

**List of Figures** **11**

**List of Tables** **22**

**1 Introduction** **25**

1.1 Motivation . . . . . 25

1.2 Thesis Aim and Objectives . . . . . 28

1.3 Thesis Contributions . . . . . 29

1.4 Thesis Structure . . . . . 31

**2 Literature Review** **33**

2.1 Introduction . . . 33

2.2 Percutaneous Intervention in Brain Surgery . . . 34

2.3 Sensors for Vessel Detection in Brain Surgery . . . 35

2.4 Steerable Needle Systems . . . 40

2.5 Image Guidance and Sensorisation of Steerable Needles . . . 46

2.5.1 Image Guidance . . . 47

2.5.2 Embedded Sensors . . . 50

2.6 Conclusion . . . 53

**3 Manufacturing of a Programmable Bevel-Tip Needle** **58**

3.1 Introduction . . . 58

3.2 Additive Manufacturing of a High Aspect Ratio Part . . . 59

3.2.1 Related Works . . . 60

3.2.2 Material and Methods . . . 61

3.2.3 Results and Discussion . . . 64

3.3 Manufacturing Process for Polymer PBNs . . . 66

3.3.1 Extrusion Process for Polymeric PBNs . . . 67

3.3.2 Fixture Design . . . 70

3.3.3 Results and Discussion . . . 71

3.4 Conclusion . . . 73

**4 Laser Doppler Flowmetry for Blood Vessel Detection with a Programmable Bevel Tip Needle 74**

4.1 Introduction . . . 74

4.2 Single Channel Laser Doppler Flowmetry Characterisation . . . 75

4.2.1 Materials and Methods . . . 76

4.2.2 Characterisation Results . . . 79

4.3 Vessel position and orientation prediction - Feasibility Study . . . 81

4.3.1 Materials and Methods . . . 82

4.3.2 Vessel Pose Prediction Results . . . 87

4.4 Discussion . . . 91

4.5 Conclusion . . . 94

**5 Multiple Forward Looking Sensors to Predict Vessel Pose 95**

5.1 Introduction . . . 95

5.2 A Four-Channel Laser Doppler Flowmetry Characterisation . . . 97

5.2.1 Material and Methods . . . 97

5.2.2 Results . . . 99

5.3 Vessel Pose Classification . . . 102

5.3.1 Materials and Methods . . . 102

5.3.2 Results . . . 106

5.3.3 Sensitivity Analysis . . . 107

5.4 Discussion . . . 111

5.5 Conclusion . . . 113

**6 A Long Short-Term Memory Network to Predict Vessel Pose in a Steerable Needle 114**

6.1 Introduction . . . 114

6.2 Single Probe Vessel Detection . . . 115

6.2.1 Materials and Methods . . . 115

6.2.2 Results . . . 122

6.3 Vessel Detection with Multiple Probes . . . 126

6.3.1 Materials and Methods . . . 127

6.3.2 Results . . . 133

6.4 Discussion . . . 137

6.5 Conclusion . . . 139

**7 Conclusion and Future Work 140**

7.1 Conclusion . . . 140

7.2 Limitations and Future Work . . . 144

**Bibliography 147**

**A Obtained Permission 168**

# List of Figures

2.1 a) A single crystal ultrasound that was implemented as a forward viewing probe (top) and side viewing probe (bottom). Reprinted, with permission, from McPhillips et al. (2015) ©2015 IEEE. b) A schematic diagram of a matrix array ultrasound probe with its pyramid shape detection volume. The inset in the figure shows the 6.48 × 6.48 mm matrix array probe. Reprinted, with permission, from Light et al. (2007) ©2007 IEEE . . . . . 36

2.2 Schematic of the forward viewing OCT probe using a long thin GRIN rod lens with a galvanometer scanning mirror to acquire B-scan images. FC: fibre coupler, PC: polarization controller, C: collimator, BD: balanced detector, MZI: Mach-Zehnder interferometer, DAQ: data acquisition board, M: mirror, GSM: galvanometer scanning mirror, O: objective lens, AS: alignment stages, GL: GRIN lens needle. Reprinted, with permission, from Liang et al. (2011) ©2011 Optical Society of America . . . . . 37

2.3 Example of perfusion value measurements using an LDF probe during a DBS implantation procedure to the left and right globus pallidus internus (GPi). Very high blood flow values (in this case >300 AU) were observed during the insertion to the right GPi target. Reprinted, with permission, from Wårdell et al. (2016) ©2016 S. Karger AG . . . . . 38

2.4 a) Schematic diagram of the remission spectroscopy probe inside a biopsy needle. The tip of the illumination (①) and the collection (②) fibre were grounded with a 45° angle and coated with aluminium to perform side viewing (A1). Reprinted, with permission, from Markwardt et al. (2017) ©2016 John Wiley and Sons. b) The enlarged view of the interstitial Optical Tomography (iOT) probe that shows its illumination and detection fibres. Reprinted, with permission, from Goyette et al. (2015) ©2015 Optical Society of America . . . . . 40

2.5 Illustration of a needle steering using base manipulation method. Needle tip position and orientation are controlled by changing the orientation and the lateral position of the needle base. Adapted with permission from Springer Nature, (DiMaio & Salcudean 2003), ©2003 . . . . . 42

2.6 (a) Lateral component of asymmetric tissue reaction force at a bevel-tipped needle (F) results in needle bending (adapted with permission from (van de Berg, van Gerwen, Dankelman & van den Dobbelsteen 2015) ©2015 IEEE), and (b) The needle curvature can be controlled by changing the duty cycle of the spinning needle (reprinted with permission from (Engh, Podnar, Khoo & Riviere 2006) ©2006 IEEE) . . . . . 44

2.7 The tip force is symmetric where the segments are aligned so that there is no bending in the ovipositor, the asymmetric force where the ovipositor has an offset produces bending . . . . . 45

2.8 The 4 mm PBN that was manufactured using additive manufacturing with rubber like materials. Each needle segment has soft (black) and rigid (black) section, as described in (Burrows et al. 2017) . . . . . 46

2.9 (a) The PBN with all of the segments aligned, and (b) with offsets introduced into the needle. (c) Cross section of the needle, which has a diameter of 2.5 mm and four, 0.3 mm OD working channels. Steering direction can be controlled by changing leading segment. . . . . 46

2.10 Illustration of a needle embedded with three optical fibres. In each fibre, fibre Bragg grating sensors were located at three axial positions: 11, 26, and 70 mm from the tip of the needle. Reprinted, with permission, from Li, Li, Gonenc, Duan & Iordachita (2017) ©2016 John Wiley and Sons . . . . . 52

3.1 A CAD drawing of warping benchmark part for building the high aspect ratio surgical needle and the cross section of the overhang structure . . . . . 62

3.2 Warping measurement method using a calibrated microscope of an overhang structure with more than 100 $\mu$m warping. The dash line shows the shape of the overhang structure if there is no warping . . . . . 62

3.3 The cross section image of an overhang structure taken by a measurement microscope (left) and its circularity measurement using the MZC method (right) . 63

3.4 The drawing of the 2 part PBN. In addition to the central needle, note that each segment has a "wing" so that it can be pushed or pulled using a nitinol wire 1.6 mm in diameter connected to an actuation box . . . . . 64

3.5 A two part needle with 70 mm in length has been built using the build strategy described in this Chapter . . . . . 65

3.6 Circularity measurements boxplot of 45° and 90° build angle . . . . . 66

3.7 Schematic diagram of the extrusion process to manufacture the PBN. Image Courtesy: XOGRAPH, ltd. . . . . 68

3.8 a) The extrusion die that was attached into the extruder head. The red arrow shows the mandrel to produce two working channels in the PBN segment; b) A 2.5 mm colour coded PBN with two working channels in each segment. Image courtesy: XOGRAPH ltd. . . . . 69

3.9 The PBN prototypes evolution from a 12 mm outer diameter needle manufactured using a rapid prototyping process (left) to a 2.5 mm outer diameter colour-code needle manufactured using an extrusion process (right) . . . . . 69

3.10 a) The shape of the tip of the needle; b) The cross section of the needle with the projection of the cutting direction $A_c$ and $B_c$ in the $xy$-plane . . . . . 71

3.11 a) The simplification of the segment's external shape used to manufacture the fixture; b) the manufactured fixture of the 4 mm PBN segment with a 45° bevel tip angle . . . . . 71

3.12 Measurements of the a) fixture angle, and b) bevel-tip angle using optical microscope (Zeiss - Axio Icc.1). The angle of the fixture is 45.8° and the bevel tip angle is 45.7° . . . . . 72

4.1 a) A bare-fibre type probe (NX-BF/F, Oxford Optronix, Abingdon, UK) with its corresponding cross-section (inset); b) LDF probe schematic diagram. Light is delivered through an illumination fiber, scattered in the substrate and collected using a collection fibre. A:Illumination fiber, B: Collection fiber, C: Scattered light, D: substrate . . . . . 76

4.2 Minimum requirements for the detection range of the probe that is used for vessel detection in the PBN. A: the PBN, B: Optical fibres, C: Blood vessel . . . . . 77

4.3 Compression tests results of phantom with 3g/L $Ti0_2$ (red dash-dot line) and without $TiO_2$ (solid black line) . . . . . 78

4.4 Schematic diagram of the characterization procedure for: a) depth detection range, b) off-axis detection range. A: LDF probe, B: blood vessel phantom, C:direction of movement, $\theta_v$: the angle of the vessel phantom . . . . . 78

4.5 Experimental configuration for laser Doppler characterization of vessel flow in a brain phantom, using a commercially available laser Doppler system (OxyFlo$^{TM}$, Oxford Optronix, Abingdon, UK). A: LDF system, B: perfusion pump, C: LDF probe, D: linear stage, E: brain phantom, F: vessel phantom . . . . . 79

4.6 Mean and standard deviations of perfusion value against capillary depth for three different flow velocities, the dash-dot line is the threshold value . . . . . 80

4.7 Mean and standard deviations for off-axis perfusion value when measured laterally across the capillary at different depths, the dash-dot line is the threshold value . . . . . 81

4.8 (a) A schematic diagram of vessel detection experiments with a global coordinate system. (b) The position of two laser Doppler probes in the PBN with the definitions and terminology used for predicting the vessel; three local coordinates at the tip of the needle ($x_n$, $y_n$, $z_n$), the bottom probe ($x_{pb}$, $y_{pb}$, $z_{pb}$), and the top probe ($x_{pt}$, $y_{pt}$, $z_{pt}$) were used. A: The PBN, B: vessel phantom, C:tissue phantom, D: Gelatin box, LD: laser Doppler probe, TO: tip off-axis distance, TP: top probe off-axis distance, LP: bottom probe off-axis distance . . . . . 83

4.9 Insertion configuration for vessel prediction experiments, the LDF system used here was the same single channel LDF system as in Section 4.2. A: LDF system, B: linear stage, C: the PBN, D: syringe pump, E: brain phantom, F: vessel phantom 83

4.10 2D map of the perfusion value generated using (4.1) . . . . . 85

4.11 Contour plot of the LDF perfusion value measurements, each line showing depth and off-axis positions for the same perfusion value . . . . . 86

4.12 Mean and standard deviation of perfusion values for the top (asterisk) and bottom probes (circle), from 3.00 mm away from the surface of the needle, with 0.50 mm increments at a) -0.36 mm, b) -0.18 mm, c) 0.00 mm, d) 0.18 mm, and e) 0.36 mm tip off-axis position. The inset in each figure shows the position of the vessel. The red circle in the inset represents the top probe, and the blue circle represents the bottom probe. The experiment set-up is shown in Figure 4.9 . . 88

4.13 a) The mean perfusion value from the bottom probe (Figure 4.12c). The possible vessel position at point A, B, and C is shown in b), c), and d) respectively, the dash-dot line is the insertion axis of the laser Doppler probe. The circles in d) show the possible vessel positions after three successive measurements . . . . . 89

4.14 Four possible tube position and orientation reconstructions (three dash-dot lines and one solid line) located on the plane perpendicular to the insertion axis (parallel to the $xy$-plane) using two detection circle methods. The solid line is the most parallel line to the ground truth that is used to quantify the vessel reconstruction. Inset shows the intersection of the line at $x$ = -0.02. O: tip of the PBN, A: position of the bottom probe, B: position of the top probe, C1: the detection circle of the bottom probe, C2: the detection circle of the top probe . 90

5.1 Left: scaled-up prototype of the PBN used here (B) and laser Doppler probes embedded within the needle (A). The needle has an outer diameter of 4.0 mm, with 4 working channels, each with a diameter of 0.6 mm (right) . . . . . 97

5.2 Experimental set-up used for LDF characterisation, the vessel and grey matter phantom were placed on top of a 2 DOF linear stage that can be moved in the $x_{st}$ and $y_{st}$ directions . . . . . 99

5.3 Characterization results: a) perfusion value for different flow velocities in a vessel with 0.6 mm and 0.3 mm inner diameter; b) perfusion value for 20 mm/s flow velocity in grey matter phantom and white matter phantom, with vessel placed at variable axial depths; c) perfusion value for 20 mm/s flow velocity in grey matter phantom and white matter phantom, with vessel placed at different off-axis distances . . . . . 100

5.4 Characterization results: a) perfusion value for constant insertion speed of 0.2 mm/s and 0.4 mm/s; b) mean and standard deviation of perfusion values obtained for 0.2 mm/s, 0.4 mm/s, 0.6 mm/s, and 1.0 mm/s insertion speeds; c) constant insertion speed of 0.2 mm/s, with a vessel detected at time 155 s, at which point the insertion was stopped. The distance from the probe to the vessel was $\approx$ 2 mm. The perfusion value drop was $\approx$ 200 AU which, as expected, is equal to the perfusion value offset for 0.2 mm/s . . . . . 101

5.5 a) Representation of a vessel (red line approximation) detected by four probes ($P_1$, $P_2$, $P_3$, $P_4$); b) Boundary of the 24 classes as a function of two parameters, $\theta$ and $c$ . . . . . 104

5.6 a) A schematic diagram of vessel detection experiments with the needle coordinate system ($x$, $y$, $z$) located at the tip of the needle. The needle can be rotated with respect to its axis ($\theta_{rm}$) to change the $\theta$ value. Moving the sample box in $y_{st}$ direction changes the $c$ value. By moving the needle in the direction of $x_{st}$, more than one insertion can be done in a sample. b) Experimental set-up used for vessel classification. The vessel and grey matter phantom were placed on top of a 2 degree of freedom (DOF) linear stage that can be moved in the $x_{st}$ and $y_{st}$ directions. The PBN was mounted on a rotation mount fixed to a three DOF linear stage . . . . . 106

5.7 Perfusion values of four probes during insertion of the needle approaching a 0.6 mm vessel at different depths, starting at $z = -1.80$ mm with the following values for $c$: a) $c = 0.40$ mm, b) $c = 0.20$ mm, c) $c = 0.00$ mm, d) $c =$ -0.20 mm, and e) $c =$ -0.40 mm. Possible vessel poses predicted using relative measurement of four probes: f) $c = 0.40$ mm, g) $c = 0.20$ mm, h) $c = 0.00$ mm, i) $c = -0.20$ mm, and j) $c = -0.40$ mm. Predictions were made at $z = -0.60$ mm. Grey area: predicted vessel pose, red line: vessel pose, $P_1$: probe 1, $P_2$: probe 2, $P_3$: probe 3, $P_4$: probe 4, $O$: tip of the needle . . . . . 108

5.8 a) Perfusion values of four probes during insertion of the needle approaching a 0.3 mm vessel at different depths, starting at $z = -0.90$ mm with $c = 0$ and $\theta = 0°$. b) Possible vessel poses predicted using the algorithm developed in this section. Prediction was made at $z = -0.30$ mm. Grey area: predicted vessel pose, red line: vessel pose, $P_1$: probe 1, $P_2$: probe 2, $P_3$: probe 3, $P_4$: probe 4, $O$: tip of the needle . . . . . 108

5.9 Representation of a vessel (red line approximation) with a tilt angle $\alpha$. The axial distance from $P_2$ to the vessel ($d_{ax2}$) is not equal to the axial distance from $P_3$ to the vessel ($d_{ax3}$). The projection of the vessel in the $xy$-plane has an angle of $\theta$ with respect to the $x$-axis. . . . . 109

5.10 a) Comparison of the normalized perfusion value between experiments (dash line) and simulation (dash-dot line) for three depth position (0.3, 0.9 and 1.5 mm). b) The mean normalized perfusion value of simulation results for various optical properties ($\mu_s'$: 0.55 - 0.95 $mm^{-1}$ and $\mu_a$: 0.0053 - 0.028$mm^{-1}$) for three depth position (0.3, 0.9 and 1.5 mm). The error bar shows the maximum and the minimum perfusion value, c) colour-map of the maximum tilt angle that can still be predicted correctly by the method described in this chapter. . . . . 110

6.1 Axial distance $d_{ax}$ and off-axis distance $d$ from the tip of the LDF probe to a vessel with a certain diameter ($\varnothing$) . . . . . 115

6.2 Schematic diagram of the detector that was used in the simulation. The detector was modelled as a ring detector between two red-dashed circles . . . . . 117

6.3 Detection area of the laser probe for each vessel diameter. Left: 0.3 mm diameter vessel, middle: 0.6 mm diameter vessel, right: 0.9 mm diameter vessel . . . . . 118

6.4 The dash-lines represent the thirty possible positions of the chosen class during the simulation. If $d_{ax} \geq \frac{\varnothing}{2} + 0.3$ the probe is moved forward. At the first instance where $d_{ax} < \frac{\varnothing}{2} + 0.3$ (Point Q), three possible probe movements are chosen until the $30^{th}$ position is reached: forwards (top), backwards (middle), and stop (bottom). Yellow squares represent probe positions while the probe is moved forward, green squares while the probe is moved backward, and the blue square while the probe is stopped. It should be noted that the off-axis distance of a simulation run is constant for all measurement points . . . . . 121

6.5 Distribution of the classes shows imbalance. In this histogram, the frequency of the no-detection class is not included, and has a value of ≈ 57,000 . . . . . 121

6.6 a) Comparison of the axial normalised perfusion value between experiments (dash-dot line) and simulation (dash-line) at 0 mm off-axis position; b) comparison of the off-axis normalised perfusion value between experiments (dash-dot line) and simulation (dash-line) at three axial distances: 0.75 mm, 1.35 mm, and 1.95 mm; c) The error-bar shows the maximum and minimum perfusion values for each vessel diameter at 0.75 mm axial distance, with varying tissue optical properties and flow velocity rates . . . . . 123

6.7 Network performance evaluation using Recall, Precision and $F_1$-score as a function of $\gamma$, with corresponding false positive and false negative values . . . . . 124

6.8 a) An example of insertion experiments with off-axis distance at 0.67 mm, which was used to evaluate the performance of the trained network; b) The prediction probability at instances A-G for three vessel diameters: 0.3 mm (top), 0.6 mm (middle), and 0.9 mm (bottom). The total probability of the three rows in each column added with the probability of no-detection is equal to 1. At the end of the insertion the actual position of the vessel was at 0.67 mm off-axis distance and 0.75 mm axial distance . . . . . 126

6.9 The red-dash line represents the detection range of the probe in the $x_p y_p$-plane. There are two coordinate systems shown, the needle coordinate system $(x_n, y_n, z_n)$ and probe coordinate system $(x_p, y_p, z_p)$. Both of the coordinate systems are located at the tip of the needle. with the second rotated $-14.8°$ with respect to the first. $P_1$: probe 1; $P_2$: probe 2; $P_3$: probe 3; $P_4$: probe 4; $d_{pn}$: distance from the probe to the $y_p$-axis; $det_{ax}$: maximum off-axis detection range at a certain axial distance; $dr_{ax}$: detection range for the four probes . . . . . 128

6.10 Three-dimensional representation of a vessel (red line). The vessel was defined in the vessel coordinate system $(x_v, y_v, z_v)$ with an angle of $\phi$ with respect to the $z_v$-axis. The projection of the vessel onto the $x_v y_v$-plane has an angle of $\theta$. The vessel coordinate system was located randomly in the global coordinate system $(x, y, z)$. Probe $n$ $(P_n)$ is represented as a green line in the figure. The probe was located in a fixed position with respect to the probe coordinate system $(x_p, y_p, z_p)$. During insertion, the probe coordinate system was moved along the $z$-axis. At the beginning of the insertion, the probe coordinate system was located at $x = 0, y = 0, z = 0$. Measures for the axial $(d_{ax})$ and off-axis $(d)$ distances were computed using the line to line distance . . . . . 132

6.11 Multilabel network performance evaluation using $F_1$, Precision, Recall, and Hamming Loss as a function of $\gamma$ . . . . . 134

6.12 a) An example of simulated perfusion values for a vessel located at $x = 0, y = 0.8, z = -1.8$, with $\theta = 120°$ and $\phi = 75°$; b) Projection of the actual (red-circles) and predicted (blue-squares) vessel area inside the detection area of the sensors on the $x_p y_p$-plane (top) and on the $x_p z_p$-plane (bottom), with its corresponding perfusion values (Point $A_1$ - $E_1$) . . . . . 135

6.13 a) Example perfusion values from the insertion experiments. The measurements were taken while the needle was located at $z = 0$ to $z = -1.8$, in $-0.3$ decrements; b) Projection of the actual (red-circles) and predicted (blue-squares) vessel area inside the detection area of the sensors on the $x_p y_p$-plane (top) and on the $x_p z_p$-plane (bottom), with its corresponding perfusion values (Point $A_0$ - $G_0$) . . . . . 136

# List of Tables

2.1 Rigid needles sensorisation. LDF: laser Doppler flowmetry; OCT: Optical Coherence Tomography; CGD: Coherence-gated Doppler; US: ultrasound . . . . . 40

2.2 Steerable needle sensorisation; US: ultrasound, EM: Electromagnetic Tracker; FBG: Fibre Bragg Grating; Cam: Camera; F/T: Force and Torque Sensor; Oth: Other sensing modalities . . . . . 55

2.2 Steerable needle sensorisation; US: ultrasound, EM: Electromagnetic Tracker; FBG: Fibre Bragg Grating; Cam: Camera; F/T: Force and Torque Sensor; Oth: Other sensing modalities . . . . . 56

2.2 Steerable needle sensorisation; US: ultrasound, EM: Electromagnetic Tracker; FBG: Fibre Bragg Grating; Cam: Camera; F/T: Force and Torque Sensor; Oth: Other sensing modalities . . . . . 57

3.1 The warping of the benchmark part in a different overhang lengths and build angles . . . . . 67

3.2 The average of cross section circularity for each build angle . . . . . 67

3.3 The comparison between the designed bevel-tip angle and the manufactured bevel-tip angle . . . . . 72

4.1 Paremeters of the insertion experiments . . . . . 82

4.2 Parameters used in equation 4.1 . . . . . 85

4.3 Mean, standard deviation, and RMS error of the constructed vessel . . . . . 91

5.1 Position of laser Doppler probes . . . . . 103

5.2 Pairs of $\theta$ and $c$ values that were used during the experiments and the prediction error . . . . . 107

6.1 Confusion matrix to find the optimise $\gamma$ value. $t_n$: true negative, $t_p$: true positive, $f_p$: false positive, $f_n$: false negative . . . . . 122

6.2 Confusion matrix of the prediction using test data set generated from simulation, ND: No-detection . . . . . 125

6.3 Confusion matrix of the prediction using data from insertion experiments, ND: No-detection . . . . . 125

6.4 Position of laser Doppler probes in the needle coordinate system $(x_n, y_n, z_n)$ and in the probe coordinate system $(x_p, y_p, z_p)$ . . . . . 129

# Chapter 1

# Introduction

## 1.1 Motivation

Brain disorders are a major public health problem. They cost the European Economy approximately 35% of the overall disease burden, where one-third of all European citizens have had at least one brain disorder (Sobocki et al. 2006). Brain tumours, as an example of a brain disease, are comparatively rare, but very costly per case (DiLuca & Olesen 2014). Therefore, to tackle this challenge, technology development regarding diagnosis, prevention, and treatment of brain disease is required (DiLuca & Olesen 2014).

Minimally invasive surgery (MIS) has been used as a method for disease diagnosis and treatment in a variety of human tissues, such as in the brain, liver, and gastrointestinal tract (Proctor & Black 2005, Gillams 2005, Fuchs 2002). MIS can be defined as a surgical procedure that is less invasive than traditional open surgery (Goldberg et al. 2005). Compared to open surgery, this procedure offers several benefits to the patient, such as reduced trauma and a faster recovery time (Westebring-Van Der Putten et al. 2008). The use of MIS is particularly favourable in neurosurgery, due to the delicate and complex nature of the nervous system and the need to leave surrounding healthy neural tissue unharmed (Proctor & Black 2005).

One subset of MIS is percutaneous (i.e. through the skin) intervention, which involves the

insertion of a needle or a catheter of a few millimetres in diameter through the skin and into the tissue. Percutaneous interventions have been commonly performed in neurosurgeries, such as during deep brain stimulation (DBS) implantation (Shukla & Okun 2016), epilepsy treatment (Quigg & Harden 2014), and a relatively new direct drug infusion method to the brain called Convection Enhanced Delivery (CED) (Barua et al. 2014). As the surgeon does not have direct vision to the surgical site, the procedure is performed with image guidance (e.g. ultrasound, magnetic resonance imaging, and computer tomography). To improve the accuracy of the procedure, surgical robotic systems have also been implemented. The positioning accuracy of the robot and its ability to manipulate the surgical instruments are useful in assisting the surgeon, particularly during lengthy procedures (Li et al. 2002). The first robotic-assisted surgery was performed by Kwoh et al. (1988) to obtain brain biopsy samples using a modified industrial robot. The robot was implemented as an insertion guide for the biopsy needle. Using the robot, a faster and a more accurate positioning capability, compared to the stereotactic frame, was achieved. In contrast with the use of an industrial robot in its early application, current commercially available autonomous clinical neurosurgical robots, such as the Neuromate (Renishaw Plc.), are specifically designed to fit in a neurosurgical suite, and are equipped with software to perform precise image-based planning and visualisation of multiple trajectories (Li et al. 2002).

Even though robots have been used to manipulate surgical instruments in conjunction with pre-operative and intra-operative images, current percutaneous intervention procedures are generally performed using straight rigid needles. A rigid needle cannot compensate for a misplacement of the needle tip without retraction and reinsertion, which increases tissue trauma (Patel et al. 2007). In addition, not all lesions can be accessed because a straight path between the insertion point and the target area is not always viable. This limitation is driving researchers toward the development of a robotically controlled flexible instrument that can be steered to follow an arbitrary three-dimensional path within a substrate, referred to as a steerable needle.

The Mechatronics in Medicine Laboratory at Imperial College London is developing one such steerable needle to access deep lesions in the brain, which is inspired by the ovipositor of

certain insects. The needle consists of multiple segments (minimum of three) that can be steered by creating an axial offset between each segment. The unique multi-segment design of the needle allows an actuation strategy where the segment is moved forward in turn, cyclically. This actuation strategy could reduce tissue deformation during the insertion, thus increasing insertion accuracy whilst hypothetically reducing tissue damage (Leibinger et al. 2016).

During percutaneous intervention in the brain, the needle must avoid major blood vessels, as inadvertently puncturing one can pose a life-threatening complication that reduces the benefits of MIS. In a recent study about DBS implantation, for instance, up to 5% of patients undergoing this procedure had such complications (Fenoy & Simpson Jr 2014). Before surgery, preoperative imaging data are commonly used to plan a vessel-free insertion path; however, the data can be unreliable due to intra-operative brain shift and limited imaging resolution. In order to avoid these complications, real-time sensing during surgery is required. As of the date of this thesis, Wårdell et al. (2016) had deployed a laser-based sensor in a rigid needle while performing DBS implantation procedures. Using this sensor, a vessel in front of the needle tip, which had not been previously detected in the preoperative images, could be identified and subsequently avoided. However, even though a steerable needle system can follow a curvilinear path to avoid obstacles, there had been no reported use of a forward-looking sensor to detect and avoid a vessel in front of the needle tip.

Endowing a steerable needle with a real-time vessel detection sensor would help to fully utilize the steering capability of the needle. Using a steerable needle, the procedure could still be performed by generating a new insertion path to the target without the need for a full needle retraction. In addition to vessel presence detection, information acquired about the vessel pose could be inferred to provide the necessary knowledge to plan and execute a subsequent avoidance strategy.

## 1.2 Thesis Aim and Objectives

The aim of the study in this thesis was thus to:
*Investigate a method to improve the safety of percutaneous intervention procedures for miniaturised programmable bevel-tip needles, by embedding sensors to detect the presence of a vessel during the insertion process, to be evaluated in realistic soft tissue phantom materials.*

Endowing a steerable needle with real-time intraoperative vessel detection sensors will decrease risks of haemorrhage during intervention procedures, which is an essential aspect for the steerable needle to be viable for clinical usage. With regards to the biologically inspired steerable needle concept conceived at Imperial College, its outer dimension first needs to be reduced. Materials and manufacturing strategies that would allow its overall diameter to be shrink down to a clinically acceptable size are thus investigated. Secondly, a comprehensive study of possible embed vessel detection sensors suitable for a clinically sized needle prototype is performed. A sensor is then chosen and characterised to study its compatibility with deployment within the steerable needle ecosystem. The knowledge of vessel pose is crucial for the steerable needle system to execute an avoidance strategy. Therefore, algorithms to infer vessel pose from sensors measurements are developed. The possibility to deploy more than one sensor inside the biologically inspired steerable needle is explored and exploited during algorithms development for vessel pose inference. Several approaches, including machine learning, are explored to improve prediction accuracy, and *in-vitro* experiments are performed to isolate the relevant parameters for the model and to quantify detection performance.

Consequently the objectives of this thesis are:

- To develop strategies to miniaturise the current needle prototype from an initial size of 4 mm outer diameter down to a size of no more than 2.5 mm outer diameter, which should be manufactured in a biocompatible material (e.g. via the use of additive layer manufacturing in plastic or metal in the first instance, followed by subcontracting of an advanced design for final manufacture).

- To investigate the range of real-time vessel detection systems associated with deep needle

insertion with the aim to highlight sensors that are compatible with the biologically inspired steerable needle technology.

- To characterise the chosen real-time vessel detection system in a tissue phantom.
- To undertake a feasibility study of the compatibility of the chosen sensor based on its characterisation results to the steerable needle technology.
- To develop an algorithm that can be used to predict the vessel pose based on the measurements from several sensors and to quantify performance via *in-vitro* trials.
- To explore machine learning methods to improve vessel pose prediction accuracy.
- To generate simulation data that can model measurements from the chosen system with sufficient fidelity to serve as training data for a predictive network.

## 1.3 Thesis Contributions

The research presented in this thesis has resulted in a number of peer-reviewed publications in international journals and conferences. A list of all relevant publications, with a brief statement about their relevance with respect to this thesis, can be found below.

- Vani Virdyawan, Joshua W Giles, Richard J van Arkel, Matthew Oldfield, and Ferdinandor Rodriguez y Baena (2015). "High Aspect Ratio Additive Manufacturing of a Biologically Inspired Surgical Needle". In: *Design of Medical Devices Conference Europe Edition 2015*, pp. 9-10

  This study investigated our first effort to miniaturise the biologically inspired needle that is under development at Imperial College London using a laser-based additive manufacturing (AM) technique. The needle was difficult to manufacture due to the intricate design of its interlock mechanism and its high aspect ratio. A benchmark part was designed to systematically evaluate the optimum build strategy for the needle using an AM machine. Even though a needle was successfully built, the needle was too stiff to be used as a

steerable needle. Nonetheless, the manufacturing strategy developed in this publication could be translated to manufacture other high aspect ratio components. This research is presented in Chapter 3.

- Vani Virdyawan, Matthew Oldfield, and Ferdinando Rodriguez y Baena (2016). "Laser Doppler Sensing for Blood Vessel Detection with a Steerable Needle". In: *6th Joint Workshop on New Technologies for Computer/Robot Assisted Surgery 2016*

  The characterisation results of a laser Doppler flowmetry (LDF) sensor were presented in this publication. Since the position of needle's working channels had an offset with respect to the needle axis, this publication also discusses the minimum requirements for the sensor detection range as to avoid puncturing a vessel in front of the needle.

- Vani Virdyawan, Matthew Oldfield, and Ferdinando Rodriguez y Baena (2018). "Laser Doppler sensing for Blood Vessel Detection with a Biologically Inspired Steerable Needle". In: *Bioinspiration and Biomimetics*, 13:2, p 026009

  This study provides a valuable insight into develop an algorithm to predict vessel pose using laser Doppler flowmetry (LDF) sensors. Characterisation results of the LDF sensor showed that the perfusion value measurements of the LDF did not give any information about vessel position. The vessel positions were defined based on axial and off-axis distance from the probe. Moreover, a single perfusion value can be associated with many different axial and off-axis distance combinations. A look-up table for a specific vessel and tissue properties was created to relate a perfusion value with its corresponding axial and off-axis positions. In this publication, successive measurements were used to reduce the possible positions of the vessel and measurements from a second probe were used to reduce the possibility of the vessel pose ambiguity. This research is presented in Chapter 4.

- Vani Virdyawan, and Ferdinando Rodriguez y Baena, Vessel Pose Estimation for Obstacle Avoidance in Needle Steering Surgery using Multiple Forward Looking Sensors, in: 'Proceedings of the IEEE International Conference on Intelligent Robots and Systems (IROS)', Oct. 2018.

This publication investigated the use of relative measurements from four forward-looking sensors to infer the "no-go" area in front of the steerable needle based on an assumption that the vessel is located in a perpendicular plane to the needle insertion axis. The algorithm in Chapter 4 could only be applied to a specific vessel and tissue optical properties. The use of relative measurements in this publication acted as a normalisation step for the perfusion value, which then allowed the method to be used for any vessel and tissue optical properties. This research is presented in Chapter 5.

In addition to the above publications, Chapter 6 discusses the use of a Long Short-Term Memory network to improve vessel pose predictions accuracy, which is about to be submitted as a further publication. Using the machine learning technique, vessel pose and diameter could be defined even without assuming vessel perpendicularity to the insertion axis. Predicting the vessel diameter and locations were performed without previous knowledge about the vessel and tissue optical properties. These results demonstrate a significant improvement in the prediction accuracy and detail, compared to the results in Chapter 4 and 5.

## 1.4 Thesis Structure

This thesis consists of an investigation in the use of forward-looking sensors embedded within a biologically inspired steerable needle.

Chapter 2 aims to describe the need for using real-time vessel detection sensors in a steerable needle system. Relevant literature about medical needs, vessel detection sensors for deep needle insertion, and the needle steering concept, is presented. Additionally, the state of the art in needle steering sensorisation is summarised.

Chapter 3 discusses strategies to miniaturise the biologically inspired steerable needle. In the first half of this chapter, an approach to miniaturising the needle prototype using metal additive layer manufacturing is discussed. Here, a systematic method to develop the manufacturing strategy is discussed based on the characterisation results of a benchmark component. The

second half of this chapter discusses a micro-extrusion process to produce the functional prototype that was subsequently implemented by our subcontractor to produce a clinically sized, medical grade 2.5 mm flexible needle. Additionally, the development of a fixture to accurately create the bevel-tip angle in each of the needle segments is described.

Chapter 4 investigates the feasibility of using forward-looking sensors in the biologically inspired steerable needle. Additionally, this chapter describes the method to predict the vessel position using successive measurements of a sensor, and a method to reduce vessel pose ambiguity based on two sensors embedded within the needle.

Chapter 5 describes the algorithm developed to predict a "no-go" area based on measurements from four sensors embedded in the biologically inspired steerable needle. In this chapter, the effect of readings taken by the sensor during continuous needle insertion is also explained.

Chapter 6 investigates the use of a machine learning technique based on a Long Short-term Memory network to predict vessel parameters such as vessel diameter, as well as the full vessel pose (i.e. position and orientation) with improved accuracy and detail with respect to methods presented in previous chapters. A simulation method to generate a large array of training data for the network is explained, followed by application of the trained network to real experimental data, with the aim to assess prediction accuracy under a realistic set-up.

This thesis concludes with Chapter 7, where a summary of the main findings resulting from the completed work is presented. The limitations of this work and a number of future research avenues are also highlighted.

# Chapter 2

# Literature Review

## 2.1 Introduction

This chapter presents a thorough review to make the context of the thesis clear. It begins with an introduction of clinical needs in minimally invasive brain surgery. The efforts to avoid vessel puncture during minimally invasive brain surgery using rigid needles are then explained. The limitations of rigid needles, which can only follow a straight insertion path and are unable to correct any misalignment drive the development of steerable needle systems. The designs of steerable needle systems are discussed, with a primary focus on the programmable bevel-tipped needle that has been developed at Imperial College London. The state of the art in the sensorisation of steerable needles is also presented to investigate the gap between the latest technological developments and the current clinical need to avoiding blood vessel punctures.

This chapter is an edited version of the following publications:

- Vani Virdyawan, Matthew Oldfield, and Ferdinando Rodriguez y Baena (2018). "Laser Doppler sensing for Blood Vessel Detection with a Biologically Inspired Steerable Needle". In: *Bioinspiration and Biomimetics*, 13:2, p 026009. ©IOP Publishing 2018.

- Vani Virdyawan, and Ferdinando Rodriguez y Baena, Vessel Pose Estimation for Obstacle Avoidance in Needle Steering Surgery using Multiple Forward Looking Sensors, in:

'Proceedings of the IEEE International Conference on Intelligent Robots and Systems (IROS)', Oct. 2018.

## 2.2 Percutaneous Intervention in Brain Surgery

The use of percutaneous intervention during brain surgery is favourable due to the delicate and complex nature of its structure and the requirement to leave surrounding healthy tissue unharmed (Goldberg et al. 2005). These methods have been performed for biopsies (Pinggera et al. 2017), deep brain stimulation (DBS) implantation (Shukla & Okun 2016), epilepsy treatment (Quigg & Harden 2014), thermal ablation for tumour therapy (Goldberg et al. 2005) , and a relatively new direct drug infusion method to the brain called Convection Enhanced Delivery (CED) (Barua et al. 2014). Generally, such procedures offer several benefits for the patient due to reduced trauma and a faster recovery time (Westebring-Van Der Putten et al. 2008). However, puncture of a blood vessel during the insertion process can pose a life-threatening complication for which a robust solution that works with all vessel sizes has not yet been found (Binder et al. 2003, Field et al. 2001, Fenoy & Simpson Jr 2014, Woodworth et al. 2006, Hall 1998, Umemura et al. 2003). Field et al. (2001) reported that up to 8% of patients who underwent a biopsy procedure had this complication, while during deep brain stimulation, Fenoy & Simpson Jr (2014) found an occurrence of 5%.

Even though preoperative imaging data are used to plan a safe, obstacle-free path (De Benedictis et al. 2017), intraoperatively, brain shift and other tissue deformations (such as pulsatile motion and breathing) may occur that would invalidate the plan, with the subsequent need for updated images to be acquired (Gerard et al. 2017). To avoid these complications, real-time sensing is needed in the operating theatre. Unfortunately, commonly used imaging modalities such as Magnetic Resonance Imaging (MRI), X-Ray and Ultrasound do not lend themselves to use intraoperatively in this application. MRI is expensive, requires significant processing time to construct the image volume and requires MRI-compatible tools (Peters & Cleary 2008, Miga 2016). The ionising radiation of X-rays hinders its application in lengthy surgical procedures.

While ultrasound can and has been used intraoperatively, its resolution is currently not able to capture millimetre-size vessels, and ultrasound waves cannot easily penetrate the skull (Liang et al. 2013). Even though there is an option to use intraoperative ultrasound through a burr hole, this method cannot reduce the incidence of intracranial haemorrhages (Allouch et al. 2014). In addition, there are in fact high-risk vessels with a diameter larger than 0.2 mm but smaller than 1 mm (Huang et al. 2013) that would be too small to be detected during preoperative imaging due to the resolution of MRI and CT where voxel sizes are typically 0.59 × 0.59 × 1 mm (Bériault et al. 2014). Based on these limitations of the current imaging modalities, several efforts have been made to detect a vessel by embedding a sensor in a rigid needle.

## 2.3 Sensors for Vessel Detection in Brain Surgery

One major challenge for embedding a sensor at the tip of a needle for percutaneous intervention procedures is to miniaturise the sensor size. The sensor has to be fitted inside needles that have diameters in the range of 1.3 - 3.0 mm (Parittotokkaporn 2011). Based on the area that needs to be investigated with respect to the axis of the needle, there are two types of viewing systems: forward viewing, and side viewing. In the literature, two imaging modalities have been embedded inside rigid surgical needles: ultrasound and light-based systems.

A single crystal ultrasound has been used to manufacture a miniature ultrasound probe (Hartley & Cole 1974, McPhillips et al. 2015). The single crystal system can be implemented either as a forward or side viewing probe (McPhillips et al. 2015) (Figure 2.1a). Since the probe consists only of a single crystal, it only gives depth information about the investigated tissue (referred as A-scan). The size of the probe can be miniaturised down to a diameter of 0.66 mm, as was designed for retinal surgery (Zhou et al. 2007). Ungersböck et al. (1992), Hertel et al. (2005), and Yamasaki et al. (1994) used a commercially available single crystal ultrasound Doppler probe with a diameter of 1 mm during biopsy procedures. The tissue in front of the needle was investigated by checking the Doppler reading of the probe. Using this method, the needle was inserted incrementally with an insertion depth equal to the maximum depth detection of the

Doppler ultrasound sensor.

A two-dimensional (B-scan) and three-dimensional (C-scan) image require scanning of the single crystal ultrasound probe. Inside the tissue, scanning the probe may not be possible. To image a 3D volume in front of the needle, Light et al. (2007) designed a 6.48 × 6.48 mm forward viewing matrix array ultrasound to be implemented in a neuro-endoscope (Figure 2.1b). The probe has a pyramid shape field of view to visualise brain structures. Schiavone et al. (2017) also proposed a matrix array ultrasound probe to be embedded into a surgical probe. However, instead of a forward viewing probe, they designed a side viewing probe to be embedded into a 1.9 mm diameter sedan type biopsy needle. The probe generates two-dimensional images. Miniaturisation of an ultrasound system is still very challenging, with the smallest probe having a diameter of 0.66 mm. Light-based systems, on the other hand, are easily miniaturised due to the use of optical fibre to deliver the laser/light to and to collect the information from the tissue, in which the smallest probe has a diameter of 0.125 mm (Liang et al. 2013).

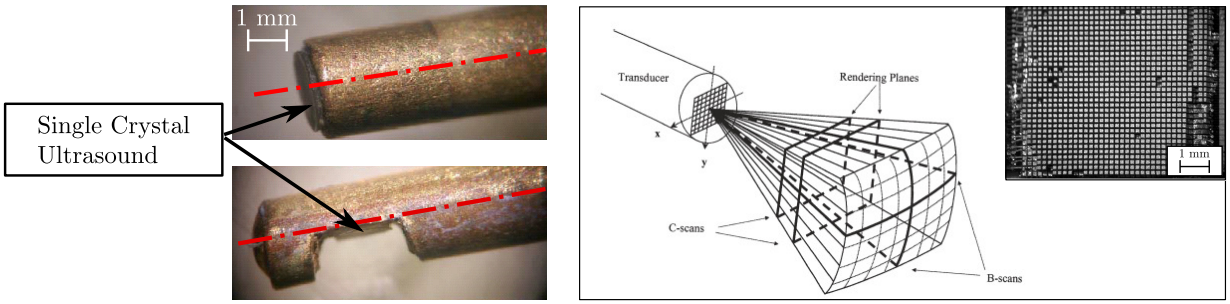


**Figure 2.1:** a) A single crystal ultrasound that was implemented as a forward viewing probe (top) and side viewing probe (bottom). Reprinted, with permission, from McPhillips et al. (2015) ©2015 IEEE. b) A schematic diagram of a matrix array ultrasound probe with its pyramid shape detection volume. The inset in the figure shows the 6.48 × 6.48 mm matrix array probe. Reprinted, with permission, from Light et al. (2007) ©2007 IEEE

Optical Coherence Tomography (OCT) is a high resolution imaging modality that employs low coherence interferometry of light to provide near histological information (Podoleanu 2005). Like a single crystal ultrasound probe, it generates A-scan images and requires axial scanning or rotation of the probe to get B-scan and C-scan images. Liang et al. (2011) developed a forward viewing OCT probe that has a diameter of 0.5 mm (Figure 2.2). A Gradient Index (GRIN) rod lens was used to deliver to and receive the laser from the tissue. To obtain the

B-scan images, the laser beam was scanned at the surface of the proximal end of the lens using a galvanometer scanning mirror (see Figure 2.2). Blood vessels were detected by using Doppler OCT (DOCT). Even though it has a high resolution (17 $\mu$m axial resolution, and 12 $\mu$m transverse resolution) its depth detection is only 1 mm.

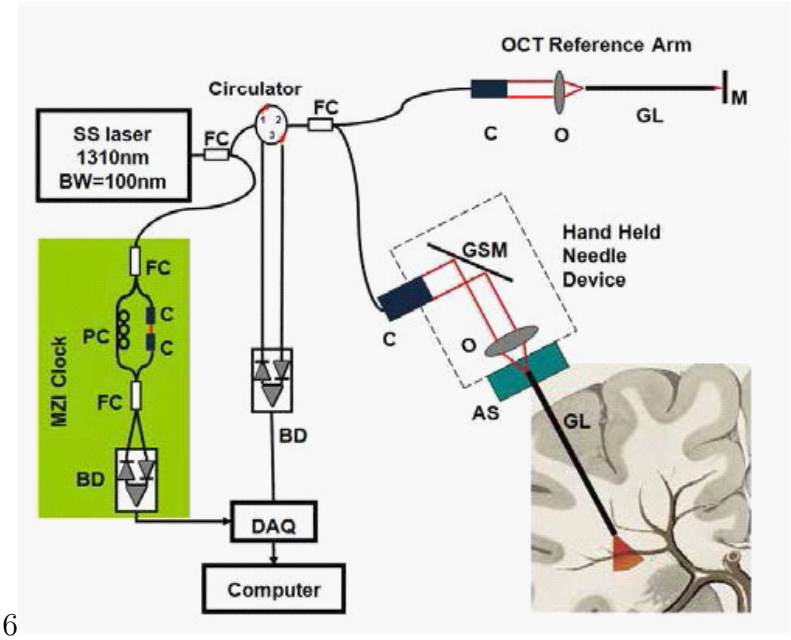


6

**Figure 2.2:** Schematic of the forward viewing OCT probe using a long thin GRIN rod lens with a galvanometer scanning mirror to acquire B-scan images. FC: fibre coupler, PC: polarization controller, C: collimator, BD: balanced detector, MZI: Mach-Zehnder interferometer, DAQ: data acquisition board, M: mirror, GSM: galvanometer scanning mirror, O: objective lens, AS: alignment stages, GL: GRIN lens needle. Reprinted, with permission, from Liang et al. (2011) ©2011 Optical Society of America

Even though OCT has a very high resolution, it requires extensive post-processing and an expensive system to obtain the images. Since the primary requirement for vessel detection in a rigid needle is detecting the presence of a vessel in front of the needle without having to know the exact location of the vessel, Liang et al. (2013) simplified the OCT probe design by developing a Coherence-gated Doppler (CGD) probe. The system did not need interferometer path length scanning, signal digitization and demodulation of an OCT system. The Doppler beating signals are converted to audio signals to differentiate tissue, vein and artery. The use of a single mode fibre and a GRIN multimode fibre for focussing allowed the probe diameter to reach 0.125 mm. The probe has significantly deeper detection range compared to OCT, with a depth detection range of 3.4 $\pm$ 1.3 mm and a lateral resolution $<$ 100 $\mu$m.

Laser Doppler Flowmetry (LDF) monitoring systems are commonly used to monitor micro-circulation (i.e. circulation in very small vascular capillaries). The LDF sensors detect blood vessels by measuring the Doppler shift generated by the movement of the blood cells that they contain. Laser light is delivered into tissue through an illumination fibre, scattered inside the tissue, and collected by a collection fibre. Due to this scattering, it is challenging to determine the source of the signal, and thus determining the absolute perfusion value of blood flow is not possible (Fredriksson et al. 2010). Therefore, the perfusion value is relative and is calibrated with Brownian motion of latex particles in water, with an arbitrary unit (AU). LDF probes have been used in real clinical procedures. Haj-Hosseini et al. (2018) used an LDF probe during tumour biopsy, while Wårdell et al. (2016) used the probe during DBS implantation procedures. A perfusion value threshold was implemented to detect the presence of a vessel close to the needle (see Figure 2.3). Besides the perfusion value, total light intensities (TLI) of the sensors were recorded to check tissue greyness.

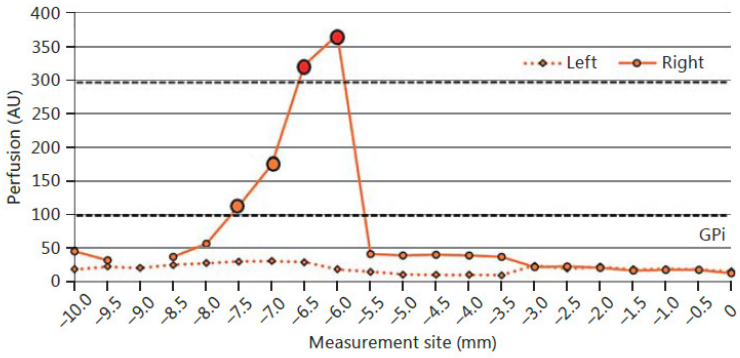


**Figure 2.3:** Example of perfusion value measurements using an LDF probe during a DBS implantation procedure to the left and right globus pallidus internus (GPi). Very high blood flow values (in this case >300 AU) were observed during the insertion to the right GPi target. Reprinted, with permission, from Wårdell et al. (2016) ©2016 S. Karger AG

DOCT, CGD, and LDF detect the presence of a blood vessel based on Doppler shift of the illumination light due to blood cells movement. It should be noted that CGD and LDF also record the movement of the tissue, and this movement needs to be accounted for since the movement of large scattering particles with slow movement will be erroneously recorded as a high perfusion value (Öberg 1999). Therefore, a very slow needle insertion or an intermittent insertion process have been performed to reduce this measurement error in previous work (Liang et al. 2013, Wårdell et al. 2016, Haj-Hosseini et al. 2018).

DOCT, CGD, and LDF require a laser with a certain coherence length. Instead of using laser as the illumination source, Markwardt et al. (2017) designed a simpler system using a cheaper broadband LED as the illumination source. The presence of a vessel close to the probe was determined by comparing the remission spectra of 578 and 650 nm. The 578 nm wavelength is the local absorption maximum for oxygenated haemoglobin, while the second wavelength gives the highest possible difference in haemoglobin absorption. The probe consists of two fibres, one for illumination and one for collection, with an offset of 1.8 mm between them, which was integrated into a biopsy needle (Figure 2.4a). To perform side viewing, the tip of the fibres were ground at an inclination angle of 45° and coated with aluminium. The probe has a detection range of up-to 0.8 mm. However, it can not differentiate between blood vessels and blood in the insterstitium from an injured minor blood vessel (Markwardt et al. 2017).

Interstitial Optical Tomography (iOT) was proposed by Goyette et al. (2015) and Pichette et al. (2015*a*) to allow 360° interrogation of tissue surrounding a biopsy needle (Figure 2.4b). Blood vessels are detected by associating high-absorption brain areas to high concentration of haemoglobin. The probe has an outer diameter of 1.7 mm and consists of 12 pairs of illumination and detection fibres. A micro-prism was attached into the tip of each fibre pair for side-viewing. The tissue was illuminated sequentially using a broadband light source. Except for the fibre that shared the same prism, the signals were recorded sequentially. The intensity of each source detector pair was used to determine the safe area in the brain to sample the tissue. iOT can detect a blood vessel surrounding the needle up to a distance of 2 mm.

Fluorescent dye has also been used for vessel detection in percutaneous intervention neurosurgery (Göbel et al. 2012). Indocyanin green (ICG) fluorescent dye was injected into the vascular system. The dye was excited with 785 nm laser light (the maximum absorption wavelength of the dye). The fluorescence can then be visualised by filtering the excitation light. In order to deliver the illumination light and receive the fluorescence signals, semi-flexible coherent fibre bundles with an outer diameter of 1 mm were used. The fibre bundles comprise of several tens of thousand of individual fibre cores. The forward viewing fluorescence signals can be visualised with an area of a 0.7 mm diameter. This system could detect the presence of a blood vessel up to 1 mm from the tip of the fibre bundles.

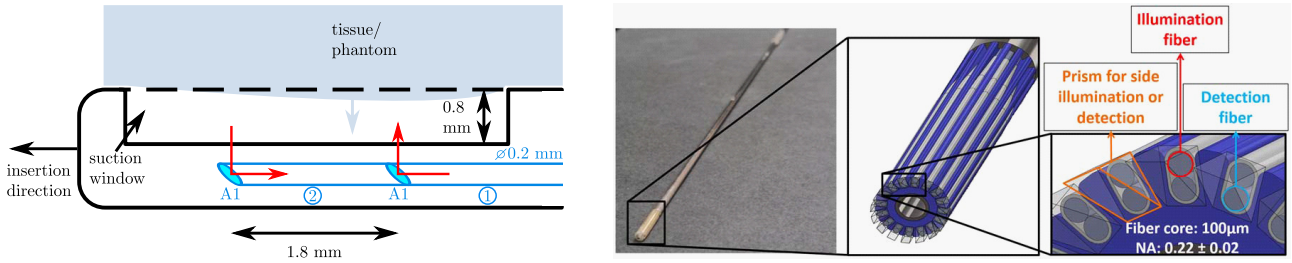


**Figure 2.4:** a) Schematic diagram of the remission spectroscopy probe inside a biopsy needle. The tip of the illumination (①) and the collection (②) fibre were grounded with a 45° angle and coated with aluminium to perform side viewing (A1). Reprinted, with permission, from Markwardt et al. (2017) ©2016 John Wiley and Sons. b) The enlarged view of the interstitial Optical Tomography (iOT) probe that shows its illumination and detection fibres. Reprinted, with permission, from Goyette et al. (2015) ©2015 Optical Society of America

Table 2.1 summarises the sensorisation method in rigid needle systems that were discussed in this section. The dimension of the sensors and its detection range could be used to highlight suitable sensors for a particular application.

## 2.4 Steerable Needle Systems

The systems mentioned in Section 2.3 were embedded in a rigid needle. This means that, if there is an obstacle (e.g. a blood vessel) detected along the insertion path, the procedure must be interrupted. To address this limitation, current research has been directed towards

**Table 2.1:** Rigid needles sensorisation. LDF: laser Doppler flowmetry; OCT: Optical Coherence Tomography; CGD: Coherence-gated Doppler; US: ultrasound

| Reference | Modality | Viewing | Dimension | Detection range |
|---|---|---|---|---|
| Haj-Hosseini et al. (2018) | LDF | Forward | ⌀ 2.2 mm | 2 mm |
| Liang et al. (2011) | Doppler OCT | Forward | ⌀ 0.5 mm | 1 mm |
| Schiavone et al. (2017) | Matrix Array US | Side | 1.9 x 4 mm | NA |
| Liang et al. (2013) | CGD | Forward | ⌀ 0.125 mm | 4 mm |
| Ungersböck et al. (1992), Hertel et al. (2005) | Single Crystal US | Forward | ⌀ 1 mm | 15 mm |
| Wårdell et al. (2016) | LDF | Forward | ⌀ 2.2 mm | 2 mm |
| Göbel et al. (2012) | Fluorescence | Forward | ⌀ 1.0 mm | 1 mm |
| Light et al. (2007) | 3D Matrix Array US | Forward | 6.48 x 6.48 mm | 30 mm |
| Markwardt et al. (2017) | Remission Spectroscopy | Side | ⌀ 0.5 mm | 0.8 mm |
| Pichette et al. (2015*b*), Goyette et al. (2015) | Interstitial Optical Tomography | Side | ⌀ 1.7 mm | 2 mm |
| McPhillips et al. (2015) | Single Crystal US | Side and Forward | ⌀ 1.7 mm | 15 mm |
| Yamasaki et al. (1994) | Single Crystal US | Forward | ⌀ 1,2,3 mm | 7 mm |

the field of steerable needles, as these have the ability to steer around obstacles and thus correct for any misalignment (Abolhassani, Patel & Moallem 2007). Steering inside tissue is achieved by controlling the bending of the needle either as a direct result of passive needle-tissue interactions or active modification of the needle shape (van de Berg, van Gerwen, Dankelman & van den Dobbelsteen 2015). Steerable needle designs cover needle-base manipulation (DiMaio & Salcudean 2003), bevel-tipped needles (Webster et al. 2005), concentric tube needles (Webster, Okamura & Cowan 2006, Dupont et al. 2010), tendon actuated needles (van de Berg, Dankelman & van den Dobbelsteen 2015, Adebar et al. 2016, Gerboni et al. 2017), and programmable bevel-tipped needles (Ko et al. 2011). For a complete overview of the steerable needle designs, the reader is referred to the literature (e.g. van de Berg, van Gerwen, Dankelman & van den Dobbelsteen (2015)).

DiMaio & Salcudean (2003) proposed a needle base manipulation method to steer the needle. By changing the orientation and lateral position of the needle base, the shape of the needle inside the tissue can be altered, enabling the needle tip position and orientation to be controlled (Figure 2.5). Glozman & Shoham (2007) modelled the needle as a linear beam supported with virtual springs to perform trajectory tracking under closed-loop fluoroscopic guidance. As the needle penetrates deeper in the tissue, the needle motion becomes constrained (DiMaio & Salcudean 2003) (Figure 2.5 right) and the steering moments around the base increase rapidly (van de Berg, van Gerwen, Dankelman & van den Dobbelsteen 2015). This can lead to a risk of tissue slicing by the needle (Leibinger 2016).

The tip of the tendon-actuated needle can be articulated during the insertion to control tool-tissue interaction forces and thus the insertion trajectory. van de Berg, Dankelman & van den Dobbelsteen (2015) described a two-degree-of-freedom ball-and-socket joint tendon actuated needle tip to achieve 3-D steering. A simpler design was proposed by Adebar et al. (2016) by using a single-degree-of-freedom joint in the needle tip. 3-D steering can be performed by rotating the needle during the insertion. A further development of the needle has been used to perform multiple ablations via a single entry in *ex-vivo* liver (Gerboni et al. 2017). Even though the tendon-actuated design achieves a small radius of curvature ($< 50$ mm), articulating the tip will displace the tissue surrounding the tip of the needle (Adebar et al. 2016), which is

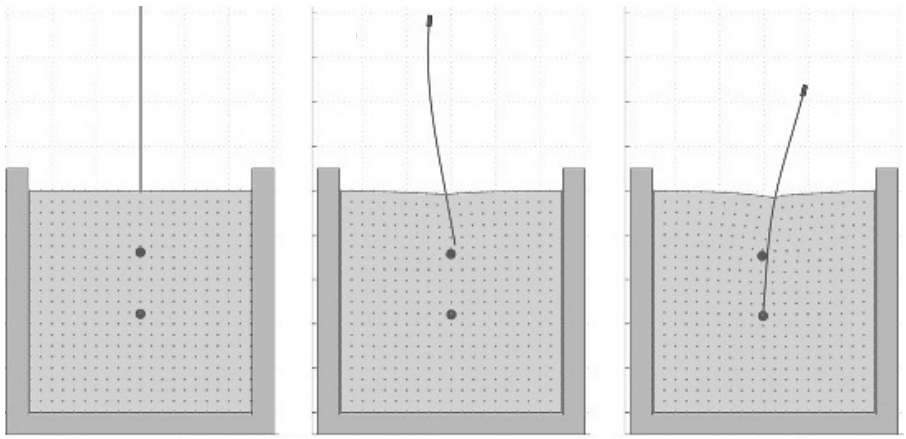

**Figure 2.5:** Illustration of a needle steering using base manipulation method. Needle tip position and orientation are controlled by changing the orientation and the lateral position of the needle base. Adapted with permission from Springer Nature, (DiMaio & Salcudean 2003), ©2003

undesirable.

A concentric tube needle consists of several telescoping pre-curved super-elastic tubes (Webster, Okamura & Cowan 2006, Dupont et al. 2010). Each of the tubes can be retracted, extended, and rotated with respect to one another. In doing so, their curvature will interfere with one another, affecting the shape of the overall needle. Therefore, steering concentric tube needles does not require tool-tissue interaction forces to be exploited. However, for use as a steerable needle system, follow-the-leader deployment (e.g. the shaft exactly follows the path of the tip) of the concentric tube robot is necessary, which continues to present significant technical challenges (Garriga-Casanovas & Rodriguez y Baena 2018).

The most commonly used method for needle steering is based on bevel-tipped needles. Due to tip asymmetry, the bevel-tipped needle bends more than cone or triangular tipped needles (Okamura et al. 2004) (Figure 2.6a). Needle bending due to asymmetric tip forces is usually assumed to follow a constant curvature (Webster, Kim, Cowan, Chirikjian & Okamura 2006). The curvature is affected by several parameters, such as tissue mechanical properties, needle diameter (Misra et al. 2010) and bevel angle (Webster et al. 2005). Interestingly, in contrast with experimental results in a soft tissue phantom, in *ex-vivo* tissue, the needle bevel angle does not have any effect on the needle curvature (Majewicz et al. 2010). In an application where a tighter radius of curvature is needed, a bevel-tipped needle with pre-curved tip (Wedlick & Okamura 2012) and flexure-tip (Swaney et al. 2013) have been proposed.

Since deflections of the bevel-tipped needle naturally occur if the needle is inserted into soft tissue, Abolhassani, Patel & Ayazi (2007) rotated the needle by 180° at certain insertion depths to compensate for the needle deflection to steer the needle in a straight trajectory. Engh, Podnar, Kondziolka & Riviere (2006) introduced spinning of the needle to achieve a straight insertion (Figure 2.6b). Additionally, by changing the duty cycle of the spinning needle, defined as the ratio of pure insertion to insertion with rotation, the curvature of the needle can be controlled (Engh, Podnar, Kondziolka & Riviere 2006). Continuous rotation of the needle, however, prevents the use of sensors in the needle due to cable wind up issues (Majewicz et al. 2014). To tackle this problem, Majewicz et al. (2014) introduced two steering algorithms: continuous insertion with bidirectional rotation and duty-cycled flipping. Spinning of the needle also can cause damage to the surrounding tissue during insertion (Swaney et al. 2013). To minimise tissue damage, 3D needle steering by minimising the number of needle rotations has also been suggested (Abayazid et al. 2014, Shahriari et al. 2015). Tissue damage due to needle rotation may prevent the use of bevel-tipped steerable needles in a soft and delicate tissue such as brain. This limitation, fuelled research into the development of a novel biologically inspired steerable needle system where axial rotation is not necessary.

**Programmable Bevel-Tip Needle Steering**

The programmable bevel-tip needle (PBN) design, first demonstrated by Frasson et al. (2012) offers a multi-segment approach, which is inspired by the ovipositor of parasitic wasps in the Ichneumonoieda family. The ovipositor, which is approximately 0.2 mm in diameter, can be as long as 18 cm, possessing the ability to penetrate wood and to steer within it to reach a suitable location to lay eggs (Quicke 2014). It consists of multiple valves, called ventral and dorsal valves, which interlock with one another through a dovetail mechanism called the olistheter (Quicke 2014). The olistheter holds the valves together, but also allows them to slide independently with respect to one another. This unique configuration enables the insect to enact a reciprocating insertion strategy, in which forward axial motion is performed sequentially by each valve, in such a way to avoid buckling even in the presence of a hard substrate, such as the bark of a tree (Sakes et al. 2016, Vincent & King 1995).

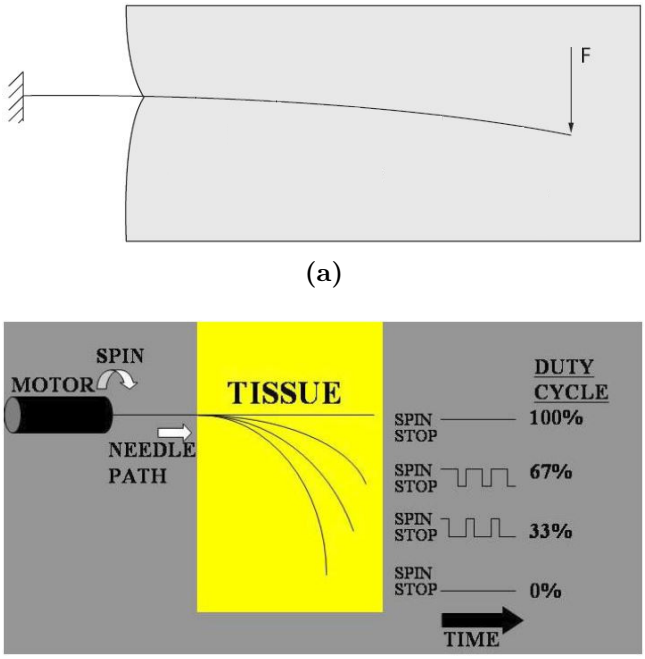


**Figure 2.6:** (a) Lateral component of asymmetric tissue reaction force at a bevel-tipped needle (F) results in needle bending (adapted with permission from (van de Berg, van Gerwen, Dankelman & van den Dobbelsteen 2015) ©2015 IEEE), and (b) The needle curvature can be controlled by changing the duty cycle of the spinning needle (reprinted with permission from (Engh, Podnar, Khoo & Riviere 2006) ©2006 IEEE)

Outward facing teeth are present at the tip of the valves, which can be used to anchor each segment onto the wood to generate a tensioning force that stabilizes the insertion (Vincent & King 1995). After failing to reproduce this mechanism based on anisotropic surface characteristics (Frasson et al. 2008), teeth were replaced by a complex sequential insertion method that achieves the same tensioning effect through the ratio between stationary and moving segments of a 4-part PBN (i.e. always maintaining a larger amount of contact surface that is stationary at any one point during the insertion). Oldfield et al. (2015) demonstrated that such an approach enables a reduction in the motion of the tissue surrounding the needle, thus improving the accuracy of needle tip delivery.

Detailed observation of a parasitic wasp probing behaviour shows that the multi-segment ovipositor is also useful for steering. The offset between segments generates an asymmetric reaction force in the tip of the ovipositor during the insertion process that results in bending along a prescribed direction (Figure 2.7). By varying this asymmetry, the radius of curvature of the bend can be controlled, enabling the ovipositor to be steered (Cerkvenik et al. 2017).

Similar to its biological counterpart, the PBN design consists of at least two segments that are linked by a dovetail mechanism, enabling these to slide with respect to one another. Embodiments of a four-segment needle demonstrate the ability to steer along an arbitrary three-dimensional (3D) path (Secoli et al. 2018) (Figure 2.9c) without relying on transmission of torque from base to tip. Therefore, PBNs can be manufactured from highly compliant materials that can be matched to a softer tissue, such as brain, in order to enhance dexterity (Gilbert & Webster 2013). In addition, compliant materials can also be useful to manufacture an implantable needle for long term brain treatment (Rosenbluth et al. 2011), a clear focus of the current, EU funded EDEN2020 project (www.eden2020.eu).

Due to the intricate design of the needle, the PBN development was performed using additive manufacturing process. Early PBN prototypes with a diameter of 12 mm (Ko et al. 2011) were manufactured using a rubber like material using a 3D printer (Object Connex500$^{TM}$). Using the 3D printer machine, the smallest four-segment PBN that was successfully manufactured has a 4 mm diameter, which was manufactured with a 'composite' body structure with alternating rigid and soft sections (Burrows et al. 2017) (Figure 2.8). However, to be clinically viable, the needle should have a diameter $< 2.5$ mm (Parittotokkaporn 2011). Therefore, the current embodiment of the needle is manufactured using a biocompatible polymer with an outer diameter of 2.5 mm (Matheson et al. 2018), which is the same size as that of commercially available biopsy needles (e.g. the sedan side cutting biopsy needle, A2430-01, Electa, Stockholm, Sweden). Figure 2.9

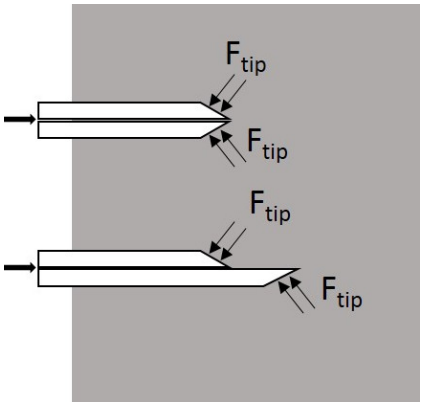


**Figure 2.7:** The tip force is symmetric where the segments are aligned so that there is no bending in the ovipositor, the asymmetric force where the ovipositor has an offset produces bending

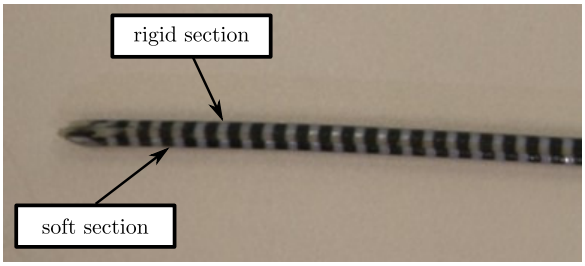


**Figure 2.8:** The 4 mm PBN that was manufactured using additive manufacturing with rubber like materials. Each needle segment has soft (black) and rigid (black) section, as described in (Burrows et al. 2017)

**(a)** **(b)** **(c)**

**Figure 2.9:** (a) The PBN with all of the segments aligned, and (b) with offsets introduced into the needle. (c) Cross section of the needle, which has a diameter of 2.5 mm and four, 0.3 mm OD working channels. Steering direction can be controlled by changing leading segment.

shows microscope images of the PBN, a representation of the relative motion between segments, and a schematic of its cross section. Figure 2.9c shows that the needle has a lumen in each of its segments. The lumen can be used as a conduit to deliver drugs and minimally invasive instruments, or as the working channel for imaging modalities based on optical fibres.

## 2.5 Image Guidance and Sensorisation of Steerable Needles

In the literature, the performance of a steerable needle system is usually reported in terms of its ability to steer around obstacles and its targeting accuracy. Extensive research has been conducted into needle designs, the modelling and control of the needle, and needle path planning. In this section, steerable needle sensing methods are discussed. The sensing methods are classified into two main categories: image guidance, and sensors embedded in the needle or

in the robotic platforms.

### 2.5.1 Image Guidance

Tracking the needle tip is required for controlling the needle in a close loop manner. One method to obtain this information is by using imaging modalities, such as: camera, ultrasound, X-ray, and MRI.

#### Camera

A camera and a pair of cameras in a stereo set up have been used in transparent phantoms (Misra et al. 2010, Swaney et al. 2013, Abayazid et al. 2014, Bernardes et al. 2013, Swensen et al. 2014, Bui et al. 2016). The use of a single camera for tracking the needle tip is justified by the assumption that the needle is steered in a plane. For 3D steering, a more sophisticated two cameras system is used. Using cameras, besides tracking the tip position of the needle, the whole shape of the needle can also be measured. The needle shape reconstruction is usually performed during needle characterisation to find the maximum curvatures that can be performed by the needle (Swaney et al. 2013, Misra et al. 2010). The requirement of the needle to be in the camera line of sight, however, limits its use in a real clinical set-up.

#### Ultrasound

Ultrasound (US) is inexpensive, portable, without ionisation radiation, and provides real-time images. With these advantages, ultrasound has been extensively used in steerable needle researches (see Table 2.2). However, US images are noisy, therefore several methods such as hough transforms (Vrooijink et al. 2014, Ayvali & Desai 2015), modified optical flow (Ayvali & Desai 2015), and random sample consensus (RANSAC) (Waine et al. 2016) have been implemented to detect the needle tip and shape. Adebar et al. (2014) improved the visibility of the needle in ultrasound images by generating a high frequency low amplitude movement of the needle so that its shape could be easily segmented using the Doppler mode of a 3D ultrasound probe.

In addition to imaging the needle, ultrasound has also been used to track target movements (Chevrie et al. 2018) and to visualise tissue ablation (Gerboni et al. 2017).

However, even though a 3D ultrasound probe is able to visualise the surgical site in 3D, the algorithm to process the images is computationally expensive and the images have slow frame rates (Waine et al. 2016, Ayvali & Desai 2015). Thus, a 2D ultrasound probe, which has a higher acquisition rate, is the current standard used in clinics (Ayvali & Desai 2015). Depending on the orientation of the needle in US images, there are two types of images: sagittal images and axial images (Waine et al. 2016). In a sagittal image, the needle is visualised within the plane of the US beams. The shape of the needle and the target can be easily visualised using this imaging mode.

An axial image, on the other hand, is a US image where the needle axis is perpendicular to the US beams. The cross section view of the needle in an axial US image has a tail-shape structure instead of a circular shape, which is referred to as comet-tail artefact (CTA) due to the acoustic impedance difference between the needle and soft tissue (Vrooijink et al. 2014). Needle shapes can be reconstructed using axial images by measuring the needle position at several insertion depths (Waine et al. 2016, Gerboni et al. 2017). To track the needle tip using axial images, the US probe is attached to a robotic platform that is moved with the same speed as the needle (Lehmann et al. 2018, Carriere et al. 2018, Fallahi et al. 2017, Khadem et al. 2017, Li, Jiang, Liang, Yang, Yu & Wang 2017, Abayazid et al. 2016, Moreira & Misra 2015, Abayazid et al. 2015). Full pose of the needle can be estimated by using an assumption that there is no twist (Vrooijink et al. 2014). Since axial images only track the needle tip, Moreira & Misra (2015) scanned the tissue before needle insertion using the US probe to measure the target and obstacle positions. By adding one more degree-of-freedom to the robotic platform to rotate the US probe with respect to its axis, the probe can be used to perform both sagittal and axial imaging (Ayvali & Desai 2015).

Additionally, ultrasound images have also been used to obtain tissue stiffness information. Neubach & Shoham (2010) used tissue movement in front of the needle tip, which was visualised using ultrasound sagittal images, to classify tissue stiffness. The shape of the needle inside the

tissue has also been used to estimate the tissue stiffness. Using sagittal images to obtain the needle shape, Lehmann et al. (2018) calculated the tissue stiffness using energy method while the needle was moved laterally.

### MRI

The high tissue contrast of MRI makes it an ideal imaging modality to perform preoperative imaging. However, to use it intraoperatively, robotic systems require MR compatibility in its actuation and sensorisation. Due to the long acquisition time of MRI, images have been used after needle insertion to measure the targeting error (Su et al. 2016, Krieger et al. 2011). Seifabadi et al. (2016) designed a master-slave robotic system for continuous MRI guidance procedures. The purpose of this system is to reduce the need of moving the patient in and out of the scanner during the procedure. Images from the MRI can be generated at 2 frames/s which is sufficient for visual feedback to the operator. However, the needle tip has an artefact with a diameter of a few millimetre, which makes tip tracking with a high accuracy difficult.

### X-ray

X-ray based imaging modalities, such as fluoroscopy and CT, have also been used for image guidance in steerable needle systems. Bui et al. (2016) used an X-ray machine to measure the deflection of the needle during characterisation of their steerable needle system in *ex-vivo* tissue. Robert et al. (2013) used a CT scan to image needle deflections in soft tissue phantoms and investigated the force acting on the needle to produce such deflections. The targeting accuracy of a concentric tube needle that consists of two tubes has also been investigated using a CT scan by comparing the planned and actual path of the needle (Torabi et al. 2014). Glozman & Shoham (2007) and Shahriari et al. (2017) tracked the needle tip using a C-arm fluoroscopy system. C-arm fluoroscopy is a promising real time imaging modality due to its ability to achieve fast imaging (3-15 frames/s). Even though it has relatively fast frame rates, Glozman & Shoham (2007) performed intermittent imaging because of the blur of the image if taken

while the needle is moving. One factor that limits the use of X-ray based imaging modalities is ionising radiation to patients and medical staffs during a lengthy procedure.

### 2.5.2 Embedded Sensors

In addition to the use of imaging modalities, sensors embedded either in the needle or in the robotic platform have also been used to provide information about tip positions, forces, and needle shapes.

#### Electromagnetic Tracker

Electromagnetic (EM) tracker has been used to track the needle tip (Chevrie et al. 2018, Shahriari et al. 2017, Patil et al. 2014, Rucker et al. 2013, Ko & Rodriguez y Baena 2013). Five and six degree-of-freedom (DOF) EM tracking sensors have been used for measuring the position and orientation of the needle tip. Compared to six DOF EM sensors, five DOF EM sensors have a smaller diameter. However, they are unable to measure the rotation of the needle with respect to its longitudinal axis. For a needle that has high torsional stiffness, a rotation encoder in the base of the needle can be used to measure the needle twist angle (Shahriari et al. 2017, Chevrie et al. 2018). However, for a long bevel-tipped needle with duty cycle spinning, the use of six DOF EM sensors is needed to compensate for torsional wind up (Swaney et al. 2015). The Em tracker can be used either in a transparent tissue phantom or in real tissue. The measurements from an EM tracker have also been combined with other imaging modalities, such ultrasound (Chevrie et al. 2018), and CT (Shahriari et al. 2017). One of the drawbacks of EM trackers is that the accuracy of the tracker is sensitive to the presence of ferromagnetic materials in the workspace (Abayazid, Kemp & Misra 2013).

#### Force and Torque Sensor

In addition to needle tip tracking, the knowledge of interaction forces during needle insertion could improve the targeting accuracy of steerable needles (Abolhassani, Patel & Moallem 2007).

The interaction force can be classified into tissue puncturing, tissue cutting, needle-tissue friction, and tissue deformation (Rossa & Tavakoli 2017). To measure the interaction forces and torques, a six DOF commercially available force and torque sensor is usually used at the base of the needle (Chevrie et al. 2018, Lehmann et al. 2018, Rossa et al. 2017, Misra et al. 2010, Neubach & Shoham 2010, Glozman & Shoham 2007, Abolhassani, Patel & Moallem 2007). Abolhassani, Patel & Ayazi (2007) used the information from the reaction forces and moments at the base of the needle to estimate the needle deflection. At the beginning of the insertion, the needle was moved laterally to estimate the tissue Young's modulus to improve deflection prediction. Based on this work, Rossa et al. (2017) introduced a data driven model to predict tissue deflection based on the force and torque measurements at the needle base combined with the insertion depth and rotation angle of the needle. Even though the model requires a large database to train it to be accurate, it predicts in-plane and out-plane deflection in heterogeneous tissue with $< 2$ mm accuracy. The force sensor in the needle base has also been used to improve the safety of needle insertion procedures. Glozman & Shoham (2007) and Neubach & Shoham (2010) measured the lateral force of a base-manipulation steerable needle to show that closed-loop control does not significantly increase the reaction forces at the needle base. Chevrie et al. (2018) proposed a needle insertion procedure that compensates for tissue movement due to physiological motion of the patient. The movement compensation could reduce the lateral force due to large tissue motion, lowering the risks of tearing tissue.

**Fibre Bragg Grating (FBG)**

Fibre Bragg Grating (FBG) sensors have also been used as a sensoritation method in steerable needles. An FBG is a distributed reflector constructed along an optical fibre length (Hill & Meltz 1997). The FBG reflects a wavelength as a function of the spacing between each grating and transmits other wavelengths. Because the reflected wavelength of the FBG can be shifted by a change in the grating period, it can be used as a mechanical sensor of temperature, strain, and force (Iordachita et al. 2009, Antonio-Lopez et al. 2014, Westbrook et al. 2015). In the field of steerable needles, several researchers have used FBGs as a shape sensing modality by computing the needle's shape from the strain measurements (Li, Jiang, Liang, Yang, Yu &

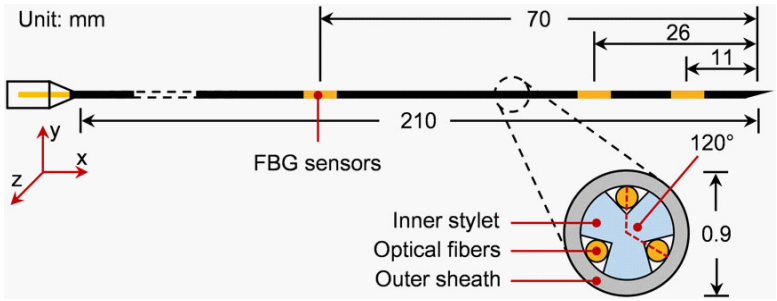


**Figure 2.10:** Illustration of a needle embedded with three optical fibres. In each fibre, fibre Bragg grating sensors were located at three axial positions: 11, 26, and 70 mm from the tip of the needle. Reprinted, with permission, from Li, Li, Gonenc, Duan & Iordachita (2017) ©2016 John Wiley and Sons

Wang 2017, Xu et al. 2016, Henken et al. 2014). To achieve three-dimensional shape sensing, at least three fibres are required (inset in Figure 2.10). The fibres are radially positioned at a distance from the axis of the needle. With a bending moment applied to the needle, each fibre experiences a different strain. This strain is measured via the FBG and is then used to compute the shape of the needle. To obtain the whole shape, FBGs are located in at least two different axial locations along the needle (Figure 2.10). In addition to FBG-based shape sensing, Xu et al. (2016) developed a force-curvature model to measure the force at the tip of the needle based on its shape. Li, Li, Gonenc, Duan & Iordachita (2017) detected the change of the tissue mechanical properties using the strain measurements of the FBG sensor that is close to the tip of the needle.

### Other Embedded Sensors

In addition to the aforementioned sensing modalities, there are other sensing systems that have been implemented in steerable needles: optical tracking, OCT, and hall effect sensing. Carriere et al. (2018) used an optical tracker to measure the insertion depth for a surgeon-in-the-loop needle insertion system. In this system, the surgeon inserted the needle manually through a trocar that rotated the needle automatically to steer. Ayvali et al. (2012) studied the use of OCT in an active steerable needle system to perform *in-situ* diagnosis. However, their study only showed the feasibility of using OCT probe in a bending needle. Reed et al. (2009) measured the lag between the needle base and the needle tip while the needle rotated inside the tissue.

The lag was measured by comparing the encoder reading at the needle base with the hall effect sensor measurements at the needle tip. They showed that torsional friction causes more than 45° discrepancy between the base and the tip angles.

Since each imaging modality and embedded sensor has its own advantages and disadvantages, measurements from several sensors or imaging modalities could be combined to improve the targeting accuracy of steerable needle systems. Therefore, in the literature, it is common to find a steerable needle system that was equipped with several sensing systems (Table 2.2). Table 2.2 shows the sensorisation methods that were used in steerable needles, which are discussed in this section. The table could be used to suggest the possible combination of sensing systems in steerable needles.

## 2.6 Conclusion

In this chapter, the problem of vessel puncture during percutaneous brain surgery was introduced, followed by the use of embedded sensors used to reduce the risk of haemorrhage. Ultrasound based systems were found to offer deeper penetration depth into brain tissue compared to the light-based systems. Deeper depth penetration means that a vessel can be detected earlier, which is advantageous. However ultrasound transducers are difficult to miniaturise, which hinders their deployment inside the needle. On average, a light-based system could detect a vessel that lies 1 mm away from the probe. This distance is enough to prevent vessel puncture as long as the needle is inserted slowly during the procedure.

Following a review of sensing systems, this chapter explained major needle steering designs, which have been used to avoid vessels along the insertion path. Bevel-tipped needle designs have been widely used due to their simple construction and ability to follow-the-leader. However, the need to rotate the needle about its insertion axis may hinder its application in delicate tissue structures such as in the brain. Programmable bevel-tip needles, on the other hand, do not need to be rotated in order to steer. In addition, the multi-segment design of PBNs can be deployed with a reciprocal motion actuation strategy that offers the potential to reduce tissue

disruption. Although any steerable needle system has the ability to avoid an obstacle, to date there is no reported use of a steerable needle system with embedded sensors to avoid a vessel along its path. Indeed, the main focus areas for steerable needle sensing to date have been position tracking, force sensing, and shape sensing.

This thesis discusses the sensorisation of PBNs to solve the clinical need to avoid haemorrhages. A detection method based on measurements from forward looking optical sensors embedded within the steerable needle segments is developed to infer vessel pose. Vessel pose information provides the necessary knowledge to plan and execute a subsequent avoidance strategy. This method could also be applied to other steerable needle designs, and is the subject of subsequent chapters.

**Table 2.2:** Steerable needle sensorisation; US: ultrasound, EM: Electromagnetic Tracker; FBG: Fibre Bragg Grating; Cam: Camera; F/T: Force and Torque Sensor; Oth: Other sensing modalities

| Reference | Sensing Modalities | | | | | | | | System Explanation |
|---|---|---|---|---|---|---|---|---|---|
| | US | MRI | CT | EM | FBG | Cam | F/T | Oth | |
| Chevrie et al. (2018) | • | | | • | | | • | • | 5 DOF EM sensor to track the needle tip, the motor encoder to measure the rotation about needle axis, 3D US to track the target |
| Lehmann et al. (2018) | • | | | | | • | • | | Predicting the Young's Modulus of the tissue based on needle deflection to improve the accuracy of needle insertion |
| Carriere et al. (2018) | • | | | | | | | • | Optical tracker to measure the insertion depth combined with a 2D US probe to track the needle tip |
| Gerboni et al. (2017) | • | | | | | | | | A 2D US probe tracked with EM sensor, scanned manually to get 3D volume images. The needle is segmented manually. |
| Rossa et al. (2017) | • | | | | | | • | • | A 6 DOF force and torque sensor in the needle base combined with insertion depth and rotation angle measurements to predict needle deflection based on a data driven model |
| Shahriari et al. (2017) | | | • | • | | | | • | 5 DOF EM tracker combined with intermittent CT images. The rotation of the needle with respect to the needle axis is measured using rotary encoder assuming there is no twist |
| Li, Li, Gonenc, Duan & Iordachita (2017) | | | | | • | | | | Shape reconstruction using FBG. Interaction force measured using the distal end FBG sensors |
| Fallahi et al. (2017) | • | | | | | | | | a 2D US probe is attached into a linear platform to track the needle tip |
| Khadem et al. (2017) | • | | | | | | | | a 2D US probe is attached into a linear platform to track the needle tip |
| Li, Jiang, Liang, Yang, Yu & Wang (2017) | • | | | | | | | | a 2D US probe is attached into a linear platform to track the needle tip |
| Su et al. (2016) | | • | | | | | | | MRI to image the final path of the robot |
| Seifabadi et al. (2016) | | • | | | | | | | 2 image per second FSPGR MRI for visual feedback |
| Bui et al. (2016) | | | • | | | • | | | A camera for tissue phantom testing, and X-ray to detect the needle *ex vivo* |
| Waine et al. (2016) | • | | | | | • | | | Needle shape reconstruction based on successive axial US images. The cameras were used to validate the shape reconstruction |
| Xu et al. (2016) | | | | | • | | | | Curvature, force, and torque measurements using FBG |
| Abayazid et al. (2016) | • | | | | | | | | A "D US probe embedded at a robotic platform to track the needle tip |
| Vrooijink et al. (2014) | • | | | | | | | | A 2D US probe was attached in a robotic platform, the features of the US images were extracted based on hough transform |
| Moreira & Misra (2015) | • | | | | | | | | a 2D US probe is used to scan the phantom before insertions to define obstacles and track the needle tip during insertion |

**Table 2.2:** Steerable needle sensorisation; US: ultrasound, EM: Electromagnetic Tracker; FBG: Fibre Bragg Grating; Cam: Camera; F/T: Force and Torque Sensor; Oth: Other sensing modalities

| Reference | Sensing Modalities | | | | | | | | System Explanation |
|---|---|---|---|---|---|---|---|---|---|
| | US | MRI | CT | EM | FBG | Cam | F/T | Oth | |
| Ayvali & Desai (2015) | • | | | | | | | | A 2D US probe to measure the shape and track the tip of the needle by changing the US images from sagittal to axial |
| Abayazid et al. (2015) | • | | | | | | | | A 2D US probe is attached in a 5DOF robotic platfrom to scan and track the needle inside curved surface |
| Adebar et al. (2014) | • | | | | | | | | 3D US power Doppler imaging mode to measure the position of the needle |
| Swensen et al. (2014) | | | • | | | • | | | Two cameras for stereo imaging were used during transparent phantom experiments, C-arm fluoroscopy was used for biological tissue to track the needle tip |
| Henken et al. (2014) | | | | | • | | | | FBG for shape measurement |
| Torabi et al. (2014) | | | • | | | | | | CT scan was performed after each intervention procedure to compare planned and actual path |
| Patil et al. (2014) | | | | • | | | | | 5 DOF EM tracker to track the needle tip pose |
| Robert et al. (2013) | | | • | | | | | | CT slices to measure needle deflection |
| Bernardes et al. (2013) | | | | | | • | | | Imaging feedback from a camera |
| Rucker et al. (2013) | | | | • | | | | | 5 DOF EM tracker to track the tip |
| Abayazid, Roesthuis, Reilink & Misra (2013) | • | | | | | • | | | A Camera and a 2D US probe in sagittal mode to track the needle tip |
| Swaney et al. (2013) | | | | | | • | | | A camera to measure needle curvatures |
| Ko & y Baena (2013) | | | | • | | | | | EM tracker to track the needle tip |
| Ayvali et al. (2012) | | | | | | • | | • | Two cameras in stereo configuration to measure the needle pose, and OCT for *in situ* diagnostic |
| Misra et al. (2010) | | | | | | • | • | | Force sensor to measure tool tissue interaction and two cameras in stereo configuration for tracking |
| Neubach & Shoham (2010) | • | | | | | | • | | Sagittal US images to track the needle, tissue stiffness prediction based on tissue movement in front of the needle tip, and force and torque measurements during insertion |
| Reed et al. (2009) | | | | | | | • | • | Hall effect sensor to measure the lag between the base and the tip inside the tissue while the needle is rotated |
| Glozman & Shoham (2007) | | | • | | | | • | | A fluoroscopic image was taken to plan the insertion. Intermittent fluoroscopy images were taken during the insertion |

**Table 2.2:** Steerable needle sensorisation; US: ultrasound, EM: Electromagnetic Tracker; FBG: Fibre Bragg Grating; Cam: Camera; F/T: Force and Torque Sensor; Oth: Other sensing modalities

| Reference | Sensing Modalities | | | | | | | | System Explanation |
|---|---|---|---|---|---|---|---|---|---|
| | US | MRI | CT | EM | FBG | Cam | F/T | Oth | |
| Abolhassani, Patel & Ayazi (2007) | • | | | • | | • | • | | US for studying internal tissue deformation, A camera to image needle deflection at the entry point, 5 DOF EM tracker to track the needle tip position, 6 DOF force and torque to measure the force and moments acting on the needle |

# Chapter 3

# Manufacturing of a Programmable Bevel-Tip Needle

## 3.1 Introduction

Previously, Leibinger et al. (2015) used a 4 mm outer diameter functional prototype of the programmable bevel-tip needle, which was manufactured using additive manufacturing out of a rubber-like material, to investigate tissue motion due to needle deflection. The miniaturisation of the PBN down to $< 2.5$ mm in diameter is required so that the needle has a clinically viable size (Parittotokkaporn 2011). Consequently, materials and manufacturing strategies that would allow the overall diameter of the PBN to be reduced while taking into account sterility and the possibility of single-use must be investigated. The PBN's interlock mechanism is, however, difficult to produce using conventional subtractive manufacturing processes due to its tiny size diameter ($< 2.5$ mm) compared to its length (200 mm). Micromachining processes can produce very small features ($\approx 10$ $\mu$m). However, they typically have a working volume below 50 $\times$ 50 $\times$ 50 mm (Qin et al. 2010). Another manufacturing option is to use a milling machine. Even though manufacturing a 0.3 mm square groove along the length of a 1 mm diameter needle with 172 mm length can be performed using a milling machine (Roesthuis et al. 2014), to mill the PBN dovetail mechanism requires the use of a special cutting tool that has the same shape as

the male interlock mechanism (see Figure 2.9c), which is not commercially available. Another option is to change the PBN design so that the interlock mechanism has the same shape as the available dovetail cutting tools on the market (e.g. Harvey Tool, Rowley, USA), which makes the cross section design suboptimal (Leibinger et al. 2014).

In this Chapter, two manufacturing strategies are discussed. Firstly, the relationship between the build angle, support structure interval, and geometric accuracy to optimise the cost and time required to successfully build high aspect ratio parts using a Selective Laser Melting (SLM) machine have been investigated. Secondly, a manufacturing method for the polymer-based PBN that was eventually executed by our subcontractor using an extrusion process, is described. Finally, the development of a fixture to manufacture the bevel-tip for the extruded needle, which was developed by the author, is explained. Part of this Chapter is a revised version of the following conference publication:

- Vani Virdyawan, Joshua W. Giles, Richard J. van Arkel, Matthew Oldfield, and Ferdinando Rodriguez y Baena (2015). "High Aspect Ratio Additive Manufacturing of a Biologically Inspired Surgical Needle". In: *Proceeding of Design of Medical Devices Conference Europe Edition 2015*, pp. 9-10.

## 3.2 Additive Manufacturing of a High Aspect Ratio Part

Additive manufacturing (AM) is a rapidly evolving process that is suitable for producing complex structures that are needed in small quantities (Vayre et al. 2012). Additive manufacturing of a rubber-like material played an important role in the development of the biologically inspired programmable bevel-tip needle, where functional prototypes with a diameter of 12 mm (Ko et al. 2011) down to a 4 mm diameter (Leibinger et al. 2015, Burrows et al. 2017) had been manufactured using this method. The first effort to miniaturise the 4 mm PBN down to a 2.5 mm diameter was performed using additive manufacturing as well. However, instead of using the AM of a rubber-like material, a metal-based additive manufacturing machine was

chosen due to its ability to produce parts using a wide range of biocompatible materials, such as stainless steel, cobalt-chrome, titanium, and nitinol.

Selective Laser Melting (SLM) is a method of additive manufacturing in which a thin layer ($\approx 0.03$ mm) of metal powder is selectively melted using a laser beam. The laser has adequate energy to rapidly melt sections of the powder, allow them to coalesce and subsequently solidify. However, this rapid heating and cooling generate residual stresses in the solidified component (Mercelis & Kruth 2006), which can produce warping if it is not well anchored to the build platform (Mumtaz et al. 2011). Support structures are needed to anchor portions of the part not in direct contact with the build platform, especially in cases of thin parts or parts with overhanging structures. Unfortunately, the higher the number of support structures, the more difficult it is to remove the part from the build platform.

The PBN has a high aspect ratio (the ratio of its length to diameter is $\approx 88{:}1$). As a result, the needle cannot be built perpendicular to the build platform (i.e. vertically) as it would exceed the system's maximum build height, require very large volumes of expensive yet unused metal powder, and result in excessive build time. Additionally, building in the vertical direction can cause high aspect ratio parts to bend during the building process which also provides an upper limit. As an alternative, the needle can be manufactured parallel or at an acute angle to the build platform. However, changing the build orientation will change the sliced data cross section in each layer which will affect the number of support structures and time needed to build the part (Mumtaz et al. 2011).

### 3.2.1 Related Works

Several research groups (Kruth et al. 2005, Fahad & Hopkinson 2012, Abdel Ghany & Moustafa 2006, Castillo 2005, Byun & Lee 2003, Moylan et al. 2012) have developed methods to assess the performance of additive manufacturing processes using a benchmark part. Although each benchmark part has its own characteristics and geometry, all are primarily interested in characterising the system's accuracy and the minimum feature size that can be built. This information has been used as a guideline for designing parts for manufacture using AM. However, in the

case of manufacturing a high aspect ratio part (e.g. a small diameter with a long length) this information is insufficient because this type of part is susceptible to warping and effects related to its orientation on the build platform that are not characterised by the above benchmark parts. Another benchmark part has been developed by Vora et al. (2013) to evaluate the maximum length of an overhang structure that can be built without warping. The part has a range of overhang lengths with successively longer overhang structures but does not include variable build angles.

### 3.2.2 Material and Methods

#### Assessment of Renishaw AM250 machine

To determine the optimal manufacturing strategy for building a multi-segment needle, a benchmark part was developed that can give information regarding the optimum interval between support structures, the build angle with respect to the build platform, and the geometrical accuracy. The benchmark part has overhang lengths of 0.1 - 1.0 mm in intervals of 0.1 mm, overhang lengths of 1.0 - 2.0 mm in intervals of 0.2 mm, and a maximum overhang length of 5.0 mm. Each overhang structure has a semi-circular cross-section with a diameter of 1.2 mm to replicate a needle's geometry. The progressively longer structures are built above the previous overhang with an interval of 3.0 mm to minimise the required build height. These progressively longer overhangs can be used to determine the optimum distance between support structures by investigating the maximum length that can be built without warping. This maximum length is, however, influenced by the build angle with respect to the build platform and thus the benchmark part was designed with a range of angles (0 - 45° with an interval of 5°). Figure 3.1 shows the CAD model of the benchmark part.

After manufacture of the benchmark part, a set of measurements were taken using a calibrated optical microscope equipped with a digital camera (Zeiss - Axio Icc.1, Carl Zeiss AG, Oberkochen, Germany) to measure the level of warping and the geometry of the part. Using the known calibration (1038 x 1392 pixels, with 1.86 $\mu$m per pixel) of the microscope and a

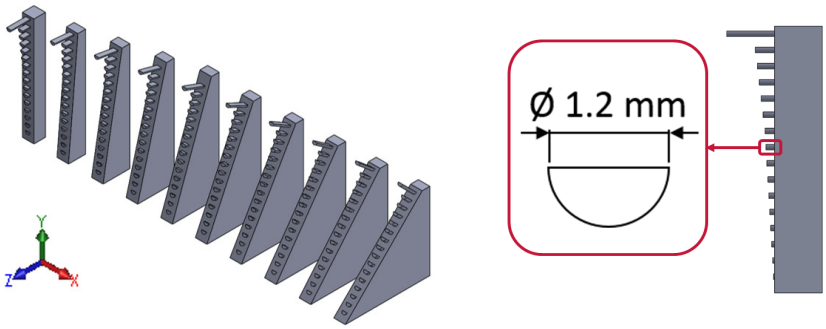


**Figure 3.1:** A CAD drawing of warping benchmark part for building the high aspect ratio surgical needle and the cross section of the overhang structure

transverse image of each overhang, the level of overhang warping was determined by recording the pixel location of a consistent point at the base of the overhang and another at its tip. The level of warping was then calculated as the difference (in $\mu$m) between the two pixels in a direction perpendicular to the overhang structure (Figure 3.2).

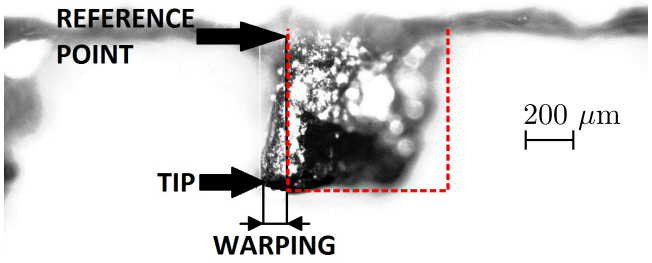


**Figure 3.2:** Warping measurement method using a calibrated microscope of an overhang structure with more than 100 $\mu$m warping. The dash line shows the shape of the overhang structure if there is no warping

The geometry of the overhang structure was assessed using a circularity measurement. The most common method to measure circularity is least - square circle (LSC), however this method can reject a good part due to a possible overestimation of form tolerance (Carr & Ferreira 1995). To avoid this, minimum zone circle (MZC) that minimize the maximum error between the data and the reference is used (Cioboata et al. 2012). Based on the MZC method, an object's circularity can be defined as the difference between two reference circles, one sufficiently large to encapsulate all deviations from the circular profile and one small enough that no deviations fall with it (Cioboata et al. 2012). The circularity measurement can be made by capturing a cross section image of the overhang structure. After filtering the image, the circularity profile of the cross section can be determined using an edge detection algorithm (Figure 3.3). A

procedure to find the MZC is described by Maresca et al. (2012).

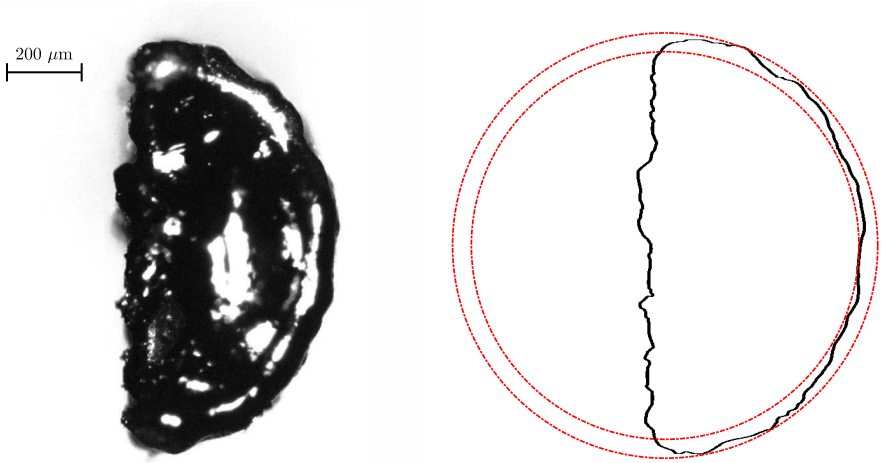


**Figure 3.3:** The cross section image of an overhang structure taken by a measurement microscope (left) and its circularity measurement using the MZC method (right)

### Needle Manufacturing

Using the data collected in Section 3.2.2, which characterise warping for a high aspect ratio part, an optimal build strategy was defined for our specific application; namely, a two-segment needle, with a diameter of 2.4 mm and 200 mm in length (Figure 3.4). Instead of a four-segment needle as described by Oldfield et al. (2014), the two part needle was chosen as a stepping stone to produce an optimized four-segment PBN using SLM. To define the optimal build strategy several factors are considered:

- To reduce build cost and time, build height should be minimised by building the part as parallel as possible to the build platform
- The interval between two support structures is chosen from the maximum overhang length that can be built with warping below an unacceptable minimum threshold
- The maximum build angle between the part and the build platform is constrained by the available material; whereby larger angles increase build height and thus required material

- The circularity measurement is used to determine the build angle such that critical features - in this case the needle interlock mechanism - are built within an acceptable geometric tolerance for the application.

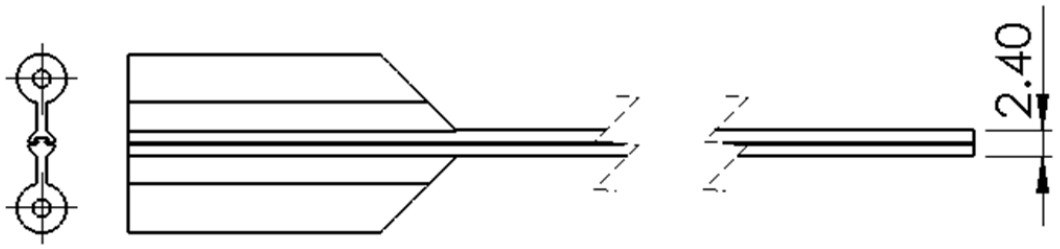


**Figure 3.4:** The drawing of the 2 part PBN. In addition to the central needle, note that each segment has a "wing" so that it can be pushed or pulled using a nitinol wire 1.6 mm in diameter connected to an actuation box

### 3.2.3 Results and Discussion

Table 3.1 and Table 3.2 show the warping and the circularity of each overhang structure. The circularity measurements were only conducted for overhang structures with <100 $\mu$m of warping because, for higher values of warping, the cross section is no longer sufficiently semi-circular (more than 20% of its diameter). A 5 mm overhang length cannot be built horizontally (0°) and exhibits very high warping (250 - 1200 $\mu$m) for 5° - 15°. Starting from 20°, the 5 mm overhang length can be successfully built. The unsupported structure without warping increases from 0.4 mm to 0.5 mm in length at a 20° build angle and increases further at 30° and 40° to 0.6 mm and 0.7 mm, respectively. The small value of warping (<100 $\mu$m) may be correlated to the slicing process of the CAD data which has 30 $\mu$m and the powder grain size (40 $\mu$m).

The circularity measurement for less than 100 $\mu$m warping shows for all parts, the circularity is not strongly related with warping. However, the circularity shows a significant difference between build angles (One-way ANOVA, F: 8.58, P value: <0.0001). This relationship can be seen in Table 3.2. The average circularity of each angle shows a higher build angle produces a better circularity profile. Therefore, to achieve improved accuracy a part should be built as near to vertical as possible given other constraints.

Based on the result of the benchmark part and the criteria to determine the manufacturing strategy several parameters were chosen. First, the maximum build angle can be selected based on the availability and cost of material required to fill the system's build chamber. In our case, this criterion dictates a maximum build height of 70 mm. Therefore, the maximum allowable build angle is equal to 17° due to the desired 200 mm needle length. Thus, suitable build angles for this criterion vary from 0° to 15°.

The second constraint that must be considered is the geometric tolerance required for proper operation of the manufactured part; in this case, the needle's interlock mechanism. By heuristically changing the size of the male and female interlock features, the interlock mechanism was found to function properly with a geometric error of $< \pm 60$ $\mu$m. Therefore, a 15° build angle was chosen as it was the only orientation capable of achieving the required accuracy.

Finally, given the selected build angle, the final parameter to be defined is the interval between support structures. This can be determined based on the chosen build angle and the data from Table 3.1. Specifically, the maximum overhang structure that can be built without warping is 0.4 mm. However, a 0.5 mm overhang length results in only 30 $\mu$m of warping which is equal to the metal powder particle size thus the overhang length can be extended to 0.5 mm. The first trial of this build strategy was used to manufacture a function PBN that has 70 mm in length (Figure 3.5) using a smaller machine to speed up the process. Although shorter than the final goal, this PBN is a proof of concept of the build strategy because has a similarly high aspect ratio (≈29:1) and allows evaluation of the functionality of the interlock mechanism.

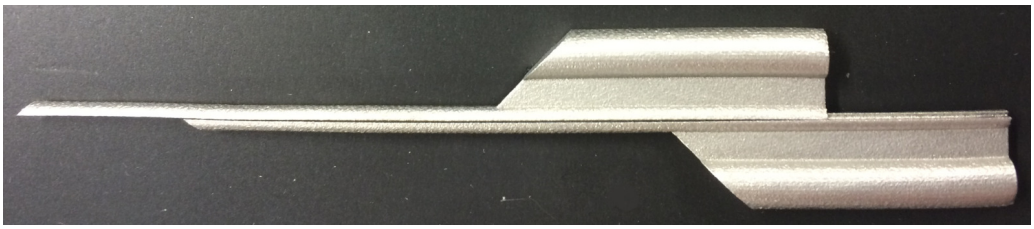

**Figure 3.5:** A two part needle with 70 mm in length has been built using the build strategy described in this Chapter

The results from the benchmark part can also be used to develop build strategies for manufacturing any part that has a high aspect ratio or has a high aspect ratio feature using SLM. By changing the build orientation with respect to the build platform the likelihood of warping

can be reduced. In addition, this reduces the required number of support structures thus increasing the surface quality of the part. In terms of geometric accuracy, a comparison between circularity profiles at 45°and 90° (vertical) build angles using paired t-test shows no significant difference (Figure 3.6). This findings provide greater freedom for manufacturing a part using the SLM process; particularly to manufacture medical devices that have intricate geometry.

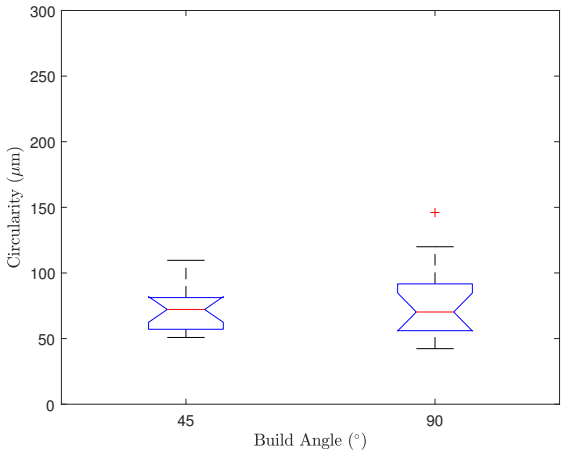


**Figure 3.6:** Circularity measurements boxplot of 45° and 90° build angle

## 3.3 Manufacturing Process for Polymer PBNs

The metal version of the PBN that was built using the manufacturing strategy described in section 3.2 was too stiff to be used as a steerable needle. Besides, a needle with a length of 200 mm could not be manufactured due to limitations in the build volume. Therefore, a second manufacturing process to produce the needle was explored.

Extrusion is a manufacturing process in which the materials are pushed into a die to produce a fixed cross-sectional area. One of the advantages of the extrusion process is its ability to produce various cross section shapes. A complex hollow shape can also be manufactured by adding a mandrel to the die (Zahid Qamar 2018). With these advantages, extrusion is a viable option to manufacture the PBN.

XOGRAPH ltd., an extrusion manufacturer based in Stonehouse, Gloucestershire, United Kingdom, was chosen as the subcontractor to produce the PBN out of a biocompatible polymer.

**Table 3.1:** The warping of the benchmark part in a different overhang lengths and build angles

| Overhang Length (mm) | Warping ($\mu$m) | | | | | | | | | |
|---|---|---|---|---|---|---|---|---|---|---|
| | 0° | 5° | 10° | 15° | 20° | 25° | 30° | 35° | 40° | 45° |
| 0.1 | 0 | 0 | 0 | 0 | 0 | 0 | 0 | 0 | 0 | 0 |
| 0.2 | 0 | 0 | 0 | 0 | 0 | 0 | 0 | 0 | 0 | 0 |
| 0.3 | 0 | 0 | 0 | 0 | 0 | 0 | 0 | 0 | 0 | 0 |
| 0.4 | 0 | 0 | 0 | 0 | 0 | 0 | 0 | 0 | 0 | 0 |
| 0.5 | 70 | 40 | 50 | 30 | 0 | 0 | 0 | 0 | 0 | 0 |
| 0.6 | 40 | 30 | 40 | 130 | 60 | 60 | 30 | 0 | 0 | 0 |
| 0.7 | 30 | 40 | 100 | 80 | 40 | 50 | 70 | 70 | 0 | 0 |
| 0.8 | 60 | 100 | 110 | 120 | 40 | 30 | 70 | 20 | 70 | 50 |
| 0.9 | 110 | 10 | 60 | 90 | 50 | 50 | 80 | 30 | 90 | 30 |
| 1.0 | 70 | 100 | 20 | 70 | 70 | 30 | 40 | 50 | 70 | 50 |
| 1.2 | 20 | 70 | 90 | 80 | 20 | 30 | 90 | 20 | 80 | 80 |
| 1.4 | 150 | 60 | 80 | 90 | 30 | 40 | 90 | 10 | 70 | 60 |
| 1.6 | 220 | 180 | 80 | 140 | 70 | 10 | 60 | 30 | 50 | 60 |
| 1.8 | 200 | 170 | 60 | 100 | 40 | 30 | 80 | 10 | 60 | 70 |
| 2.0 | 260 | 180 | 110 | 140 | 60 | -50 | 100 | 0 | 70 | 10 |
| 5.0 | N/A | 1150 | 260 | 320 | 80 | 70 | 80 | 0 | 200 | 180 |

**Table 3.2:** The average of cross section circularity for each build angle

| **Build Angle(°)** | 0 | 5 | 10 | 15 | 20 | 25 | 30 | 35 | 40 | 45 |
|---|---|---|---|---|---|---|---|---|---|---|
| **Circularity ($\mu$m)** | 136 | 152 | 128 | 111 | 111 | 106 | 89 | 86 | 81 | 69 |

The extrusion process that was performed by XOGRAPH ltd. to manufacture the PBN is included in this section for completeness.

### 3.3.1 Extrusion Process for Polymeric PBNs

The schematic diagram of the extrusion process to manufacture the PBN segment is shown in Figure 3.7. Firstly, the polymer in the form of granule was fed into the extruder. Inside the extruder, a rotating screw pushed the material towards the extruder head. The heat from a

heating element combined with the heat from the shearing energy between the granule and the rotating screw melted the polymer inside the extruder (Zahid Qamar 2018).

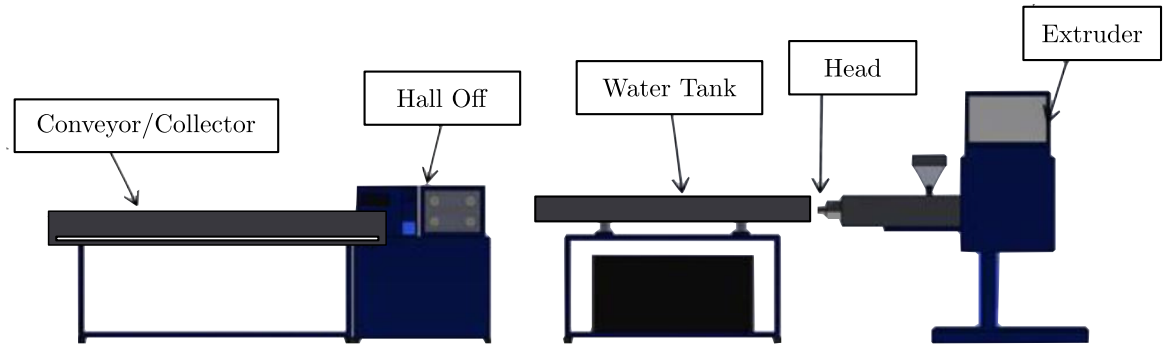


**Figure 3.7:** Schematic diagram of the extrusion process to manufacture the PBN. Image Courtesy: XOGRAPH, ltd.

An extrusion die that had a shape similar to the outer shape of the PBN segment was attached in the extruder head (Figure 3.8a). By passing the melted polymer through the die, the polymer had an interlocking, dove-tail, cross-section design (Figure 3.10b). To produce the working channel, a mandrel was added to the die (the red arrow in Figure 3.8a). Using the mandrel, a prototype with a single working channel (the earlier prototype as in Figure 2.9b) or even two working channels (Figure 3.8b) in each segment could be produced. The hall off then pulled the extruded material through a water tank to cool the polymer and solidify it. The tension during this pulling process was necessary to ensure the quality of the extruded part (Zahid Qamar 2018).

The PBN was manufactured by extrusion from clear flexible biocompatible polymers. During prototype development, several polymers with shore-A hardness ranging from 76 - 89 were extruded. After several iterations, the final prototype was manufactured from hy-vin® XT80730 (INEOS Compounds Aycliffe Ltd., Durham, United Kingdom) with an 89 shore-A hardness. A series of prototypes were successfully produced by XOGRAPH ltd.: a 4 mm diameter PBN with one working channel in each segment, a 2.5 mm diameter PBN with one working channel in each segment, and a 2.5 mm diameter PBN with two working channels in each segment. During the extrusion process of the PBN with two working channels, colour particles were added to colour code the segment (Figure 3.8b). Figure 3.9 showed the evolution of the PBN prototypes from the 12 mm diameter PBN manufactured using rapid prototyping process of rubber-like

material to the 2.5 mm colour coded extruded PBN with two working channels.

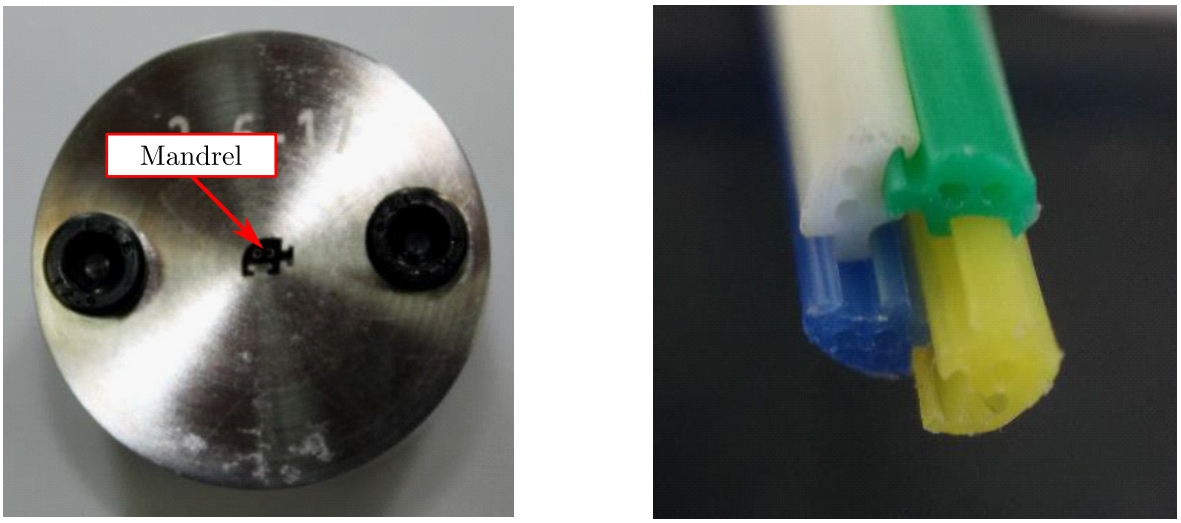


(a) (b)

**Figure 3.8:** a) The extrusion die that was attached into the extruder head. The red arrow shows the mandrel to produce two working channels in the PBN segment; b) A 2.5 mm colour coded PBN with two working channels in each segment. Image courtesy: XOGRAPH ltd.

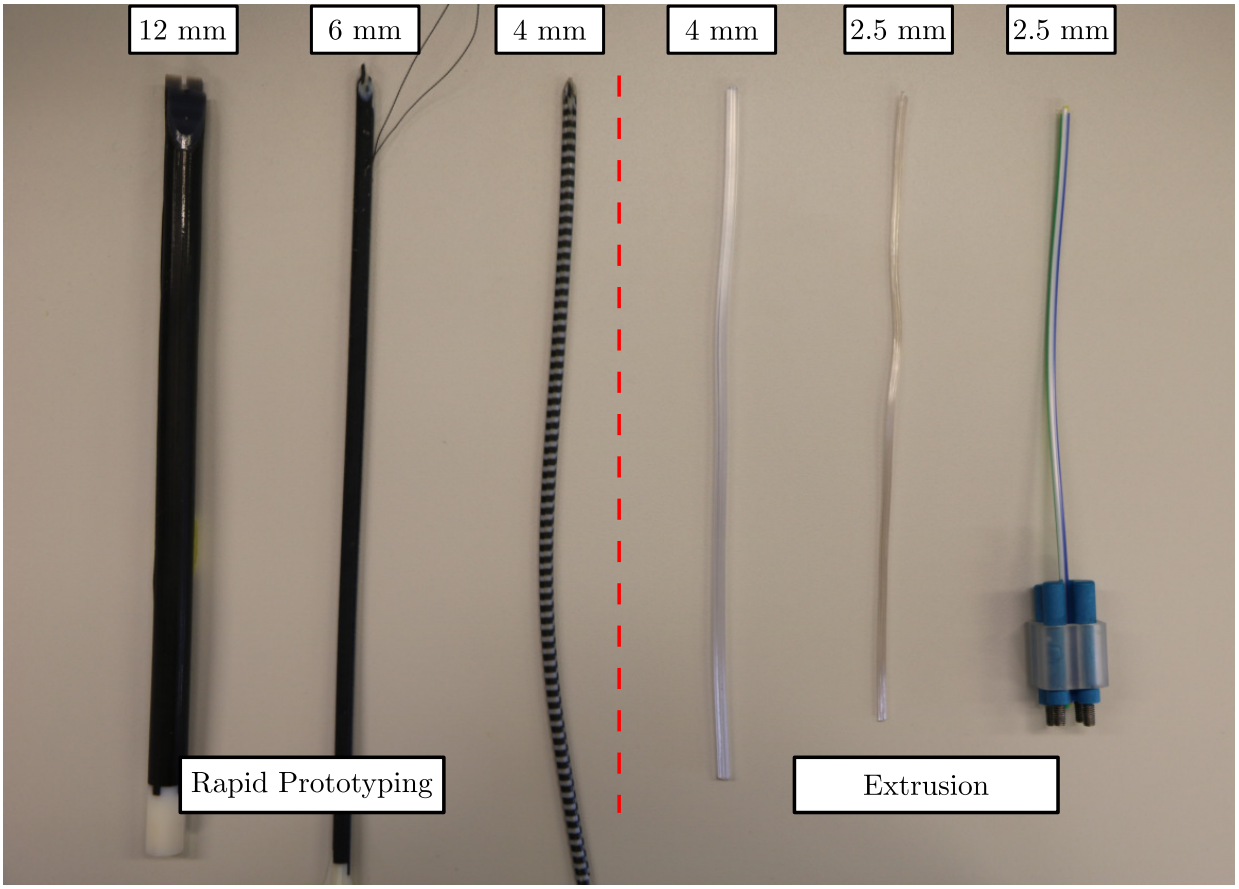


**Figure 3.9:** The PBN prototypes evolution from a 12 mm outer diameter needle manufactured using a rapid prototyping process (left) to a 2.5 mm outer diameter colour-code needle manufactured using an extrusion process (right)

The extrusion process produced a long PBN segment. This long segment was then cut into the required length (e.g. 200 mm). Four segments that had been cut were then assembled to produce a complete needle assembly. While cutting the extruded segment into the desired length was easily done, since the polymer was soft, it was challenging to manufacture its tip into a precise shape (i.e. 30° or 45° bevel tip angle). A fixture to produce the PBN's bevel tip accurately and consistently was then developed, which is described in the following section.

### 3.3.2 Fixture Design

The tip of the PBN should be designed to have a pyramid shape (Figure 3.10a) when the four segments of the PBN are aligned. The bevel tip angle of each segment was defined as the angle between the needle axis and the tip surface (see Figure 3.10a). To get this shape, each segment was cut in two cutting directions ($A_c$ and $B_c$ direction in Figure 3.10b). Figure 3.10b shows the projection of these cutting directions in the $xy$-plane. Both of these projections had a 45° angle with respect to the $y$-axis. The angle between each cutting direction to the $z$-axis was equal to the bevel tip angle of each segment.

Cutting the PBN segment accurately without any fixture was difficult since it bent while a cutting force was applied. The fixture was designed to minimise this bending during the cutting process. Using a fixture also ensured repeatability of the cutting direction. Ideally, it had the same shape as the external shape of the PBN segment. However, due to the small features of the interlocking mechanism, it may not be possible to manufacture using an additive manufacturing method. Therefore, a simplified version of the segment's external shape was used instead (Figure 3.11a).

To get the optimum fixture geometry, several geometries with 0.05 mm increments with the shape of Figure 3.11a were printed using a resin-based additive manufacturing machine (Form 2, Formlabs Inc., Somerville, Massachusetts, United States). After the printing, the segment was manually inserted into each geometry to find the best dimension where the segment could be easily inserted with less rotation. At the top of the fixture, two m3×0.3 mm threads were added manually so that the segment could be secured using a screw during the tip cutting

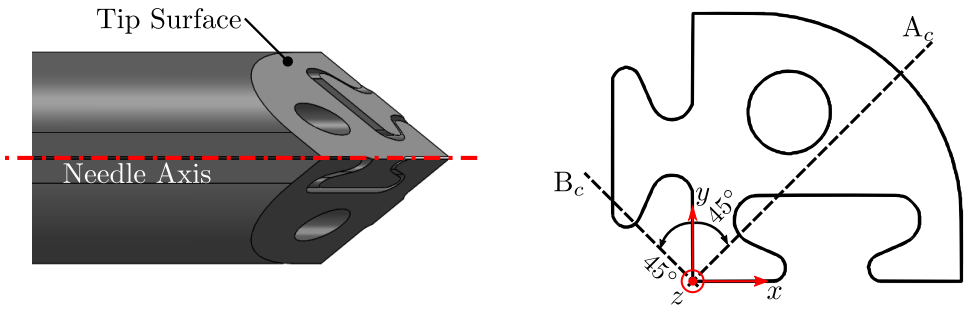


(a) (b)

**Figure 3.10:** a) The shape of the tip of the needle; b) The cross section of the needle with the projection of the cutting direction $A_c$ and $B_c$ in the $xy$-plane

process. Figure 3.11b shows the printed fixture that was utilised to cut the 4 mm PBN with 45° bevel tip angle.

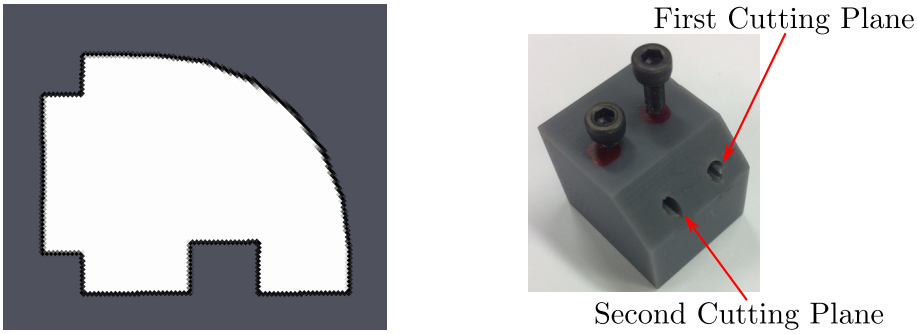


(a) (b)

**Figure 3.11:** a) The simplification of the segment's external shape used to manufacture the fixture; b) the manufactured fixture of the 4 mm PBN segment with a 45° bevel tip angle

The cutting processes were performed using a milling machine. The fixture was clamped into a milling machine with an angle equal to the desired bevel tip angle. A needle segment was then inserted into the fixture and was then cut. The segment was subsequently removed from the fixture, and the next segment was then cut without removing the fixture from the clamp. Bevel tip angle measurements were then carried out using a calibrated optical microscope equipped with a digital camera (Zeiss - Axio Icc.1, Carl Zeiss AG, Oberkochen, Germany).

### 3.3.3 Results and Discussion

Figure 3.12 shows angle measurements for the fixture and the bevel-tip of the 4 mm in diameter PBN, as an example. The desired bevel-tip angle was 45°. However, since the fixture was tilted

manually in the milling machine, an error of ≈1° was observed. Six needle segments were cut using this fixture. The bevel-tip angles of the segments were 45.8° ± 0.3°. In addition to 45° bevel-tip angle, a fixture with a 30° angle was also manufactured. The manufactured fixture has an angle of 31°, and the segments bevel-tip angle were 32° ± 0.5°. Even though the first cutting plane was cut using a milling machine, the second cut to remove the excessive part from the male interlock mechanism was performed manually using a knife while the segment was placed inside the second fixture hole. Table 3.3 summarises the bevel-tip manufacturing results.

**Table 3.3:** The comparison between the designed bevel-tip angle and the manufactured bevel-tip angle

| Designed Angle (°) | Fixture Angle (°) | Mean Bevel-Tip Angle (°) | Standard Deviation (°) |
|---|---|---|---|
| 30 | 31.0 | 32.0 | 0.4 |
| 45 | 45.8 | 45.8 | 0.3 |

The results show that the method described here could be used to manufacture a consistent bevel-tip angle with a variability of less than 1°. The accuracy of the bevel-tip angle depends on the fixture angle. The tilting of the fixture in the milling machine was performed manually. Therefore, after removing the fixture from the milling machine, there might be differences in the fixture angle if it was clamped in the machine again to perform another tip cutting. To remove this inconsistency, the fixture holes can be three-D printed in the desired angle directly. With this method, the variability of the angle only depends on the accuracy of the additive manufacturing machine used to build the fixture.

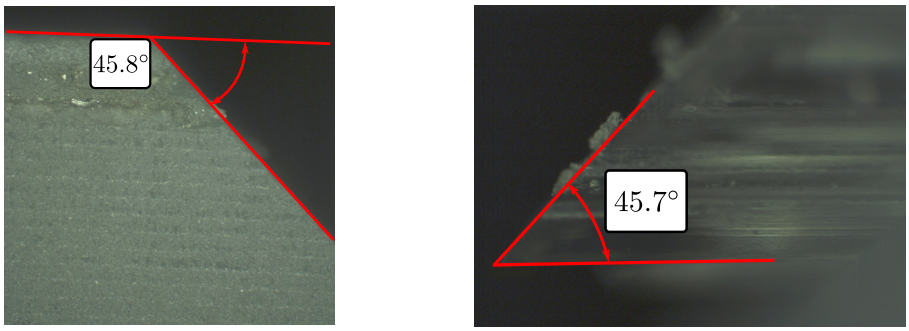


**(a)** **(b)**

**Figure 3.12:** Measurements of the a) fixture angle, and b) bevel-tip angle using optical microscope (Zeiss - Axio Icc.1). The angle of the fixture is 45.8° and the bevel tip angle is 45.7°

## 3.4 Conclusion

To be viable for clinical application, miniaturisation of the PBN from 4 mm to a diameter to $< 2.5$ mm was required. Two approaches were considered to miniaturise the needle: using metal additive manufacturing and using an extrusion process. In this chapter, the challenge of producing a needle that has a high aspect ratio using metal additive manufacturing has been discussed and solved using a benchmark part to develop the optimised build strategy. Even though a 70 mm length PBN was built successfully utilising the manufacturing strategy developed in section 3.2, the needle was too stiff to be used as a steerable needle. Therefore, an extrusion process was chosen to manufacture the miniaturise PBN, which was completed in partnership with a commercial extrusion manufacturer, XOGRAPH ltd.

Using a fixture, consistent and accurate bevel tips were also achieved. Since the fixture was built using a resin-based additive manufacturing machine, a new fixture for different bevel tip-angles can easily be produced. This advantage can speed up the prototyping process to identify the optimum bevel tip angle of the PBN. In Chapter 4 and Chapter 5, the polymer PBNs with manufactured bevel tip segments were embedded with forward-looking sensors to detect the presence of a vessel during insertion. Using these sensors, a vessel that cannot be detected during preoperative imaging can be avoided.

# Chapter 4

# Laser Doppler Flowmetry for Blood Vessel Detection with a Programmable Bevel Tip Needle

## 4.1 Introduction

Each segment of the Programmable Bevel Tip Needle (PBN) has a working channel that can be used to insert optical fibres for imaging or diagnostics. This working channel has a diameter of 0.3 and 0.6 mm for the 2.5 mm and the 4 mm diameter PBN, respectively. The diameter of the working channel dictates the maximum size of the sensor that can be embedded in the PBN. As shown in Table 2.1, light-based systems are more suitable to be inserted in the PBN.

This chapter is organised as follow. Firstly, a feasibility study of using forward-looking sensors based on Laser Doppler sensing in the 2.5 mm diameter programmable bevel-tip needle is discussed. The tip of the needle was manufactured using the method explained in Chapter 3.3. Secondly, an algorithm is presented, which enables prediction of the vessel orientation and position using two sensors embedded within the needle, with experimental results using the proposed algorithm discussed. This chapter concludes with a discussion and summary of the

main findings.

Contents presented in this chapter have been reproduced with permission from IOP Publishing from the following publication:

- Vani Virdyawan, Matthew Oldfield, and Ferdinando Rodriguez y Baena (2018). "Laser Doppler sensing for Blood Vessel Detection with a Biologically Inspired Steerable Needle". In: *Bioinspiration and Biomimetics*, 13:2, p 026009. ©IOP Publishing 2018.

## 4.2 Single Channel Laser Doppler Flowmetry Characterisation

Laser Doppler Flowmetry (LDF) monitoring systems are commonly used to monitor microcirculation (i.e. circulation in tiny vascular capillaries). Since light is scattered inside the tissue, determining an absolute perfusion value using LDF is not possible. Brownian motion of latex particles suspended in water is used as a standard to calibrate an LDF system (Fredriksson et al. 2010) (referred as motility standard). Therefore, an LDF monitor measures relative perfusion value with an arbitrary unit (AU). Compared to other light-based vessel detection systems, OCT, LDF, and CGD could differentiate between blood vessels and blood in the interstitium from a minor injury without the need of injecting any fluorescent dye into the patient. The simulation results of Fredriksson et al. (2009) showed that the measurement range of LDF possesses a large off-axis detection range compared to OCT and CGD (up to a few mm for LDF, 10 $\mu$m for OCT, and 40 $\mu$m for CGD). Consequently, as a feasibility study, a single channel commercially available laser Doppler system (OxyFlo$^{TM}$, Oxford Optronix, Abingdon, UK), with a bare-fibre type probe (NX-BF/F, Oxford Optronix, Abingdon, UK) was chosen as the sensor (Figure 4.1a), since an offset exists between the centre of the PBN lumens and the centre of the needle itself (see Figure 2.9c).

In this study, LDF is used to detect the presence of larger vessels, with a diameter $> 0.2$ mm (Huang et al. 2013). The Doppler probe that was used consists of two fibres, one for

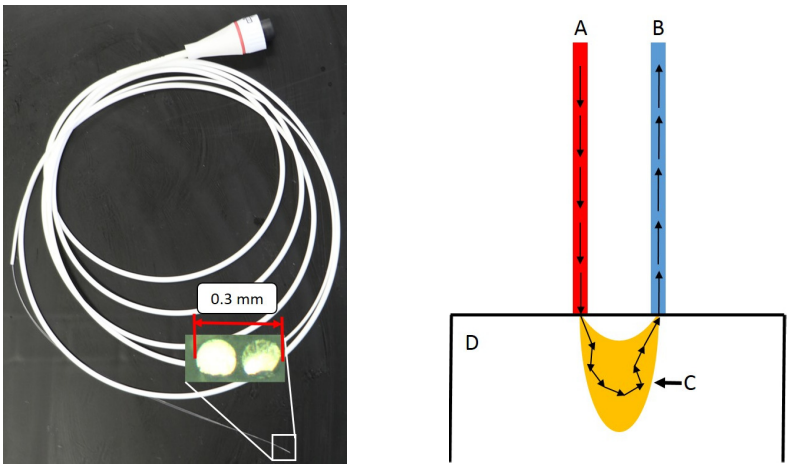


**(a)** **(b)**

**Figure 4.1:** a) A bare-fibre type probe (NX-BF/F, Oxford Optronix, Abingdon, UK) with its corresponding cross-section (inset); b) LDF probe schematic diagram. Light is delivered through an illumination fiber, scattered in the substrate and collected using a collection fibre. A:Illumination fiber, B: Collection fiber, C: Scattered light, D: substrate

illumination and the other for collecting the light (Figure 4.1b). In Fredriksson et al. (2009) it was shown that, for 0 to 1.2 mm fibre separation (i.e. the centre to centre distance between fibres), the larger the separation between source and collector fibres, the deeper the source of the reflected signals that could be detected. Due to the lumen size of each needle segment (0.30 mm, Figure 2.9c), the probe that was used during the experiment had a tip length of 60 mm, with a diameter less than 0.30 mm. Both the illumination and collection fibres had a diameter of 0.15 mm, with 0.15 mm fibre separation. The probe should have the ability to detect a vessel located in front of the tip of the needle. To verify the use of the probe as a vessel detector able to inform an eventual puncture avoidance system, the measurement range of the probe was firstly characterised to comply with the requirements of having $>$ 0.67 mm depth detection, and $>$ 0.88 mm off-axis detection (Figure 4.2).

### 4.2.1 Materials and Methods

The sensing capabilities of the probe were tested using a phantom that mimicked the optical properties of a blood vessel inside human grey matter. In order to achieve the 0.75 $mm^{-1}$ reduced scattering coefficient of human grey matter (Yaroslavsky et al. 2002), 3 g/L titanium

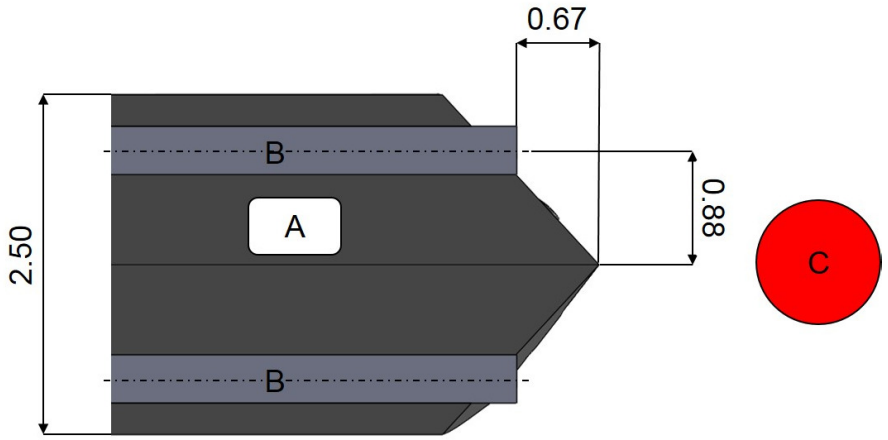


**Figure 4.2:** Minimum requirements for the detection range of the probe that is used for vessel detection in the PBN. A: the PBN, B: Optical fibres, C: Blood vessel

dioxide ($TiO_2$) (Akarçay et al. 2012) was added to 4.5% by weight gelatine, achieving a measured Young's Modulus of 7 kPa (Burrows et al. 2013), which is in the range of measurement taken for grey matter (Franceschini 2006). Compression tests were performed to compare the stiffness of the phantom with $TiO_2$ and the stiffness of the phantom without $TiO_2$. Each sample was prepared in a cylinder shape with a diameter of 30 ± 1 mm and a height of 11 ± 1 mm. Figure 4.3 shows the results of the compression test. The force and displacement curves for both samples show a good agreement, indicating that both phantoms have a similar stiffness.

A capillary tube with an outer diameter of 0.9 mm and an inner diameter of 0.6 mm was used as a blood vessel phantom, while the blood surrogate was milk, with 1.5% fat content (Öberg 1999). In here, depth detection is defined as the distance between the probe and the outer surface of the tube, while the off-axis (lateral) distance is defined as the distance between the centre axis of the tube and the centre axis of the probe. To test the measurable depth of a vessel below the gelatine surface, the capillary tube was placed at a gradient ($\theta_v$) inside the gelatine. The maximum depth detection range was investigated by scanning axially above the tube on the gelatine surface (Figure 4.4a). The off-axis detection range was measured by moving the probe laterally across the tube's axis (Figure 4.4b). The Doppler probe was held inside a capillary tube in a two degree-of-freedom (DOF) precision linear stage (Figure 4.5).

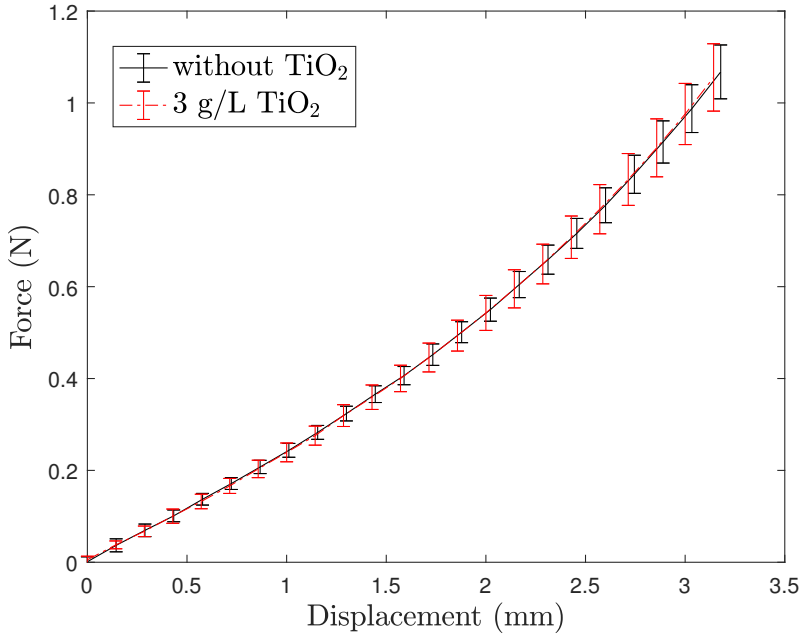


**Figure 4.3:** Compression tests results of phantom with 3g/L $Ti0_2$ (red dash-dot line) and without $TiO_2$ (solid black line)

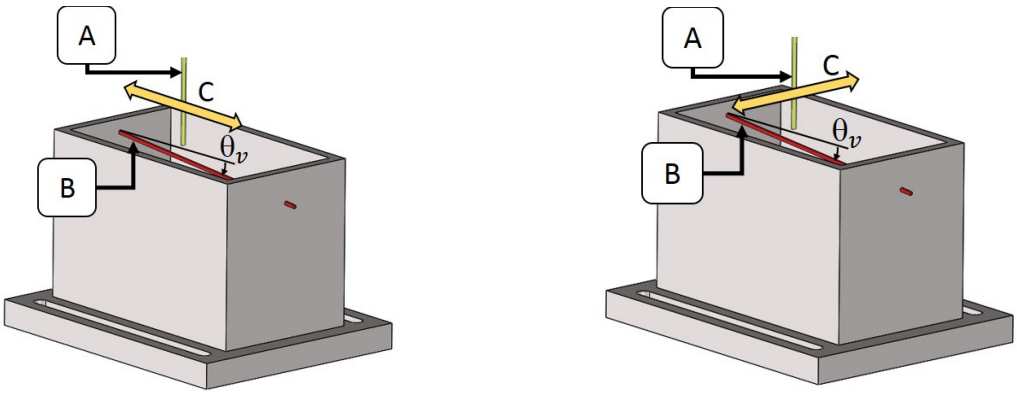


**(a)** **(b)**

**Figure 4.4:** Schematic diagram of the characterization procedure for: a) depth detection range, b) off-axis detection range. A: LDF probe, B: blood vessel phantom, C:direction of movement, $\theta_v$: the angle of the vessel phantom

During the experiments, milk flow velocities were achieved using a syringe pump (Graseby 3200, Graseby Medical Ltd., UK). The depth detection range was measured for three different flow velocities, 1 mm/s, 5 mm/s, and 10 mm/s, with 0.30 mm depth increments, starting from 0.30 mm tube depth. Lateral measurements were only performed for 5 mm/s flow velocity, which represents the maximum flow velocity described in (Liang et al. 2013), with 0.10 mm resolution

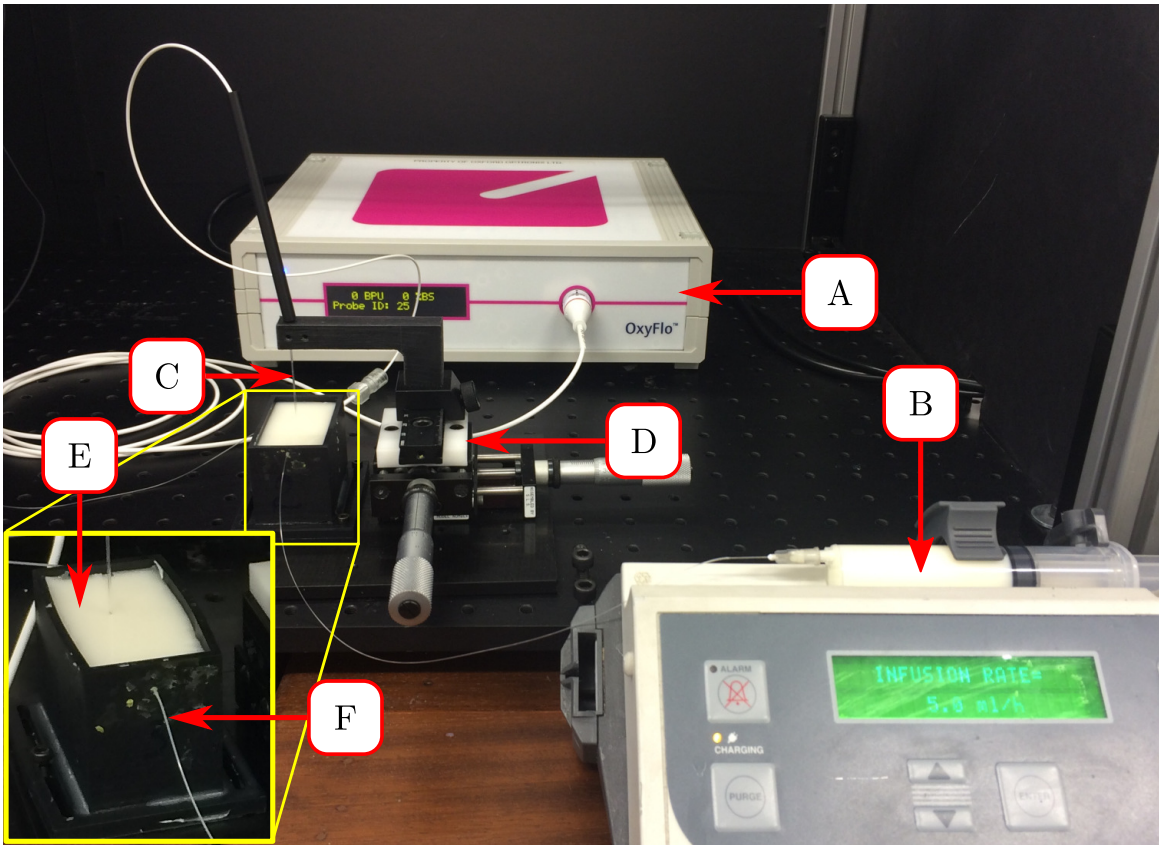


**Figure 4.5:** Experimental configuration for laser Doppler characterization of vessel flow in a brain phantom, using a commercially available laser Doppler system (OxyFlo$^{TM}$, Oxford Optronix, Abingdon, UK). A: LDF system, B: perfusion pump, C: LDF probe, D: linear stage, E: brain phantom, F: vessel phantom

and at four different tube depths (0.30, 0.90, 1.50, and 2.10 mm). In order to calibrate the zero depth position, the sensor was moved along the gelatine surface (right to left, Figure 4.4a) until it touched the tube. Since the tube was placed manually in the gelatine box, the computed uncertainty in finding the zero depth position was estimated as ± 0.10 mm. In each position, the Doppler signal was measured a minimum of 5 times and the average was taken.

### 4.2.2 Characterisation Results

Figure 4.6 shows the perfusion value for different flow velocities at various depths. Figure 4.7 shows the off-axis perfusion value for a flow velocity of 5 mm/s at found depth positions when measured across the capillary tube. The background signal of the LDF system was measured when there was no flow in the capillary tube and was found to fluctuate (mean: 13.7 AU, standard deviation: 29.4 AU). The threshold for vessel detection was empirically set at 120 AU

since, starting from this vaule, the perfusion level showed a statistically significant difference for all depths, when compared to the lowest measurement value at 2.00 mm off-axis position. Using this threshold, the maximum detection depth for a 5 mm/s flow velocity was found to be 2.10 mm. Using the same setup, measurement thresholds for 1.20, 1.00, 0.50, and 0.30 mm off-axis positions of the Doppler probe were found to be 0.30, 0.90, 1.50, and 2.10 mm depth, respectively. For the same position, 10 mm/s flow velocity gives a higher perfusion value compared to 5 mm/s. Consequently, the maximum detection depth also increases to 2.70 mm. A lower, 1 mm/s flow velocity also gives a lower perfusion value, with maximum detection depth of only 0.90 mm. Comparing these characterisation results to the characteristics of our needle (Figure 4.2), the minimum detection range of 0.67 mm at 0.88 mm off-axis distance for blood detections is fulfilled for flow velocities above 5 mm/s.

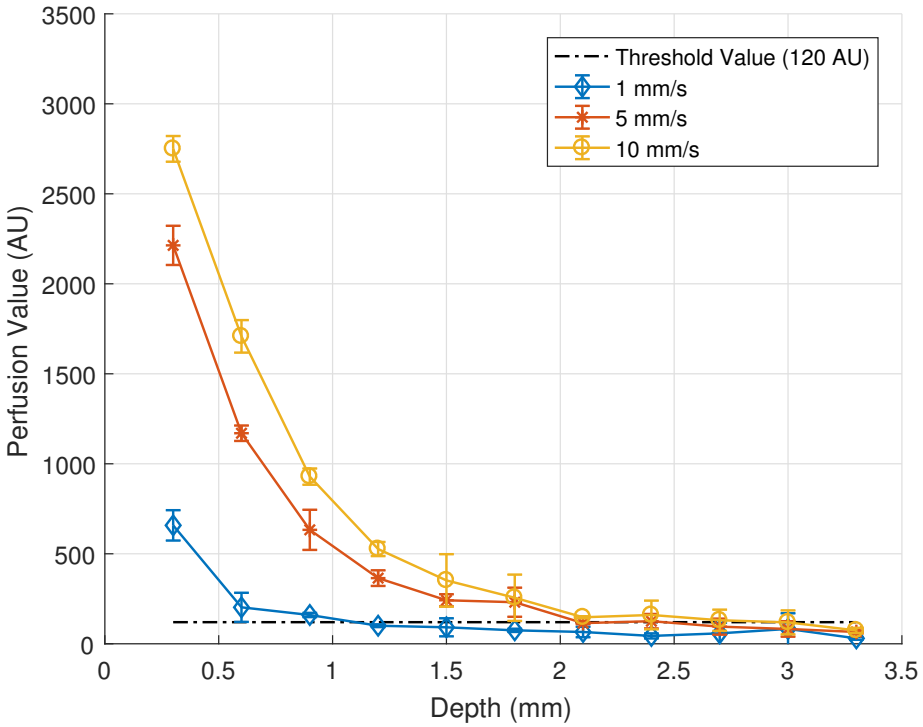


**Figure 4.6:** Mean and standard deviations of perfusion value against capillary depth for three different flow velocities, the dash-dot line is the threshold value

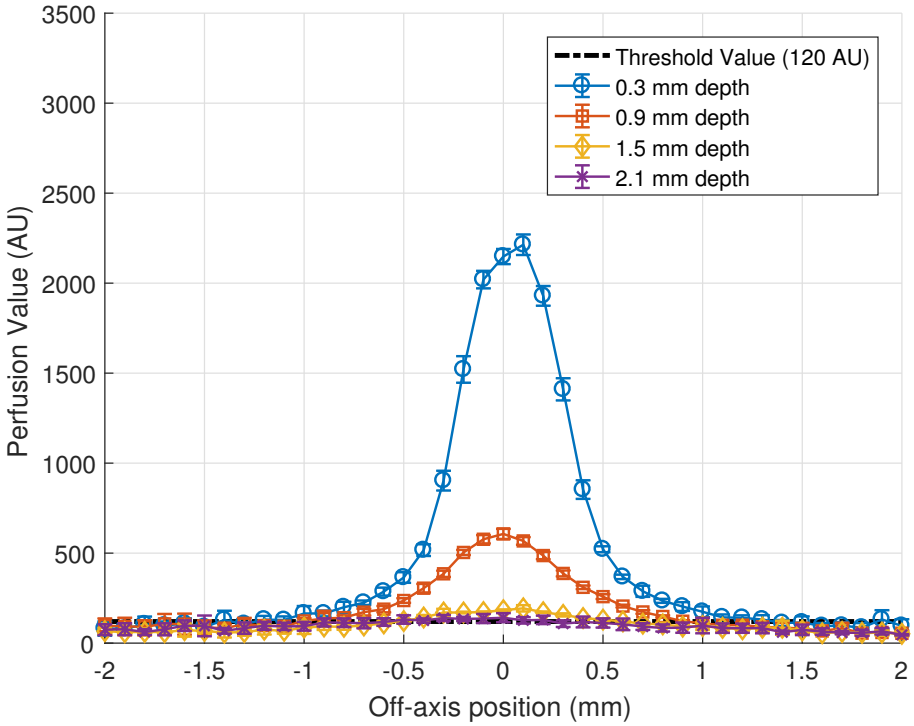


**Figure 4.7:** Mean and standard deviations for off-axis perfusion value when measured laterally across the capillary at different depths, the dash-dot line is the threshold value

## 4.3 Vessel position and orientation prediction - Feasibility Study

In this section, a new method to predict the position and orientation of a possible vessel in front of the needle is proposed. The detection algorithm is based on the characterisation results for 5 mm/s flow velocity (Section 4.2). These characterisation results show that, for a given perfusion value, the exact position and orientation of a vessel cannot be determined using a single measurement, since positions that give the same perfusion value are not unique. Successive measurements, combined with measurements from multiple optical probes made possible due to the PBN's multi-segment design, were used to infer the tube position and orientation. For the algorithm developed here, the assumption is made that the vessel detected by the probe is just one and that it is lying approximately in a plane normal to the needle axis. The implications of this assumptions are explored in Section 5.10, while Chapter 6 proposes a machine learning based technique to release this constraint.

### 4.3.1 Materials and Methods

#### Insertion Experiments using Two LDF Probes

The same tissue and blood vessel phantom was used as for the characterisation experiments (Section 4.2). A tube was placed inside a gelatine box on a gradient (Figure 4.8a). Two laser Doppler probes were placed in the PBN prototype, as shown in Figure 4.8b. The needle, embedded with the probes, was then placed in a two DOF linear stage. To investigate the ability of the probes to discriminate vessel pose, measurements were taken for several tip off-axis positions (defined with respect to the needle coordinate system $(x_n, y_n, z_n)$ in which the axis of the vessel intersects with $x_n$). By moving the PBN in the $y$ direction, a variable tip off-axis distance could be created. Perfusion values from both of the probes were measured in five different tip of-axis positions: -0.35, -0.18, 0.00, 0.18, and 0.35 mm. At each tip off-axis position, the needle was advanced in the positive $z$ direction at 0.50 mm increments, as in Wårdell et al. (2016), since it is the minimum resolution needed to be able to detect local changes in microvascular measurements, starting 3.00 mm away from the tangent plane of the vessel in the $xy$-plane. This starting position was set as $z = 0$. During all insertions, the flow velocity was maintained at 5 mm/s. For every depth increment, the needle was kept in place and the Doppler signal was measured during that time, alternating between the two probes (5 s for each probe) due to the inability of the detection system chosen here to look at both simultaneously. Ten repetitions were performed for each tip off-axis position. The experimental set-up for predicting the tube position and orientation is shown in Figure 4.9. Parameters of the experiments are shown in Table 4.1.

**Table 4.1:** Paremeters of the insertion experiments

| No | Angle (°) | Tip Off-axis (mm) | $z$ position (mm) | Repetition |
|---|---|---|---|---|
| 1 | 2 | -0.36 | 3.00 | 10 |
| 2 | 2 | -0.18 | 3.00 | 10 |
| 3 | 2 | 0 | 3.00 | 10 |
| 4 | 2 | 0.18 | 3.00 | 10 |
| 5 | 2 | 0.36 | 3.00 | 10 |

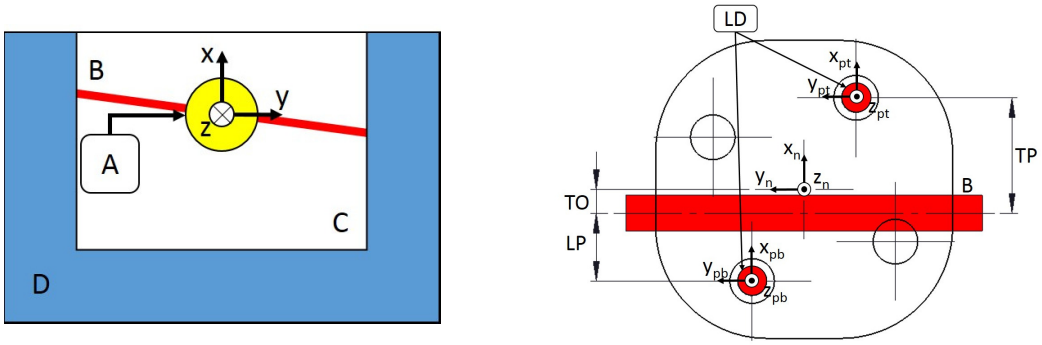


**(a)** **(b)**

**Figure 4.8:** (a) A schematic diagram of vessel detection experiments with a global coordinate system. (b) The position of two laser Doppler probes in the PBN with the definitions and terminology used for predicting the vessel; three local coordinates at the tip of the needle ($x_n$, $y_n$, $z_n$), the bottom probe ($x_{pb}$, $y_{pb}$, $z_{pb}$), and the top probe ($x_{pt}$, $y_{pt}$, $z_{pt}$) were used. A: The PBN, B: vessel phantom, C:tissue phantom, D: Gelatin box, LD: laser Doppler probe, TO: tip off-axis distance, TP: top probe off-axis distance, LP: bottom probe off-axis distance

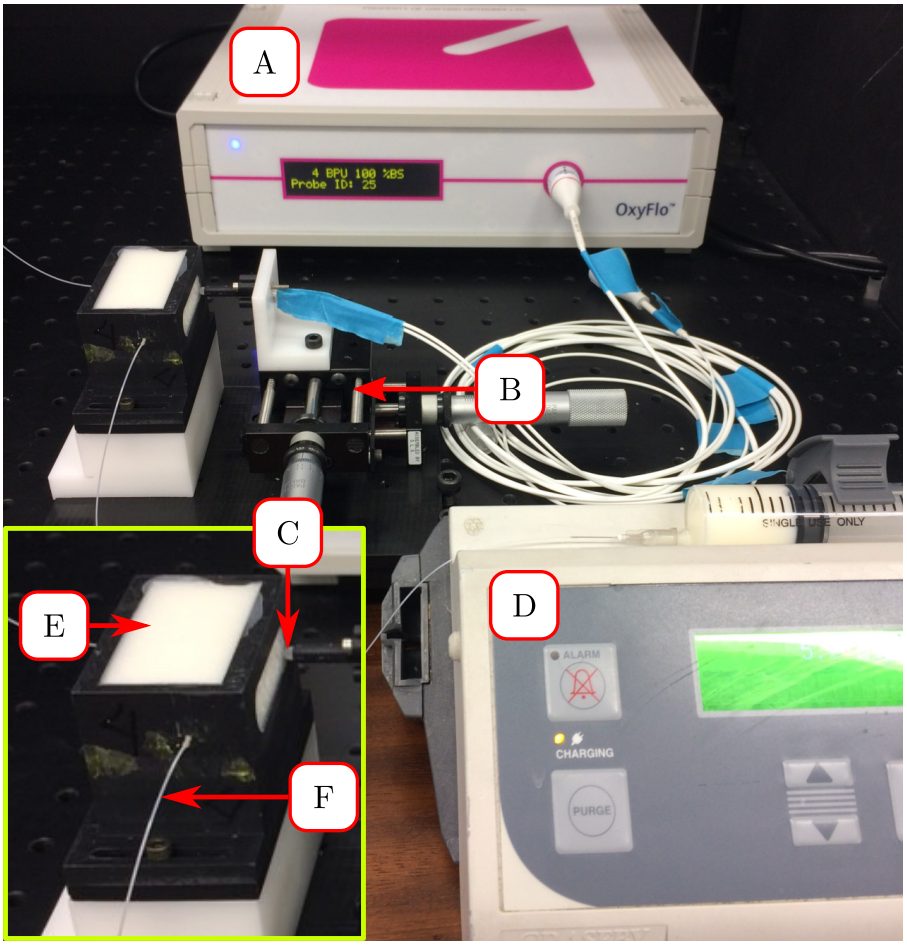


**Figure 4.9:** Insertion configuration for vessel prediction experiments, the LDF system used here was the same single channel LDF system as in Section 4.2. A: LDF system, B: linear stage, C: the PBN, D: syringe pump, E: brain phantom, F: vessel phantom

**Algorithm Development for Vessel Position and Orientation Prediction**

To develop the algorithm for predicting the vessel position and orientation (i.e. the pose), the characterisation results from Section 4.2.2 were approximated using a two dimensional function. To find the best approximation, off-axis and depth measurements were analysed individually before being combined into a single expression. The steps to find the approximating function were as follows:

- The depth perfusion value is approximated using an exponential function since the probability of a transmitted photon is also an exponential function (Wang et al. 1995).
- The off-axis perfusion value for each depth is approximated by a bell shaped function with the Gaussian $f_{zi}(y) = a_0 \mathrm{e}^{(-y^2/a_1^2)}$, where $a_1$ is a variable used to account for off-axis perfusion values at different depths.

The complete behaviour was thus approximated as:

$$f(y_p, z_p) = (c_1 \mathrm{e}^{(-y_p^2/(c_2 \mathrm{e}^{(c_3 z_p)})^2)} + c_4)\mathrm{e}^{c_5 z_p} + b \tag{4.1}$$

where $b$ is background noise, $y_p$ is the off-axis distance from the laser Doppler probe to the vessel, and $z_p$ is the off-axis distance from the laser Doppler probe to the vessel, and $z_p$ is the depth of the laser Doppler probe from the vessel. Constants $c_1 - c_5$ were found empirically using the MATLAB (The Mathworks inc., USA) curve fitting toolbox. Table 4.2 shows the parameter values of $c_1 - c_5$ and $b$. The two-dimensional (2D) map of perfusion values obtained from 4.1 is shown in Figure 4.10. LDF perfusion values for a given depth and off-axis position can be obtained from 4.1. However, during the insertion process, the depth ($z_p$) and the off-axis ($y_p$) position from the probe must be inferred from the measured signals using the inverse of 4.1. A lookup table of 4.1 facilitates its conversion into a grid used for mapping the insertion environment and provides the additional benefit of overcoming difficulties associated with an analytical inverse function, as the off-axis position, $y_p$ approaches zero.

Unlike a standard laser range finder that gives a measured distance directly, the LDF sensor

**Table 4.2:** Parameters used in equation 4.1

| $c_1$ | $c_2$ | $c_3$ | $c_4$ | $c_5$ | $b$ |
|---|---|---|---|---|---|
| 4.698 | -0.296 | 0.167 | 0.639 | -2.197 | 0.068 |

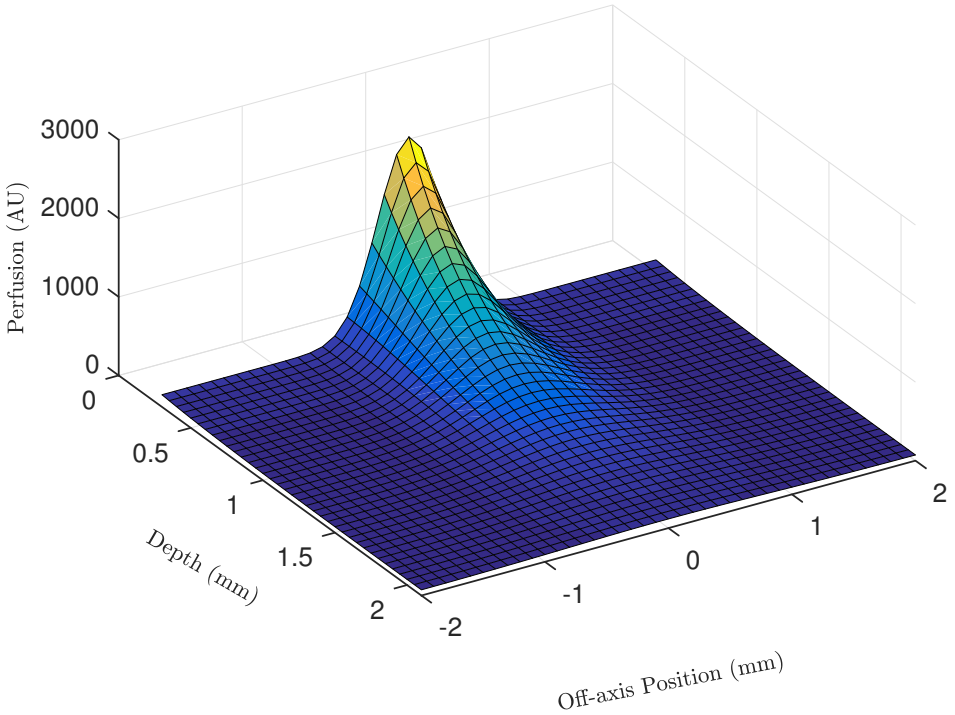


**Figure 4.10:** 2D map of the perfusion value generated using (4.1)

does not provide a unique vessel position. Even in the case of same vessel properties, there are multiple depths and off-axis positions that results in the same perfusion value. This is illustrated using the contour plot shown in Figure 4.11. To tackle this ambiguity, the recorded contour lines from each probe were transformed into global coordinates while the needle was advancing. A rigid glass tube was used as the blood vessel phantom, so an assumption could be made that the vessel in front of the needle would not move while the needle advanced towards it. Using this assumption, unique solutions were found at the intersection of two isolines in the global coordinate of two incremental measurements. The contour lines show that there is a possibility of four intersection points (a pair at each of the two different $z$ positions). In order to reduce the solution to a pair at the same $z$ position, a minimum of three consecutive measurements is therefore required.

It should be noted that, up to this point, we assumed the vessel to be a line that lies on a plane

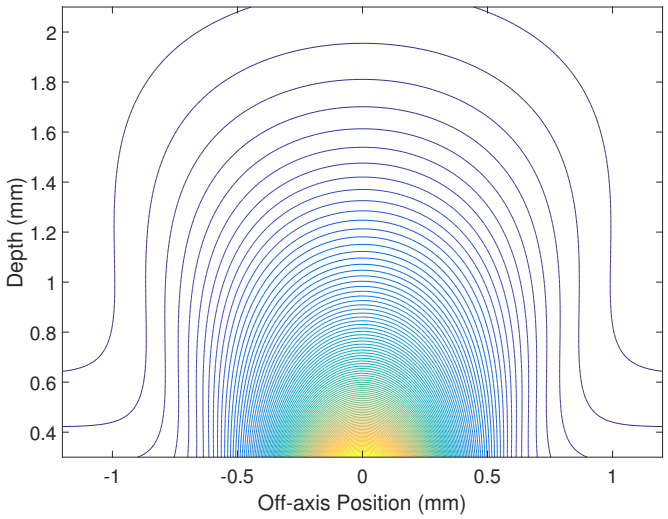


**Figure 4.11:** Contour plot of the LDF perfusion value measurements, each line showing depth and off-axis positions for the same perfusion value

parallel to the $xy$-plane perpendicular to the insertion axis of the needle (see Figure 4.8a). The location of this plane was at the $z$ position where the three contour lines intersect. To convert the 2D map into three dimensions, the probe measurements was assumed to possess rotational symmetry about the probe $z_p$ axis ($z_{pt}$ for the top probe and $z_{pb}$ for the bottom probe) and normal to the vessel's assumed plane. This means that, in the vessel plane, the possible probe off-axis distance ($y_p$) is rotated, generating a detection circle. The vessel position and orientation is then the tangent line of this detection circle, for which there are infinite solutions. To reduce the number of possibilities, measurements using the second embedded probe are used, as these measurements provide another detection circle. The vessel is then determined as coinciding with the tangent line to both of the circles, reducing the number of possibilities to four by solving the following equations simultaneously (Weisstein 2002*a*):

$$(\mathbf{t}_{bp} - \mathbf{x}_{bp}) \cdot (\mathbf{t}_{bp} - \mathbf{t}_{tp}) = 0 \tag{4.2}$$

$$(\mathbf{t}_{tp} - \mathbf{x}_{tp}) \cdot (\mathbf{t}_{bp} - \mathbf{t}_{tp}) = 0 \tag{4.3}$$

$$| \mathbf{t}_{tp} - \mathbf{x}_{tp} |^2 = \mathbf{TP}^2 \tag{4.4}$$

$$| \mathbf{t}_{bp} - \mathbf{x}_{bp} |^2 = \mathbf{LP}^2 \tag{4.5}$$

where $\mathbf{t}_{tp}$ and $\mathbf{t}_{bp}$ were the points of tangency to the two circles. $\mathbf{x}_{tp}$ and $\mathbf{x}_{bp}$ were the centre of the detection circle with radii of **TP** and **LP** from the top and bottom probe, respectively.

### 4.3.2 Vessel Pose Prediction Results

Figure 4.12 shows the mean and standard deviation of perfusion values for ten insertion experiments, using two laser Doppler probes, at five different tip off-axis positions. It shows that the position of the tube affects the perfusion value from each laser Doppler probe. At 0 mm tip off-axis position, there is no significant difference in perfusion values between the tow probes for all distances to the vessel. However, for the remaining tip off-axis position, statistically significant differences in perfusion values ($t$-test, $p = 0.01$) are observed, starting from vessel positions which are 1.50 mm (Figure 4.12a and 4.12b) and 1.00 mm (Figure 4.12d and 4.12e) away from the tip of the needle.

The algorithm to predict vessel pose was used to analyse the data for each insertion. An example of how this algorithm works is shown in Figure 4.13, using the mean value measurements of the bottom probe at 0 mm tip off-axis position. A significant perfusion value (>120 AU) was detected at point A in Figure 4.13a that gives a corresponding contour line of possible vessel positions in the $xz$-plane in global coordinates, as shown in Figure 4.13b. At the next increment (point B) another contour line was recorded (Figure 4.13c). Even though, in this case, there already were a pair of intersections points at the same $z$ position, another measurement at point C was still required to account for the worst case scenario, where three successive measurements are required. After recording the perfusion values at Point C, the third set of contour lines were recorded an the $z$ position of the vessel plane ($z = 3.10$ mm) and the radius of the detection circle (**LP** = 0.70 mm) of the bottom probe were determined (Figure 4.13d). Repeating this method for the top probe then gave two detection circles. The possible number of vessel poses was then reduced to four, shown by dash-dot lines in Figure 4.14.

To investigate the performance of the algorithm, every insertion was analysed. The characterisation results (Section 4.2.2) show that, for a given depth and off-axis position, there is a variability in the LDF perfusion value. Therefore, in order to look for the corresponding contour

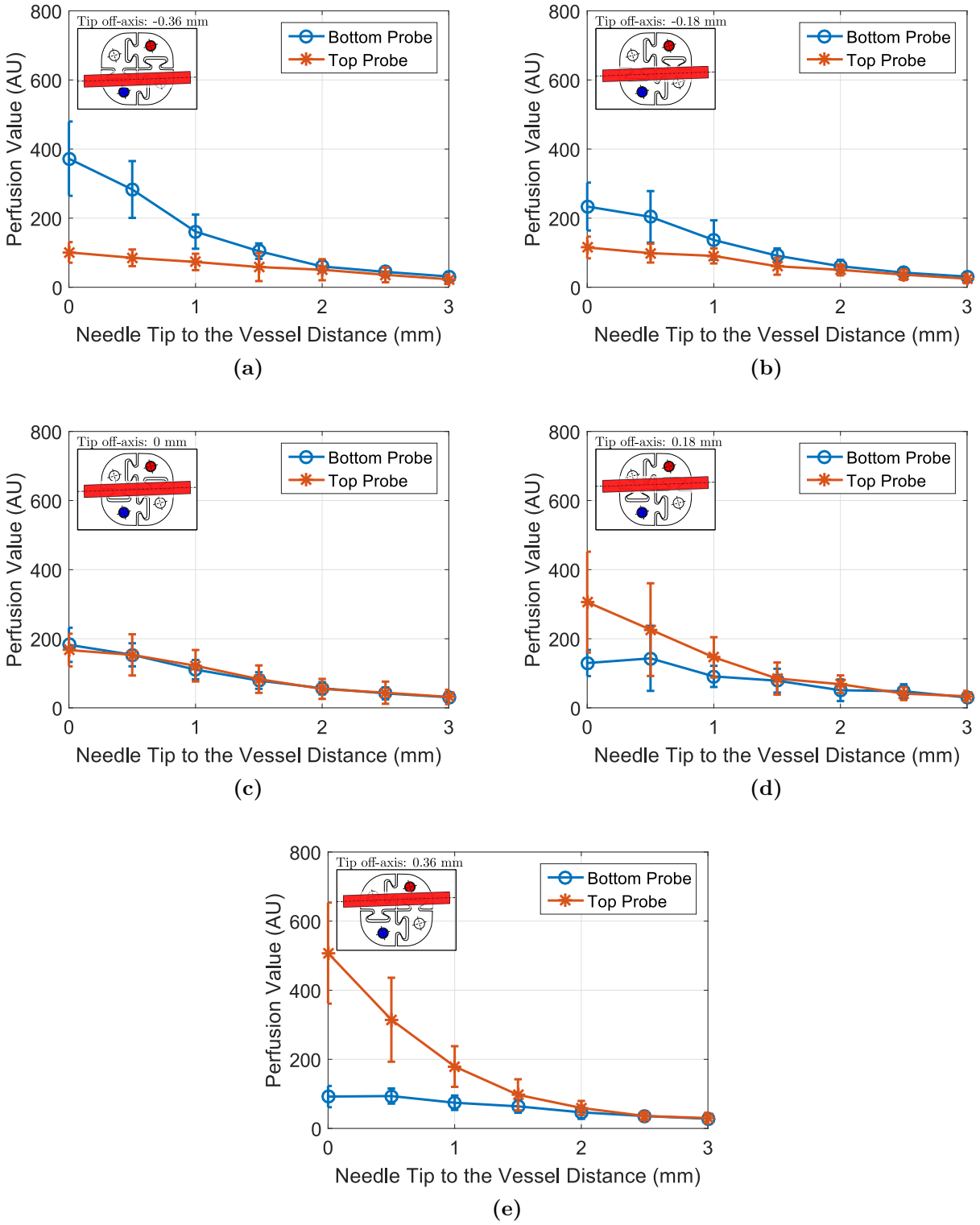


**Figure 4.12:** Mean and standard deviation of perfusion values for the top (asterisk) and bottom probes (circle), from 3.00 mm away from the surface of the needle, with 0.50 mm increments at a) -0.36 mm, b) -0.18 mm, c) 0.00 mm, d) 0.18 mm, and e) 0.36 mm tip off-axis position. The inset in each figure shows the position of the vessel. The red circle in the inset represents the top probe, and the blue circle represents the bottom probe. The experiment set-up is shown in Figure 4.9

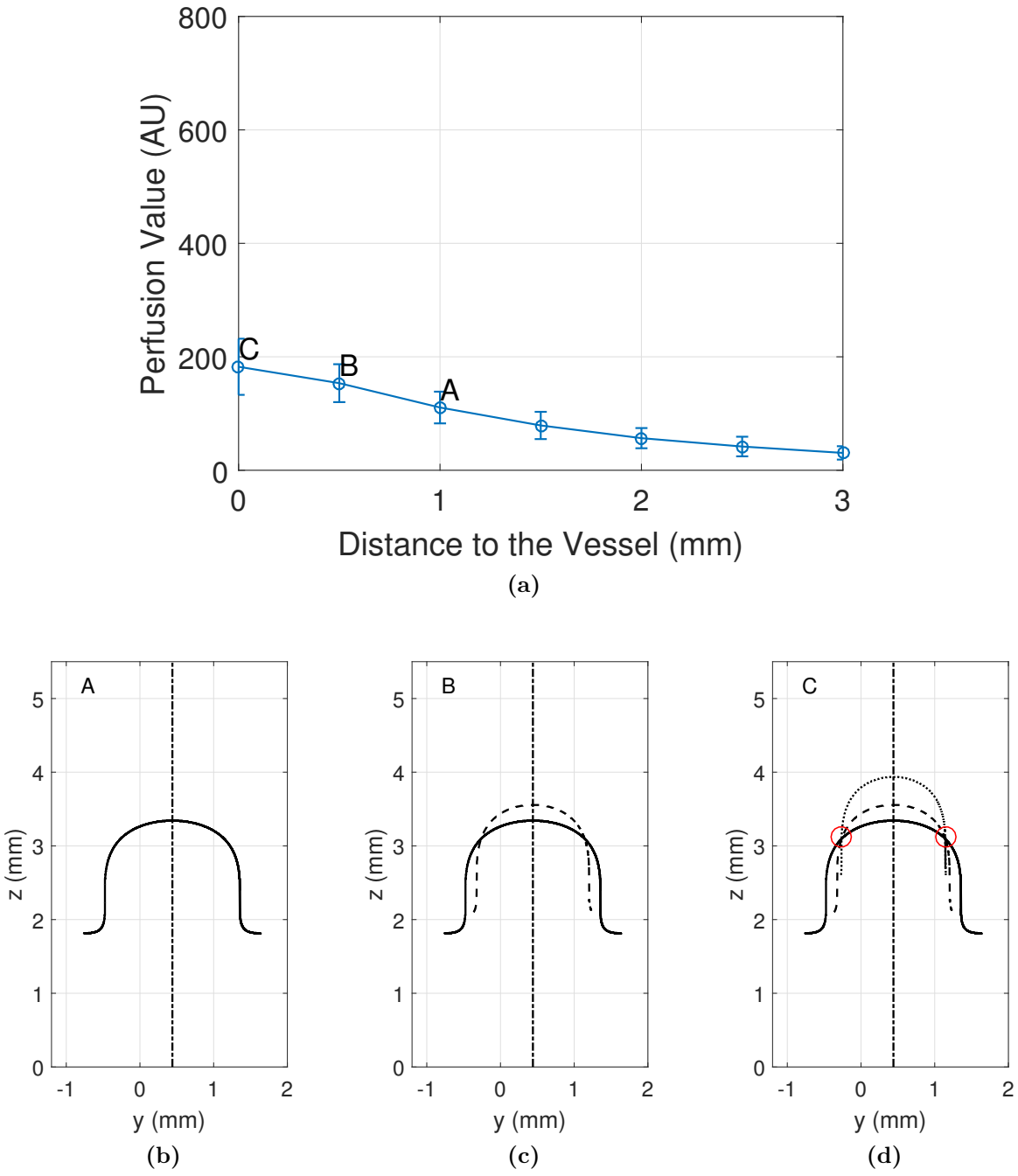


**Figure 4.13:** a) The mean perfusion value from the bottom probe (Figure 4.12c). The possible vessel position at point A, B, and C is shown in b), c), and d) respectively, the dash-dot line is the insertion axis of the laser Doppler probe. The circles in d) show the possible vessel positions after three successive measurements

line, the recorded value was included with ± one standard deviation, as measured during the characterisation process. The $z$ position of the vessel plane and radius of the detection circle in global coordinates were then determined by computing the centroid of the intersection area.

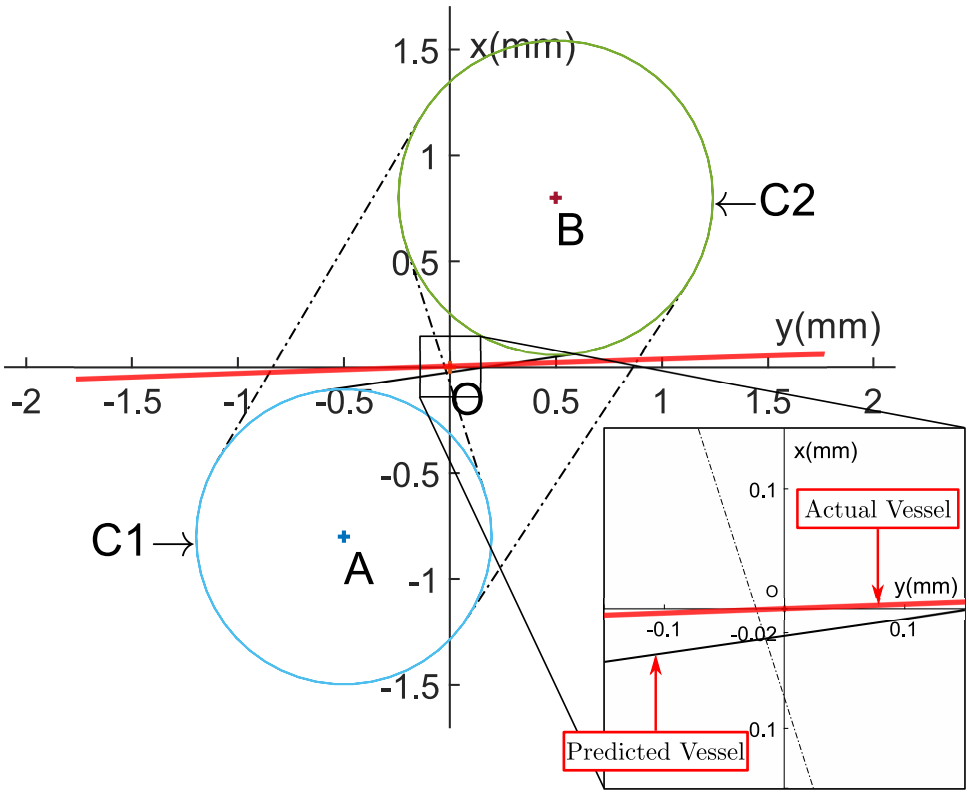


**Figure 4.14:** Four possible tube position and orientation reconstructions (three dash-dot lines and one solid line) located on the plane perpendicular to the insertion axis (parallel to the $xy$-plane) using two detection circle methods. The solid line is the most parallel line to the ground truth that is used to quantify the vessel reconstruction. Inset shows the intersection of the line at $x$ = -0.02. O: tip of the PBN, A: position of the bottom probe, B: position of the top probe, C1: the detection circle of the bottom probe, C2: the detection circle of the top probe

To quantify how good the tube reconstruction is, a comparison to the ground truth (Table 4.1) was conducted. Three parameters were compared:

- The $z$ position of the detected vessel
- The angle between the vessel and the tangent line between the two detection circles that lies closest to it, where the angle of the vessel was set experimentally to 2° for all trials
- The $x_n$ intersection of the tangent line of the two detection circles that lies closest to the vessel (inset in Figure 4.14 (in this case, $x_n$ and $y_n$ align with $x$ and $y$ of the global coordinate)), which should equal to the real tip-off axis position of the vessel with respect to the needle tip.

Using the parameters above, the mean of the recorded depth position is 3.00 mm, with 0.35

mm standard deviation and 0.37 mm RMS error. The RMS error for the tip off-axis prediction is 0.36 mm. The angle prediction has an average of 5.8°, with 15.1° standard deviation and 15.6° RMS error. Tabulated data for these results is shown in Table 4.3.

**Table 4.3:** Mean, standard deviation, and RMS error of the constructed vessel

| Parameter | Angle (°) | Tip Off-axis (mm) | $z$ position (mm) |
|---|---|---|---|
| Average | 5.8 | - | 3.00 |
| Standard Deviation | 15.1 | - | 0.35 |
| RMS Error | 15.6 | 0.36 | 0.37 |

## 4.4 Discussion

The characterisation results illustrate the detection range of the 800 nm wavelength LDF probe. Using 5 mm/s flow velocity in a tube with an inner diameter of 0.6 mm fulfils the minimum requirement to detect the vessel in front of the tip of 2.5 mm outer diameter PBN prototype, as it was shown to cater for up to 1 mm off-axis detection at 0.9 mm depth (Figure 4.2). One of the advantages of LDF is that it has a fast response time (Rajan et al. 2009). During insertion, an increase in the perfusion value means that the tip is approaching a vessel. If a high perfusion value is detected, the insertion can be stopped and, based on the vessel pose estimate, an avoidance strategy that complies with the needle's geometrical and steering constraints can be implemented. Using the sensors, needle insertion can be performed in a safer manner, allowing even vessels that may not have been visible in preoperative images, to be avoided. Indeed, the sensors can detect vessels with a diameter as small as 0.6 mm, which may be hard to image using MRI, due to the limited resolution of the reconstructed volume (typically 0.59 x 0.59 x 1.50 mm, as in (Bériault et al. 2014). Additionally, compared to MRI guided procedures, in which the patient has to be moved in and out of the scanner (Sillay et al. 2014), the method and approach described in this chapter should reduce surgical time without compromising patient safety.

The measurement value of the laser Doppler system is affected by both the concentration of

the scattering particles and the flow velocity. Figure 4.6 shows that a vessel with higher flow velocity can be detected further ahead compared to a lower velocity. Therefore, a vessel with lower flow velocity may not be detected before it is too close to the tip of the needle to initiate an avoidance procedure. Nonetheless, the 5 mm/s flow velocity is half the value of the average blood flow velocity in a small vein (10 mm/s) and a quarter of the blood flow velocity in an arteriole (20 mm/s) (Fredriksson 2009). It is therefore reasonable to believe that the system will work at least as well for more realistic physiological flow velocities. However, the size of the vessel also needs to be considered. In smaller vessels, the lower blood concentration inside it would reduce the perfusion value. Therefore, before surgical implementation, a minimum value of perfusion for vessels that must be avoided during surgery should be defined.

In this chapter, two laser Doppler probes have been used to determine a safe region for the steerable needle to access in order to avoid a vessel sensed along its insertion path. The work in this chapter was focused on a 5 mm/s flow velocity inside a 0.6 mm inner diameter tube to prove the concept of LDF-based vessel detection. Due to a dependency on depth and flow velocity, it is not possible to determine the exact position of blood vessels with respect to the needle using a single measurement. Using two diagonally positioned laser Doppler probes in opposite PBN working channels shows the discrepancy between the perfusion values as a function of the distances between the vessel phantom and the probes. In Figure 4.12c, where the tip off-axis was set at 0 mm, there is no significant difference between the perfusion values from the top and bottom probes, since the distance from the vessel phantom to each probe is equal. For other tip off-axis positions, significant differences are observed, starting at the maximum detection range of 2.1 mm away from the sensor. In a two dimensional world, where a tube/vessel has zero gradient with respect to the normal plane to the needle, the problem of vessel avoidance becomes on of moving on the plane, and thus the vessel can be identified and avoided. However, the vessel angle is in the range of $0^\circ \pm 180^\circ$ to the needle's normal plane, and thus further data processing is required.

Successive measurements using at least three data points have been used to determine the distance from the tip of the needle to the tube surface and the possible tip off-axis position. Successive measurements rely on the accuracy of the inverse of (4.1). Equation 4.1 was derived

empirically, since understanding the random scattering inside a medium like brain tissue is commonly achieved using simulation results based on random walks (Fredriksson et al. 2009, Hennessy et al. 2014). In this paper, (4.1) was only used to smoothen the characterisation data.

Using two probes, the distance from the tip to the needle is determined by the mean of the distance from the top and the bottom probes. The average distance prediction from the probe to the surface of the tube gives sub-millimetre accuracy, with an RMS error of 0.37 mm. However, the RMS error of the angle measurement is 15.6°. The effect of the tip geometry has not been considered in the prediction algorithm presented here, and this may be the main source of this rotational inaccuracy. However, for the steerable needle, in order to avoid an obstacle (e.g. a vessel), the avoidance direction can be set at 90° to the direction of the vessel axis. If this avoidance direction is used, it is still safe to avoid the vessel, even with the angular RMS error measured here. The algorithm outputs four possible poses for the vessel, and thus the needle "escape" direction should be set as the one which would result in the smallest risk to puncture any of these. As this method is believed to be the first method to employ embedded optical fibres to predict vessel pose, no comparison in terms of accuracy of the system can be made with the existing literature. In Chapter 5 and 6 four LDF probes were used, since this eliminate any possible ambiguity of possible vessel configurations.

It should be noted that the detection range of the sensor is only 2.1 mm from the needle tip. The detection range can be increased by using a sensor with a longer wavelength (currently the system uses an 800 nm laser). However, using an optical system, the longest detection range that is found in the literature is 3 - 4 mm (Liang et al. 2013). This is less than the minimum radius of curvature of our latest PBN design (a detection depth of 15 mm is needed for a needle with 70 mm radius of curvature, assuming the vessel to be avoided has a diameter of 1 mm, with 0 mm tip-off-axis position). Therefore, a short retraction, followed by reinsertion may be required to completely avoid the vessel, depending on its predicted orientation. Even though retraction is required, full extraction and reinsertion can be avoided, which would be the only option for rigid needle designs. The inverse data computed from the perfusion value of depth and off-axis positions used in this chapter is only valid for the given combination of vessel, medium properties and sensing configurations. Any change in the flow velocity rates, tube

diameter, optical properties of the tissue phantom, and the type of the sensor, may change the relationship of the empirical inverse function described here.

## 4.5 Conclusion

This chapter discussed a novel vessel detection method for steerable needle systems with multiple lumens. The specific proof-of-concept implementation described in this chapter employs two laser Doppler flowmetry probes connected to a single channel LDF monitor. Errors of 0.37 mm (RMS) in depth detection and 15.6° angular error for predicting the vessel pose were achieved, but with significant potential for improvement. Since it was shown that vessel direction can be predicted using multiple probes combined with successive measurements, finding a complete relationship for every parameter is possible. This investigation is discussed in Chapter 5. Chapter 5 also discusses the effect of probe movement inside the tissue on the perfusion reading, alongside an investigation performed with a four-channels LDF monitor that can measure the perfusion in all of the channels simultaneously.

# Chapter 5

# Multiple Forward Looking Sensors to Predict Vessel Pose

## 5.1 Introduction

Chapter 4 discussed the feasibility of using forward-looking sensors in a steerable needle, which have two main purposes: 1) to detect the presence of a vessel; 2) to determine the possible vessel pose if a vessel has been identified. More specifically in PBNs, having a sensor in each segment is crucial since the steering of the needle is performed by changing the leading segment/s. Therefore, by embedding a sensor in each segment, the presence of a vessel in front of any one of the four segments can be detected. As explained by Wårdell et al. (2016) and shown by our investigation in Chapter 4, the perfusion value threshold can be used to determine the presence of a vessel in the proximity of the sensor (i.e. 120 AU).

In Chapter 4 the perfusion characterisation was only performed in the static condition, while in this chapter, besides the static condition, a perfusion reading where the needle is moving was also investigated. An LDF system measures the Doppler shift effect of the light refracted by the scattering particles. Since the tissue is also a scattering particle, the LDF monitoring system also records the movement of the tissue, and this movement needs to be accounted for since the movement of a large number of scattering particles with slow movement could be

erroneously recorded as a high perfusion value (Öberg 1999).

The results in Chapter 4 also demonstrated that vessel pose (i.e. position and orientation) prediction can be achieved by using successive measurements combined with a look-up table of the inverse perfusion value obtained with two LDF probes. However, this method only works for a given pair of tissue and vessel properties. In this chapter, a novel detection strategy is proposed, based on the relative measurements of four probes embedded within a PBN prototype with a diameter of 4 mm (Figure 5.1). Using these relative measurements, vessel pose estimation can be achieved for any tissue optical properties and without reliance on the inverse function of the perfusion value. In addition, it is hypothesised that, if the needle is inserted using a constant insertion speed, the background perfusion value affecting vessel measurements would be constant. This assumption is exploited to suggest an approach where vessel presence can be discriminated from bulk tissue movement. The use of the 4 mm diameter PBN in this chapter is due to sensor size availability. The tip of the sensor has a length of 60 mm with a diameter of 0.3 mm. However, the rest of the sensor has a diameter of 0.6 mm, which does not fit in the working channel of the 2.5 mm diameter PBN, but it fits in the working channel of the 4 mm diameter PBN.

This chapter is presented in two parts. In Section 5.2, a four-channel commercial laser Doppler blood-flow monitoring system is characterised. The characterisation in this chapter is the complementary to the characterisation in Section 4.2 due to the use of two different systems. In Chapter 4, the LDF monitor uses 800 nm wavelength laser while the four-channel LDF used in this chapter uses 785 nm laser. The characterisation includes static measurements, where the perfusion value is measured for different vessel sizes and tissue properties, and dynamic measurements, where the perfusion value is obtained while the PBN is moving forward with constant insertion speed. In Section 5.3, an algorithm based on the relative measurements between sensors is presented, which enables the vessel pose to be classified with a known degree of uncertainty. Section 5.4 discusses these results, while the summary of the main findings is included in Section 5.5. The contents presented in this chapter are reproduced with permission from the following publication:

- Vani Virdyawan, and Ferdinando Rodriguez y Baena, Vessel Pose Estimation for Obstacle Avoidance in Needle Steering Surgery using Multiple Forward Looking Sensors, in: 'Proceedings of the IEEE International Conference on Intelligent Robots and Systems (IROS)', Oct. 2018.

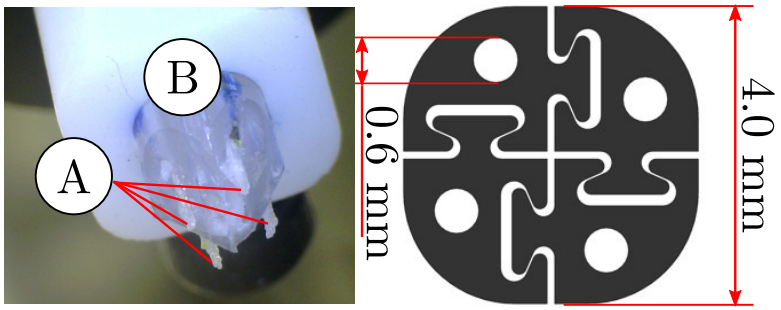


**Figure 5.1:** Left: scaled-up prototype of the PBN used here (B) and laser Doppler probes embedded within the needle (A). The needle has an outer diameter of 4.0 mm, with 4 working channels, each with a diameter of 0.6 mm (right)

## 5.2 A Four-Channel Laser Doppler Flowmetry Characterisation

### 5.2.1 Material and Methods

A commercially available, four-channel laser-Doppler tissue monitor (OxyFlo™ Pro XL (Oxford Optronix, Abingdon, UK)) with bare-fiber type probes (NX-BF/F (Oxford Optronix, Abingdon, UK)) was characterized. The laser has a wavelength of 785 nm, with a power $< 0.5$ mW at the probe tip. The probe diameter is 0.3 mm. Perfusion values were recorded using a LabJack U3-HV (LabJack Corporation, Colorado, USA) with a 150 Hz update rate.

Firstly, perfusion values for different flow velocities (5, 20, 40, 80 mm/s) and vessel phantom sizes (0.3 and 0.6 mm inner diameter) were measured to investigate the dynamic range of the equipment. A capillary tube with an inner diameter of 0.6 mm and an outer diameter of 0.9 mm was used as the vessel phantom. To change the inner diameter to 0.3 mm, a polyethylene tube was placed within the capillary tube. The vessel phantom was embedded at at a gradient

inside the same grey matter phantom as described in Chapter 4.2.1. To mimic the reduced scattering coefficient of blood (1.8 $mm^{-1}$), 3.5% fat milk diluted in water to obtain the 25% volume fraction was used as a blood surrogate (*Handbook of optical biomedical diagnostics* 2002). The same automatic syringe pump as explained in Chapter 4.2.1 was used to achieve the flow velocities. All measurements were performed with one Doppler probe perfectly aligned (i.e. 0.00 mm off-axis position) with the vessel, 0.30 mm away from the probe tip.

Secondly, perfusion values for grey matter phantom and white matter phantom were compared, where the white matter phantom was made by adding 15 g/L $TiO_2$ ($\mu_s' \approx 3.8$ $mm^{-1}$ and $\mu_a = 0.005$ $mm^{-1}$) into gelatine (Akarçay et al. 2012). The comparison was done for a 0.6 mm diameter vessel phantom at 20 mm/s flow velocity, with 0.00 mm off-axis position and the vessel placed at different depths from the probe tip (0.30 - 2.10 mm, with 0.30 mm increments) and at different off-axis positions (-2.00 - 2.00 mm, with 0.20 mm increments) and the depth fixed at 0.30 mm. The gelatine box was mounted on the top of a kinematic base (KB25/M, Thorlabs, New Jersey, USA), which could be assembled and disassembled with high repeatability (26.72 $\mu$rad) so that the position of the vessel phantom with respect to the probe could be calibrated only once, beforehand. The bottom of the kinematic base was mounted on a two degree-of-freedom (DOF) precision linear stage. Figure 5.2 shows the characterisation set-up for the four-channel LDF monitor. In order to calibrate the position of the vessel, the sensor was moved until it touched the vessel and the position was recorded. Based on the calibration of the whole set-up, repeatability of $\pm$ 0.10 mm was achieved in measuring the "zero position" of the vessel with respect to the probe.

The third set of experiments was conducted to investigate the effect of different constant insertion speeds on perfusion values. Four insertion speeds were tested: 0.2, 0.4, 0.6, 1.0 mm/s, all within the grey matter phantom. During insertion, the perfusion values were recorded and compared to the perfusion value obtained while the probe was stationary. On completion of this characterisation experiment, the feasibility of detecting the vessel located in front of the needle, as it travelled at 0.20 mm/s towards it, was investigated.

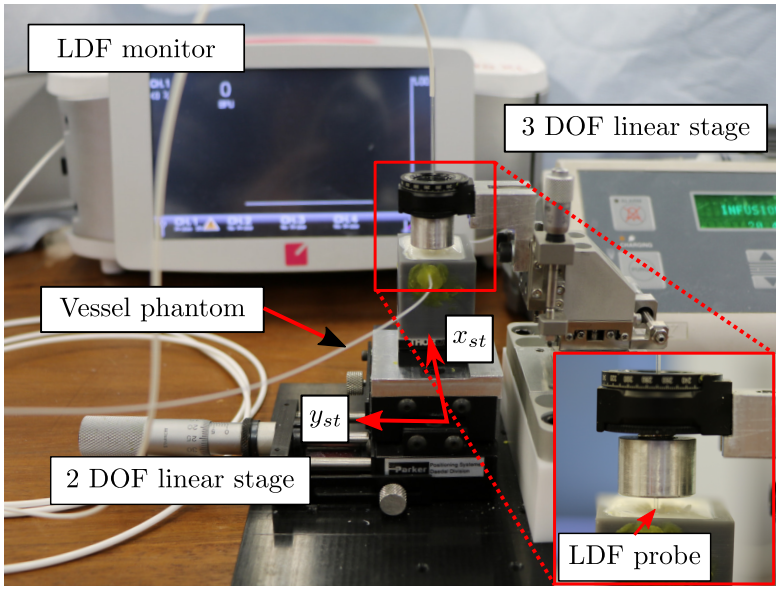


**Figure 5.2:** Experimental set-up used for LDF characterisation, the vessel and grey matter phantom were placed on top of a 2 DOF linear stage that can be moved in the $x_{st}$ and $y_{st}$ directions

### 5.2.2 Results

Since determining an absolute perfusion value is not possible, an LDF monitor measures relative perfusion value with an arbitrary unit (AU). If the concentration of moving particles is kept constant, the perfusion value of an LDF monitor increases linearly with the increase of flow velocity up to the dynamic limit of the instrument (Fredriksson et al. 2007). Figure 5.3a shows that the dynamic limit for the set-up is 20 mm/s for both vessel phantom. This flow velocity is equal to the flow velocity of an arteriole (Fredriksson 2009).

For a given flow velocity and vessel diameter, Figure 5.3b and 5.3c show that the higher the reduced scattering properties, the lower the perfusion value. At 0.30 mm axial depth and 0.00 mm off-axis position, for instance, the perfusion value in the grey matter phantom gives 5 times the perfusion value of the white matter phantom (1500 AU compared to 300 AU). Even though the perfusion value of the grey matter phantom is not always 5 times the perfusion value of the white matter phantom, results demonstrate that, in general, this value is always higher.

The stationary probe experiment in the absence of a vessel within the phantom produced a perfusion value of 20 AU. Conversely, as can be seen in Figure 5.4a, this perfusion value increases by 200 AU for 0.2 mm/s insertion speed and 400 AU for 0.4 mm/s insertion speed. A high spike

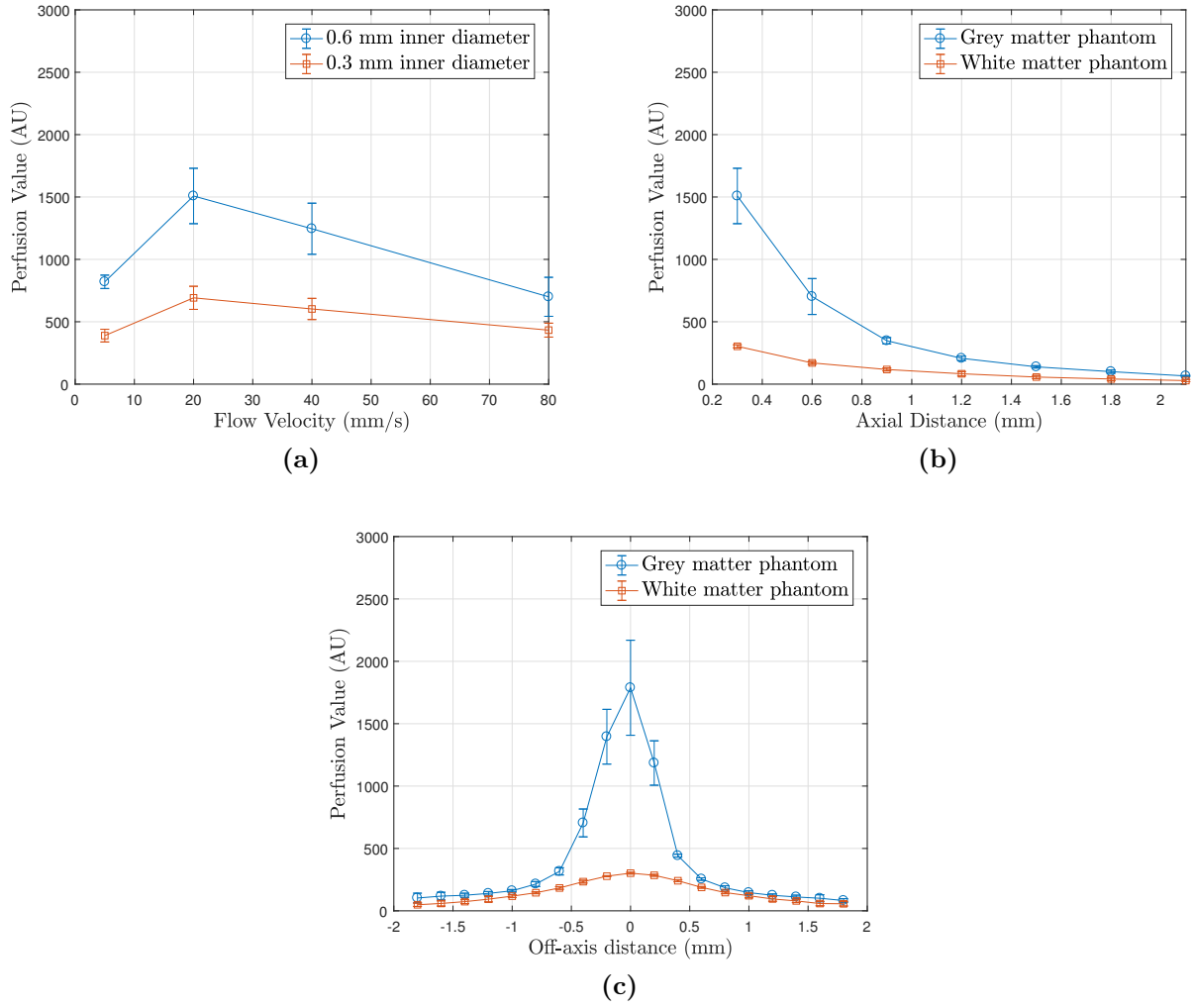


**Figure 5.3:** Characterization results: a) perfusion value for different flow velocities in a vessel with 0.6 mm and 0.3 mm inner diameter; b) perfusion value for 20 mm/s flow velocity in grey matter phantom and white matter phantom, with vessel placed at variable axial depths; c) perfusion value for 20 mm/s flow velocity in grey matter phantom and white matter phantom, with vessel placed at different off-axis distances

was always observed at the beginning of the insertion for all of the experiments. In Figure 5.4a there is another spike at 25 s. However, since it represents a sudden increase of perfusion value and is short in duration (0.6 s), we could safely assume that it was not due to an approaching vessel, and could thus discard it. Mean and standard deviation for 02, 0.4, 0.6, and 1.00 mm/s insertion speeds are shown in Figure 5.4b. Statistically significant differences are observed for all of these measurements (one-way ANOVA, F: 317.4, $p$: 0.0001 with Post-Hoc Tukey test). The virtually constant offset values identified can be fit linearly ($R^2 = 0.96$) with

$$B_O = 1382 \times v - 137.4 \tag{5.1}$$

where $B_O$ is the perfusion offset value and $v$ is the insertion speed. The feasibility of detecting a vessel using 0.2 mm/s insertion speed is shown in Figure 5.4c. Starting from 140 s, perfusion increased up to 956 AU. The insertion was then manually stopped. The perfusion value dropped to 780 AU, showing that there is a vessel in front of the probe. The perfusion value drop was $\approx$ 200 AU which, as expected, is equal to the perfusion value offset for 0.2 mm/s

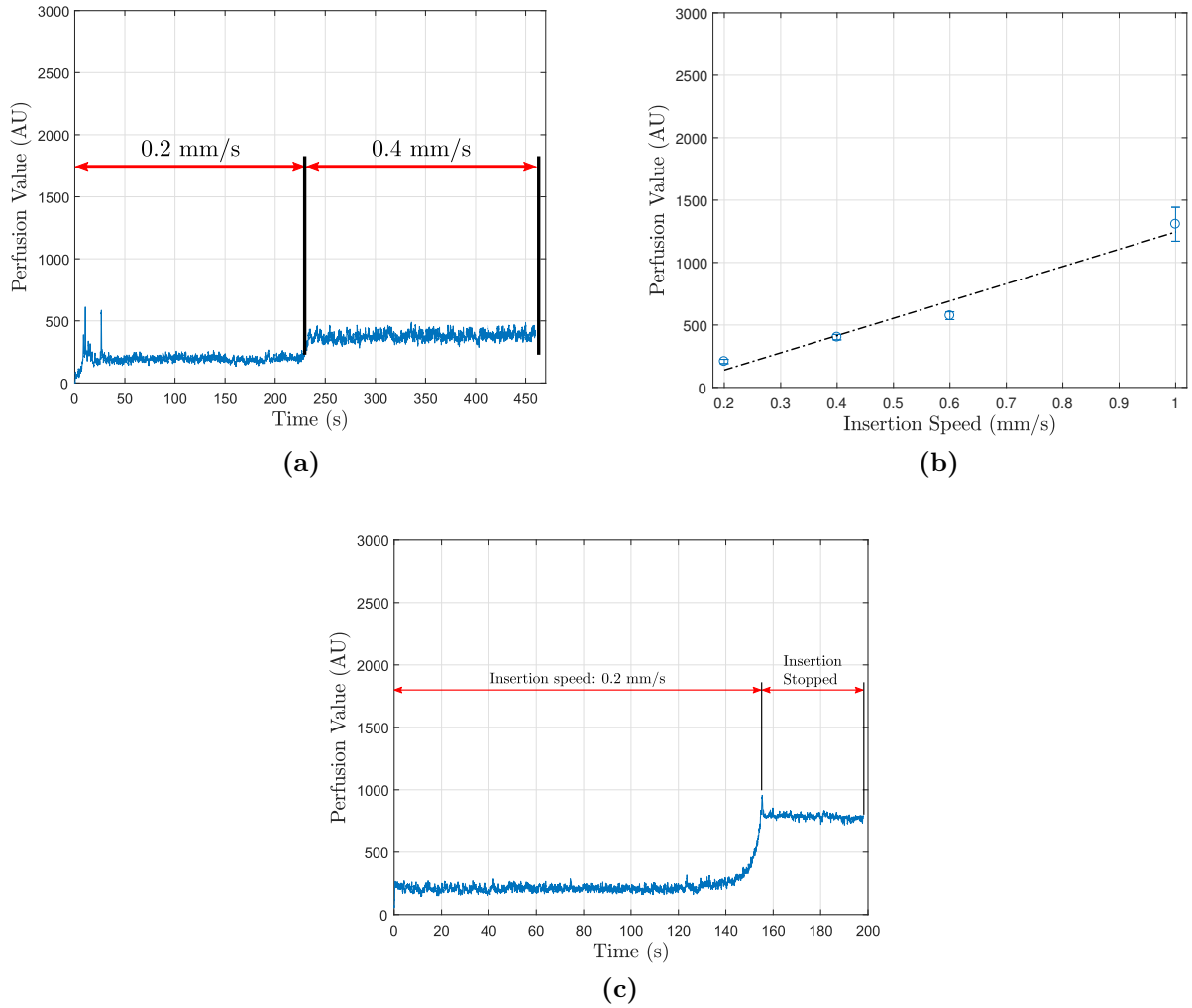


**Figure 5.4:** Characterization results: a) perfusion value for constant insertion speed of 0.2 mm/s and 0.4 mm/s; b) mean and standard deviation of perfusion values obtained for 0.2 mm/s, 0.4 mm/s, 0.6 mm/s, and 1.0 mm/s insertion speeds; c) constant insertion speed of 0.2 mm/s, with a vessel detected at time 155 s, at which point the insertion was stopped. The distance from the probe to the vessel was $\approx$ 2 mm. The perfusion value drop was $\approx$ 200 AU which, as expected, is equal to the perfusion value offset for 0.2 mm/s

## 5.3 Vessel Pose Classification

Due to the high variability in perfusion values as a function of tissue and vessel parameters, it would be near impossible to ascertain depth and off-axis position of a vessel for a given perfusion value, without prior knowledge of these parameters. In addition, using a single probe, it would be impossible to estimate the pose of a vessel lying in front of the tip of the needle. In this chapter, a laser Doppler probe was embedded in each of the four segments of a PBN. The vessel pose is determined By comparing the simultaneous measurements from all four laser Doppler probes.

### 5.3.1 Materials and Methods

The probes were embedded in the PBN working channels (Figure 5.1), at different $x - y$ positions but on the same orthogonal plane, when all the segments are aligned. The following assumptions were made:

1. only one vessel is ever in view,
2. the vessel is located on a plane which is approximately perpendicular to the insertion axis,
3. the portion of the vessel is straight inside the detection range of the sensors.

On this basis, the distance between the vessel and the laser Doppler probe can be described as in Figure 5.5a. The axis of the vessel is defined as:

$$ax + by + c = 0 \tag{5.2}$$

where $-\frac{c}{a}$ is the $x$-intercept of the line, and $-\frac{c}{b}$ is the $y$-intercept of the line. The distance from each probe to the axis of the vessel is

$$d_n = \mid ax_n + by_n + c \mid / \sqrt{a^2 + b^2} \tag{5.3}$$

Here, $n = 1, 2, 3, 4$, and $d_n$ is the distance of the vessel to the respective probe. Based on Figure 5.3c, the closer the off-axis distance of the vessel to the probe, the higher the perfusion value measured.

To classify the vessel pose, the measurement values were then sorted from highest to lowest: $P_{v1}, P_{v2}, P_{v3}, P_{v4}$, $P_{v1}$ being the highest and $P_{v4}$ the lowest perfusion values. $P_{v1}$ relates to the distance $d_{v1}$ between the vessel and the respective probe. Consequently, $d_{v1}$ is the shortest distance and $d_{v4}$ the longest. Since there were four probes, the total number of classes is equal to the number of permutations of the set $Pr = \{P_1, P_2, P_3, P_4\}$, which is $4! = 24$ classes. Boundaries of vessel pose classes are calculated by solving: $d_1 = d_2$, $d_1 = d_3$, $d_1 = d_4$, $d_2 = d_3$, and $d_3 = d_4$. The boundaries are then given by

$$a = -(b(y_n + y_m) + 2c)/(x_n + x_m) \tag{5.4}$$

and

$$a = -b(y_n - y_m)/(x_n - x_m) \tag{5.5}$$

with $n = 1, 2, 3, 4$, $m = 1, 2, 3, 4$, and $n \neq m$.

In the equation of a line, the gradient is $-\frac{a}{b} = \tan\theta$. By setting $b = 1$, class boundaries can be obtained for $-90° < \theta < 90°$. For $\theta = 90°$, the value of $\tan\theta$ approaches infinity, therefore the value of $b$ is set to 0 and $a$ is set to 1. Figure 5.5b shows the boundary between classes as a function of $\theta$ and $c$, with probe positions given in Table 5.1. The probe positions were measured using a calibrated optical microscope (Zeiss - Axio Icc.1, Carl Zeiss AG, Oberkochen, Germany) with a resolution of 1.86 $\mu$m per pixel.

**Table 5.1:** Position of laser Doppler probes

| **Probe** | $x$ | $y$ |
|---|---|---|
| 1 | -0.67 | 1.15 |
| 2 | -1.15 | -0.67 |
| 3 | 0.67 | -1.15 |
| 4 | 1.15 | 0.67 |

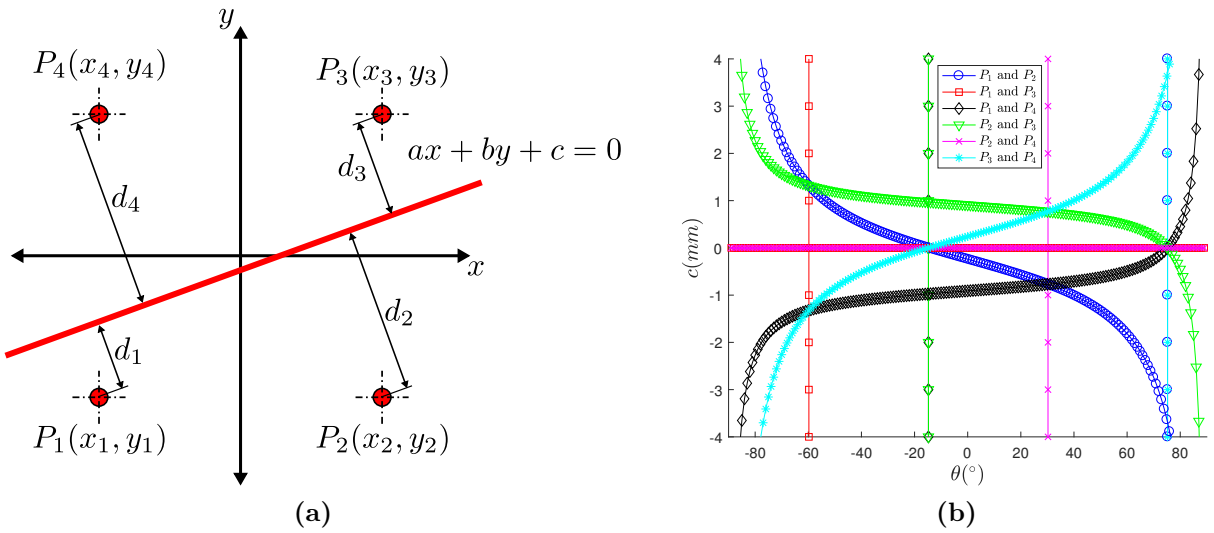


**Figure 5.5:** a) Representation of a vessel (red line approximation) detected by four probes ($P_1$, $P_2$, $P_3$, $P_4$); b) Boundary of the 24 classes as a function of two parameters, $\theta$ and $c$

Relative measurements between probes are used to define the area of $\theta$ and $c$ that could result in the same measurement output. Since four probes are used, there are $C_2^4 = 6$ comparisons to be made. Each comparison produces an area

$$A_k = \begin{cases} d_{k1} \leq d_{k2}, & \text{if } P_{k1} > P_{k2} \\ d_{k1} = d_{k2}, & \text{if } P_{k1} = P_{k2} \\ d_{k1} \geq d_{k2}, & \text{if } P_{k1} < P_{k2} \end{cases} \tag{5.6}$$

where $k = 1, 2, 3, 4, 5, 6$, $d_{k1}$ is the distance from the vessel to the first probe, with perfusion value $P_{k1}$, and $d_{k2}$ is the distance from the vessel to the second probe, with perfusion value $P_{k2}$. Possible vessel poses $A_v$ are given by

$$A_v = \bigcap_{i=1}^{6} A_k \tag{5.7}$$

An ideal sensor can discriminate a very small difference in off-axis vessel position. However, sensors used here were not ideal and thus suffered from limited sensitivity. Therefore, the boundary is included in equation 5.6 if $P_{k1} \neq P_{k2}$. In addition, a tolerance $d_l$ was used in the comparisons so that $\mid d_{k1} - d_{k2} \mid \leq d_l$ if $P_{k1} = P_{k2}$. As evident in Figure 5.3c, the higher the

perfusion value the steeper the slope between two off-axis distance. This means that $d_l$ is also a function of the perfusion value. Based on the characterisation results (Section 5.2.2), two ranges of $d_l$ were used so that

$$A_k = \begin{cases} \mid d_{k1} - d_{k2} \mid \leq 0.6, & \text{if } P_{k1} = P_{k2}, P_{k1} < 100AU \\ \mid d_{k1} - d_{k2} \mid \leq 0.2, & \text{if } P_{k1} = P_{k2}, P_{k1} \geq 100AU \end{cases} \tag{5.8}$$

A schematic and the experimental set-up for vessel pose classification are shown in Figure 5.6a and 5.6b, respectively. The needle was mounted in a rotation mount (RSP05/M, Thorlabs, New Jersey, USA) with a resolution of 2°, attached onto a three DOF linear stage with needle coordinates $(x, y, z)$ placed at the tip of the needle. The three DOF linear stage was used to change the $z$ position of the vessel and to make small adjustments during the "zeroing" calibration. As in Section 5.2.1, the gelatine box was mounted onto a kinematic base. To produce variable $c$ values, the two DOF lienar stage was translated in the $y_{st}$ direction. For $-90° < \theta < 90°$, the translation in $y_{st}$ for a given $c$ is

$$d_{st} = c \cos \theta \tag{5.9}$$

Experiments were conducted for three cases. To ascertain the feasibility of the algorithm, a first set of experiments was carried out at 0°, for five $c$ positions (0.40, 0.20, 0.00, -0.20, -0.40 mm). For each position, the perfusion values were measured for the vessel phantom at -1.80 - 0.00 mm $z$ position, with 0.30 mm increments. Based on these results, the second set of experiments was performed for 24 random pairs of $c$ and $\theta$ values (Table 5.2). For each pair, the vessel was located at $z = -0.60$ mm. For all of the classification experiments, the flow velocity rate was set at 20 mm/s, with a 0.6 mm internal diameter capillary tube inside the grey matter phantom. The third set of experiments were performed using a 0.3 mm diameter vessel phantom at 0° and 0 mm $c$ position. The perfusion values were measured for the vessel phantom at -0.90 - 0.00 mm $z$ position, with 0.30 mm increments. All measurements were repeated at least 8 times. The classification was done based on the statistically significant

difference between measurements of each probe at a given position.

Due to the close distance between the probes (≈ 1.9 mm). Cross talk between each probe was observed. To avoid cross talk between each probe, the measurements were conducted by activating each channel in turn, after an initial calibration of each probe separately, using motility standard provided by the manufacturer. The perfusion value from each probe was recorded for 5 s. The average value of this measurement was used to compare measurements between the probes.

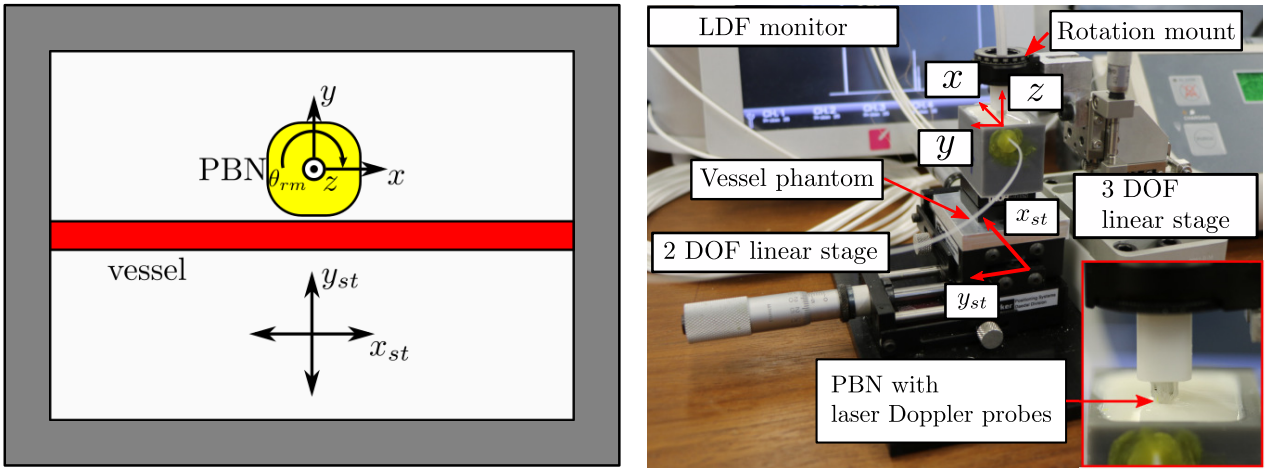


**(a)** **(b)**

**Figure 5.6:** a) A schematic diagram of vessel detection experiments with the needle coordinate system ($x$, $y$, $z$) located at the tip of the needle. The needle can be rotated with respect to its axis ($\theta_{rm}$) to change the $\theta$ value. Moving the sample box in $y_{st}$ direction changes the $c$ value. By moving the needle in the direction of $x_{st}$, more than one insertion can be done in a sample. b) Experimental set-up used for vessel classification. The vessel and grey matter phantom were placed on top of a 2 degree of freedom (DOF) linear stage that can be moved in the $x_{st}$ and $y_{st}$ directions. The PBN was mounted on a rotation mount fixed to a three DOF linear stage

### 5.3.2 Results

All of the data were checked for normality using the Shapiro-Wilk normality test, with $p = 0.01$. Comparisons of perfusion values between each probe were performed using a one-way ANOVA, with post-hoc Tukey test. As can be seen from Figure 5.7a - Figure 5.7e, a high perfusion value (> 120 AU) started to be detected in one of the probes at $z = -1.20$ mm. Hence, the classification algorithm was executed based on measurements at $= -0.60$ mm, which is midway between the first detected $z$ position and the tip of the needle.

For $\theta = 0°$, in the first experiments all of the vessel angles were correctly predicted. There is one error in the estimate for $c = 0.40$ mm, where the difference between the actual $c$ value with the predicted value was 0.06 mm. All possible vessel poses are drawn as a grey area in Figure 5.7f - 5.7j. The predicted values for 24 random pairs of $\theta$ and $c$ have 1.6° and 0.37 mm RMS error respectively, where the RMS error for $\theta$ is less than the resolution of the rotation mount. High errors in $c$ are found mainly for poses where the angle approaches 90° (Table 5.2) and further data analysis was conducted to check for the source of these errors. As described in section 5.3.1, to set $c$, the linear stage was translated in the $y_{st}$ direction by $d_{st}$. To check for the sensitivity of $d_{st}$ as a function of $\theta$, directional error was used

$$\mathrm{dir}_{\mathrm{error}} = c_{error} \cos\theta \tag{5.10}$$

The directional RMS error was found to be 0.1 mm, which is equal to the uncertainty of finding the zero position of the vessel. Figure 5.8a shows perfusion values while the probes approach a vessel with a 0.3 mm diameter. A high perfusion value started to be detected at $z = -0.6$ mm. The classification algorithm was executed at $z = -0.3$ mm. The vessel angle and position were correctly predicted by the algorithm as can be seen in Figure 5.8b.

**Table 5.2:** Pairs of $\theta$ and $c$ values that were used during the experiments and the prediction error

| $\theta$ (°) | -80 | -50 | -50 | -40 | -30 | -30 | -20 | -10 | -10 | 0 | 10 | 20 | 20 | 40 | 40 | 50 | 50 | 70 | 70 | 80 | 80 | 90 | 90 | 90 |
|---|---|---|---|---|---|---|---|---|---|---|---|---|---|---|---|---|---|---|---|---|---|---|---|---|
| $\theta_{\mathrm{error}}$ (°) | 0.0 | 3.6 | 0.0 | 0.0 | 0.0 | 0.0 | 0.0 | 0.0 | 0.0 | 0.0 | 0.0 | 0.0 | 0.0 | 0.0 | 0.0 | 0.0 | 0.0 | 0.0 | 0.0 | 1.6 | 1.6 | 6.4 | 0.0 | 0.0 |
| $c$ (mm) | -1.60 | 0.80 | -1.00 | -0.40 | 0.80 | 1.20 | -1.20 | 0.20 | -1.80 | -0.80 | 1.00 | -0.40 | 0.40 | -0.40 | 0.60 | -1.60 | 2.00 | 1.20 | -2.0 | -2.00 | 2.00 | 0.20 | 1.00 | -2.00 |
| $c_{\mathrm{error}}$ (mm) | 0.71 | 0.15 | 0.07 | 0.00 | 0.03 | 0.00 | 0.00 | 0.00 | 0.00 | 0.00 | 0.30 | 0.00 | 0.18 | 0.00 | 0.00 | 0.07 | 0.00 | 0.59 | 0.00 | 0.00 | 1.49 | 0.29 | 0.00 | 0.00 |
| $\mathrm{dir}_{\mathrm{error}}$ (mm) | 0.12 | 0.10 | 0.04 | 0.00 | 0.03 | 0.00 | 0.00 | 0.00 | 0.00 | 0.00 | 0.30 | 0.00 | 0.17 | 0.00 | 0.00 | 0.04 | 0.00 | 0.20 | 0.00 | 0.00 | 0.26 | 0.29 | 0.00 | 0.00 |

### 5.3.3 Sensitivity Analysis

#### Methods

If a vessel is not perpendicular to the insertion axis, the axial distance ($d_{ax2}$ and $d_{ax3}$, see Figure 5.9) from the vessel to each one of the probes may not be the same. Here, the tilt angle was defined as the angle between the vessel with the $xy$-plane ($\alpha$ in Figure 5.9). To investigate the sensitivity of the method developed in this chapter to the assumption that the vessel is

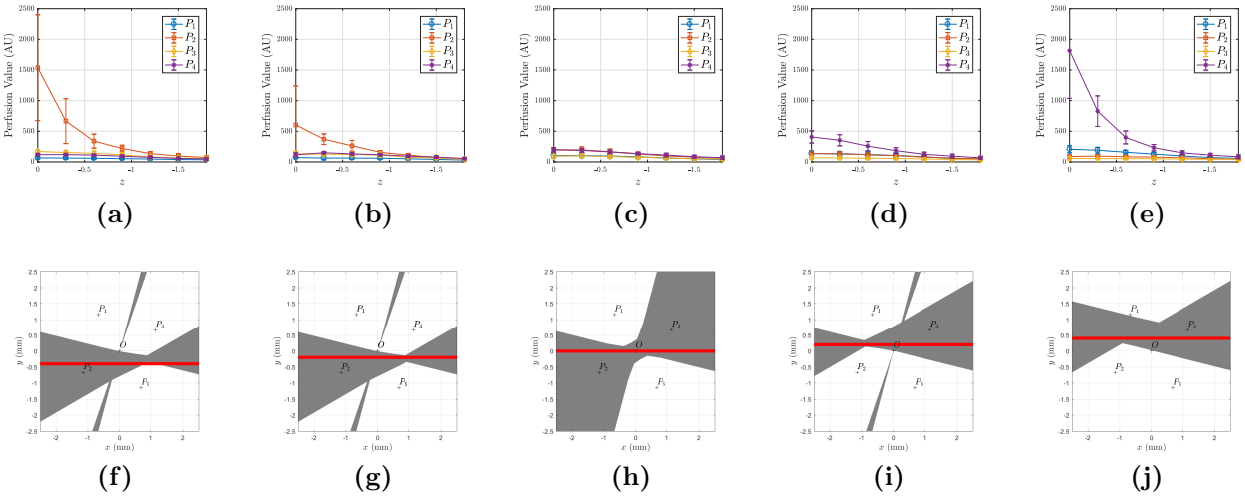


**Figure 5.7:** Perfusion values of four probes during insertion of the needle approaching a 0.6 mm vessel at different depths, starting at $z = -1.80$ mm with the following values for $c$: a) $c = 0.40$ mm, b) $c = 0.20$ mm, c) $c = 0.00$ mm, d) $c =$ -0.20 mm, and e) $c =$ -0.40 mm. Possible vessel poses predicted using relative measurement of four probes: f) $c = 0.40$ mm, g) $c = 0.20$ mm, h) $c = 0.00$ mm, i) $c = -0.20$ mm, and j) $c = -0.40$ mm. Predictions were made at $z = -0.60$ mm. Grey area: predicted vessel pose, red line: vessel pose, $P_1$: probe 1, $P_2$: probe 2, $P_3$: probe 3, $P_4$: probe 4, $O$: tip of the needle

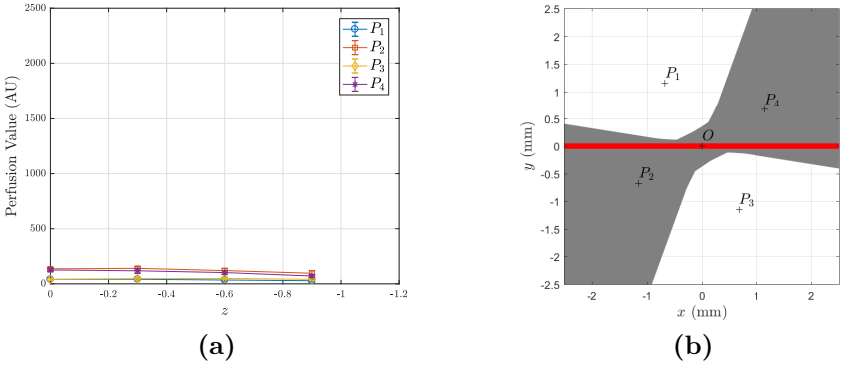


**Figure 5.8:** a) Perfusion values of four probes during insertion of the needle approaching a 0.3 mm vessel at different depths, starting at $z = -0.90$ mm with $c = 0$ and $\theta = 0°$. b) Possible vessel poses predicted using the algorithm developed in this section. Prediction was made at $z = -0.30$ mm. Grey area: predicted vessel pose, red line: vessel pose, $P_1$: probe 1, $P_2$: probe 2, $P_3$: probe 3, $P_4$: probe 4, $O$: tip of the needle

perpendicular to the insertion axis (i.e. the tilt angle is zero), additional characterisation of the grey matter phantom was conducted. Using 20 mm/s flow velocity, the perfusion values in the range of -2.0 - 2.0 mm off-axis position were measured in 0.2 mm increments at 6 vessel depths (0.3, 0.6, 0.9, 1.2, 1.5, and 1.8 mm). The characterisation results were thus used as a look-up table to approximate the measurements of each probe at certain axial ($d_{ax}$), and off-axis ($d$) distances from a vessel for a given tilt angle. The method to predict the vessel pose developed

in this chapter was then used to check the maximum tilt angle that would still allow the vessel pose to be predicted correctly. The maximum tilt angle of the vessel was investigated for $\theta$ values ranging from -80° to 90° in 10° increments and a $c$ value ranging between -2.4 mm to 2.4 mm in 0.2 mm increments. The vessel was located at $z = -0.60$ mm. For $\theta \neq 90°$ the centre of the rotation was at the $y$-intercept, and for $\theta = 90°$ the centre of rotation was at the $x$-intercept.

In addition, a Monte Carlo simulation (de Mul et al. 1995, de Mul 2004) were performed to investigate the effect of changing the optical properties ($\mu_s'$ and $\mu_a$) of the tissue. The simulation was carried out for $\mu_s'$ values of 0.55, 0.75, and 0.95 mm$^{-1}$, and $\mu_a$ values of 0.005 mm$^{-1}$ and 0.05 mm$^{-1}$ (grey matter $\mu_a$ (Yaroslavsky et al. 2002)), for 20 mm/s flow velocity. Additional simulations of vessel pose predictions were then performed to investigate the effect of optical properties on the prediction area.

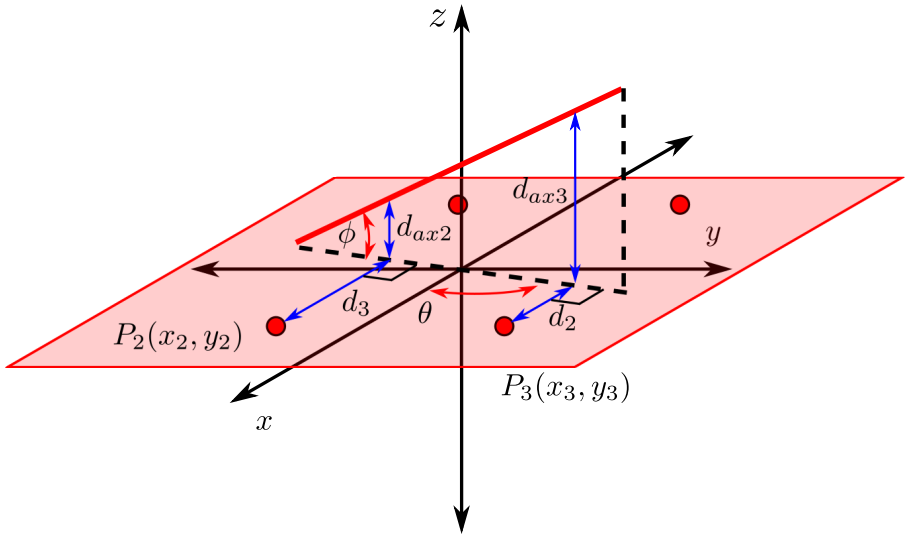


**Figure 5.9:** Representation of a vessel (red line approximation) with a tilt angle $\alpha$. The axial distance from $P_2$ to the vessel ($d_{ax2}$) is not equal to the axial distance from $P_3$ to the vessel ($d_{ax3}$). The projection of the vessel in the $xy$-plane has an angle of $\theta$ with respect to the $x$-axis.

### Results

Figure 5.10c shows the maximum tilt angle that the vessel prediction algorithm can handle. The average value of the tilt angle is ± 13°. The simulation shows good agreement with the experiment (Fig. 5.10a). All perfusion values were normalized against the perfusion value at

0.3 mm depth and 0.00 mm off-axis value. Fig. 5.10b shows the effect of optical properties on the perfusion value. The highest perfusion value corresponds to $\mu_s' = 0.55$ mm$^{-1}$ and $\mu_a = 0.005$ mm$^{-1}$, while the lowest perfusion value corresponds to $\mu_s' = 0.95$ mm$^{-1}$ and $\mu_a = 0.05$ mm$^{-1}$. The simulations were performed by setting different optical properties in front of each probe. The parameter variation was based on the optical properties that result in the highest and the lowest perfusion value. The results show that predictions remain valid up to a maximum error of 10° in $\theta$ and of 0.5 mm in $\text{dir}_{\text{error}}$.

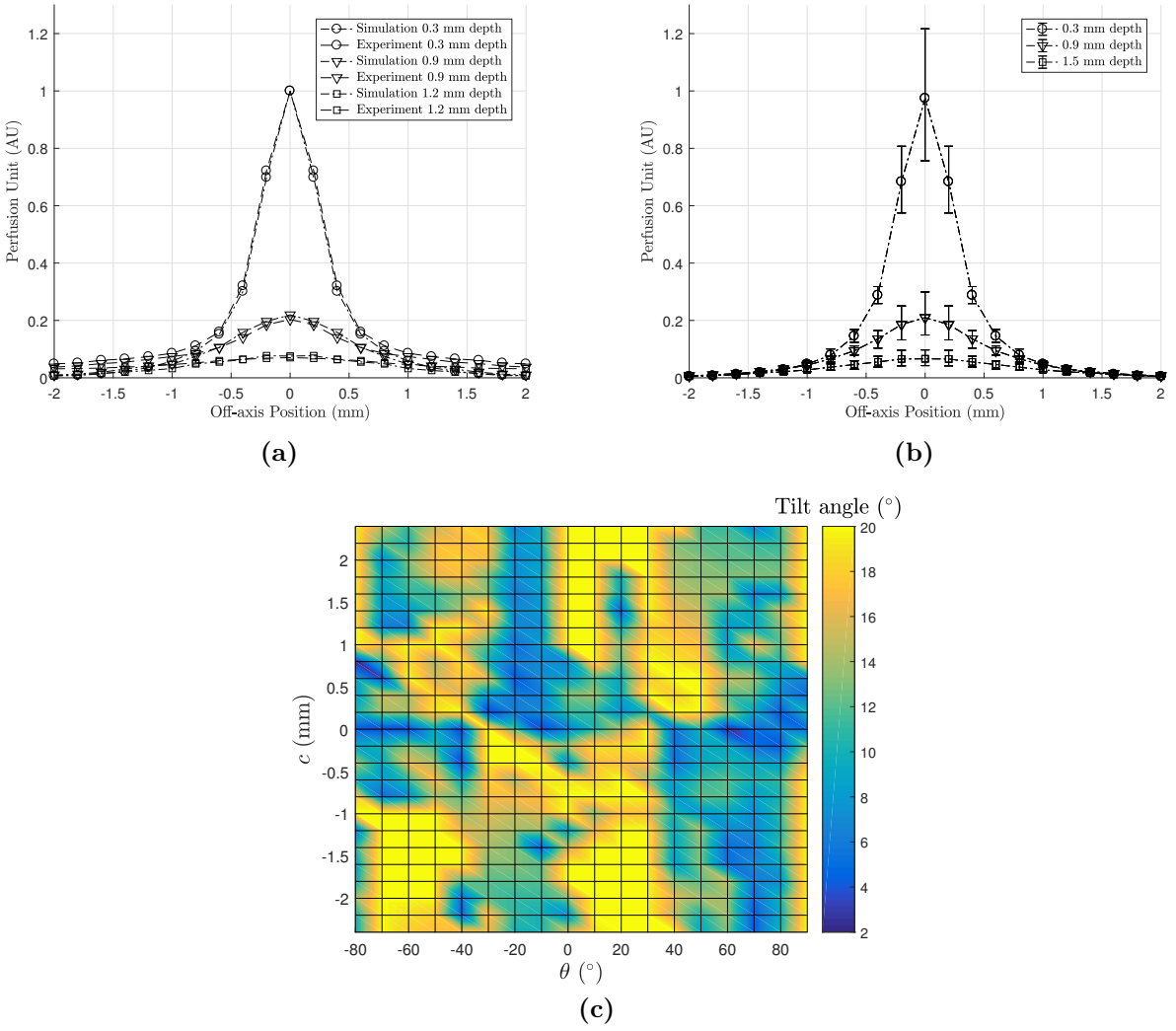


**Figure 5.10:** a) Comparison of the normalized perfusion value between experiments (dash line) and simulation (dash-dot line) for three depth position (0.3, 0.9 and 1.5 mm). b) The mean normalized perfusion value of simulation results for various optical properties ($\mu_s'$: 0.55 - 0.95 mm$^{-1}$ and $\mu_a$: 0.0053 - 0.028mm$^{-1}$) for three depth position (0.3, 0.9 and 1.5 mm). The error bar shows the maximum and the minimum perfusion value, c) colour-map of the maximum tilt angle that can still be predicted correctly by the method described in this chapter.

## 5.4 Discussion

Static and dynamic characterisation of a laser Doppler probe have been investigated in this chapter. Based on the static experiments, the laser Doppler monitor used here was found to have a maximum dynamic range of 20 mm/s for both vessel sizes. However, an artery with a diameter of $\approx$ 1 mm could have a flow velocity of up to 150 mm/s (Piechnik et al. 2008), which would be much higher than the dynamic limit of the commercial laser Doppler monitor used here. The development of a laser Doppler monitor that has higher dynamic range would thus be necessary, which is included as recommendation for future works in Chapter 7.

The tissue's bulk movement is considered to be a significant problem in the use of laser Doppler systems (Liang et al. 2013, Öberg 1999, Fredriksson et al. 2009). Since tissue is also a scattering object, the movement of the tissue is measured by an LDF system that generates a higher perfusion value that it should. To avoid this, Wårdell et al. (2016) measured the perfusion along the DBS implantation path in an incremental manner. The characterisation of perfusion values with different constant insertion speeds shows that there is an additional, approximately constant perfusion offset that scales up linearly as a function of insertion speed. The materials in front of the tip of the needle are displaced during the insertion process. The Particle Image Velocimetry (PIV) method has been used to investigate the displacement and to track material point trajectories (Oldfield et al. 2014). They found that the material point trajectories in front of the needle are quasi-static during constant insertion speed, and as such, these result in a constant background offset. Changing the optical properties could change the depth penetration of the light. However, since during the course of the insertion, the distribution of material point trajectories in front of the needle is quasi-static, it is believed that the background perfusion value would hold constant as well.

Figure 5.4c shows that a vessel located in front of the probe can still be detected by observing a monotonic increase of the perfusion value. Using 0.2 mm/s insertion speed, for instance, it takes $\approx$ 7 minutes for full insertion of a 75 - 89 mm DBS electrode. This result demonstrates that detecting a vessel in front of a continuously advancing needle using a robotic assisted needle insertion system, combined with LDF, is indeed possible.

The novel vessel pose classification algorithm employing multiple laser Doppler probes embedded within in a PBN shows an angular RMS error of 1.6° and translational RMS error of 0.1 mm. Both of these errors are within the repeatability of the experimental set-up itself, which is encouraging. As can be seen in Figure 5.3c, the closer the vessel is to the Doppler probe, the higher the perfusion value. This relationship still holds for any set of homogeneous tissue optical properties. Therefore, even though specific tissue optical properties and vessel properties generates in front of each probe is high, the algorithm may fail to predict the vessel pose correctly. This eventuality is unlikely due to the close proximity between the four probes ($\approx$ 1.9 mm), as the tissue optical properties are not likely to vary significantly within such a confined space.

It should be noted that the prediction area corresponds to the area where the axis of the vessel lies. The classification algorithm is based on the position of the laser Doppler probes and the number of probes used, which means an optimisation of the numbers and the position of the probes can be performed, for instance to obtain better vessel pose discrimination when $c$ is close to 0.

Unlike in Chapter 4, the axial distance ($z$) of the vessel from the tip of the needle cannot be discriminated here, however, due to the short axial detection range of the probe, a "no-go" region can be set from the tip of the needle up to 1.5 mm behind the predicted area. This no-go region can be loaded into an obstacle map that can be used to generate a new path to avoid the detected vessel. As has been explained in Chapter 4, the short axial detection range means that a short retraction might be required to properly avoid the vessel. Oldfield et al. (2014) showed that there is tissue deformation around the needle during the insertion process, both in front of it and at the tissue-needle interface. Based on this work and the work of Liang et al. (2013), it seems probable that a blood vessel would also move with the surrounding brain tissue, but sensors measurements could be used to update the vessel position in real time.

Finally, in this chapter, an assumption that a vessel lies in a plane perpendicular to the insertion axis was used. In fact, the sensitivity analysis shows that the average tilt angle that the method can handle is $\pm$ 13°. As can be seen in Figure 5.10c, the maximum tilt angle varies depending on

the vessel pose. The variation depends on whether the perfusion value order (from the highest to the lowest) for the four probes, changes. If the tilt angle does not introduce a change, the vessel pose will be robustly predicted even though a high tilt angle is present. To solve for possible vessel poses which do not comply with this restriction, a continuous update of the vessel classification, while the needle is steered around the vessel, would be needed.

## 5.5 Conclusion

In this chapter, multiple forward-looking sensors for vessel pose classification were used in a 4 mm prototype of a bio-inspired programmable bevel-tip needle. The sub-millimetre accuracy results show a significant improvement compared to the method explained in Chapter 4. In addition, the method used here can be applied to any tissue optical properties without the need for the sensor's inverse model. Using an assumption that a vessel lies in a plane perpendicular to the insertion axis, the model can still predict a safe area even for a vessel that has a tilt angle of 13°. However, several vessel parameters such as axial distance from the vessel to the probe and the vessel diameter cannot be inferred. The next chapter, Chapter 6, discusses the use of machine learning technique based on a Long Short-Term Memory (LSTM) network to solve these problems. The machine learning technique combines the findings of Chapter 4 and Chapter 5, where successive measurements from a four-channel laser Doppler probe system are used to define a "no-go" area.

# Chapter 6

# A Long Short-Term Memory Network to Predict Vessel Pose in a Steerable Needle

## 6.1 Introduction

Chapter 4 and Chapter 5 showed that vessel detection is possible with a PBN coupled with a commercial laser Doppler flowmetry (LDF) system. The LDF sensor detects a vessel by measuring the Doppler shift effect in the light refracted by the moving blood cells flowing within it. Since a perfusion value corresponds to many vessel positions, in Chapter 4, successive measurements combined with a lookup table of the inverse perfusion value (measured under controlled conditions with varying parameters) were used to determine the axial ($d_{ax}$) and off-axis ($d$) distance from the tip of the probe to the vessel (Figure 6.1). Based on $d_{ax}$ and $d$ values for two LDF probes, the vessel pose could be predicted. However, this method only works for a given pair of tissue and vessel properties (e.g. a 0.6 mm vessel diameter with 5 mm/s flow velocity rate). In Chapter 5, relative measurements between each probe were used directly to classify the "no-go" area. Using relative measurements, the perfusion value of each probe was normalised so that this method is applicable to any set of tissue optical properties.

However, there are several limitations in the algorithm presented in Chapter 5, such as the inability to predict vessel diameter or the axial distance $d_{ax}$ from the vessel to the probe. Also, the assumption that the vessel lies on a plane perpendicular to the insertion axis represents an important limitation of the method.

Under real conditions, neither the vessel nor the tissue properties are known beforehand. Hence, in this chapter, a feasibility study is presented where a Long Short-Term Memory (LSTM) network is employed to infer information about vessel pose based on successive LDF probe measurements. LSTM represents an effective means to capture the long-term dependency of sequential data (Greff et al. 2017). Here, the perfusion values recorded while the needle is moving are considered as sequential data to feed the network. This chapter consists of two main sections. Firstly, section 6.2 investigates the ability of the LSTM network to predict diameter ($\varnothing$), axial distance ($d_{ax}$), and off-axis distance ($d$) of a vessel based on successive measurements from a single probe (see Figure 6.1). Secondly, Section 6.3 discusses the development of the LSTM network to directly predict the "no-go" area that was inferred from successive measurements from four laser Doppler probes. The results are then discussed in Section 6.4, with conclusions and a summary in Section 6.5.

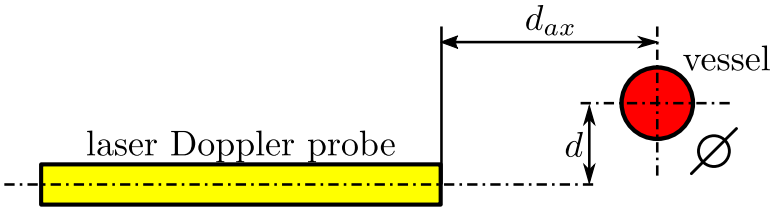


**Figure 6.1:** Axial distance $d_{ax}$ and off-axis distance $d$ from the tip of the LDF probe to a vessel with a certain diameter ($\varnothing$)

## 6.2 Single Probe Vessel Detection

### 6.2.1 Materials and Methods

LSTMs require a large number of training data sets, which would be impractical to acquire experimentally, as in previous chapters. Therefore, a Monte-Carlo simulation (de Mul et al.

1995, de Mul 2004) was performed, using a software developed by de Mul et al. (1995) to model measurements from an LDF system. As described in Larsson et al. (2002), the detection fibre was modelled using a ring detector (see Figure 6.2). In each run, the simulation was stopped if there were 100,000 photons detected in the detector. The detail of the method to compute the perfusion value from the simulation is explained in Larsson et al. (2002). Each simulation was performed twice and the average of the two was taken. The simulations were compared to the characterisation results for a 0.6 mm diameter vessel phantom with 20 mm/s flow velocity, acquired with the phantom set-up described in Chapter 5.2.1.

The simulation was then extended to model the perfusion value for 0.3, 0.6, and 0.9 mm diameter vessels, with $\mu_s'$ equal to 0.55, 0.75, and 0.95 $mm^{-1}$. The flow velocities were arbitrarily set at 10, 15, and 20 mm/s, values in the range of biological blood flow in smaller vessels. For each set of optical properties, the perfusion values were simulated at off-axis positions ranging from 0 mm to 2 mm in 0.2 increments and at axial positions ranging between 0.75 mm to 4.05 mm, in 0.3 mm increments. For each vessel diameter, the maximum and the minimum simulated perfusion value at a certain vessel position from the probe tip were recorded. Since a simulation takes $\approx$ 3 minutes to run, these maximum and minimum data were subsequently used in the form of a look-up table. To generate training datasets, the perfusion value for a certain vessel diameter at a given position was generated based on a random number uniformly distributed between the maximum and the minimum perfusion value at that point. The uniformly distributed perfusion value assumption means that the probabilities for $\mu_s'$ and the vessel flow velocity were uniform. Gaussian noise with zero mean was subsequently added to the generated perfusion value to simulate the shape of a real signal. The standard deviation used for the Gaussian noise was obtained from the characterisation results. A perfusion value between simulated positions was approximated using a two-dimensional interpolation.

A Recurrent Neural Network (RNN) uses the previous state at time $t-1$ with the current data point as an input for the network (Lipton et al. 2015). Therefore, it can capture the long-term dependencies hidden within sequential data. LSTM is a special RNN structure that consists of a memory cell that acts as an accumulator of state information (Xingjian et al. 2015). The flow of the information from and to the cell is controlled by three gates: input, forget, and output.

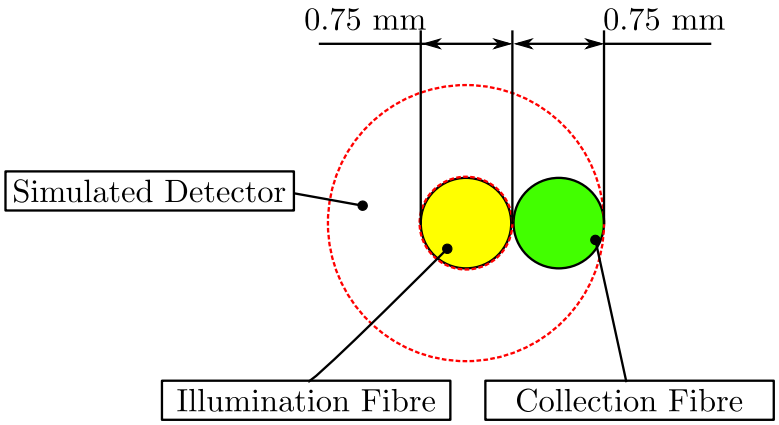


**Figure 6.2:** Schematic diagram of the detector that was used in the simulation. The detector was modelled as a ring detector between two red-dashed circles

Using these gates, LSTM overcomes the vanishing gradient problem of a standard RNN by trapping the gradient in the cell so that it does not vanish too quickly (Hochreiter & Schmidhuber 1997). In this section, the LSTM network was used to predict the probability of vessel parameters $V(\varnothing, d_{ax}, d)$ based on perfusion measurements $Perf_1, Perf_2, Perf_3, \ldots, Perf_t$. Mathematically, this is equivalent to computing:

$$P(V(\varnothing, d_{ax}, d) \mid Perf_1, Perf_2, \ldots, Perf_t) \tag{6.1}$$

To obtain a value for the probability in equation 6.1, the measurement range of the sensors was discretised with 0.1 mm resolution for three vessel diameters (0.3, 0.6, and 0.9 mm). One set of parameters in the discretised element $(\varnothing, d_{ax}, d)$ represents an output class of the network. The problem then becomes that of a multi-class classification. The mean perfusion value in the absence of a vessel was 28 AU, with a standard deviation of 8 AU. The perfusion limit of a detected vessel was then set at 55 AU (the mean perfusion value in the absence of a vessel plus three times its standard deviation). Using this perfusion limit, there were 659 classes where the vessel was inside the detection range of the probe (103, 225, and 331 classes for 0.3, 0.6, and 0.9 mm diameter, respectively). By adding the no-detection class (ND), the total number of classes was 660. Figure 6.3 shows a comparison of the probe detection range for each vessel diameter.

The hyper-parameters of the LSTM network were chosen manually: the number of layers was

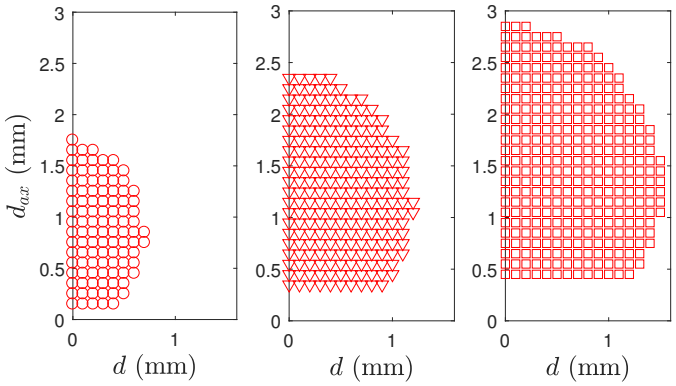


**Figure 6.3:** Detection area of the laser probe for each vessel diameter. Left: 0.3 mm diameter vessel, middle: 0.6 mm diameter vessel, right: 0.9 mm diameter vessel

empirically chosen to be 2, with 100 cells in each layer (Reimers & Gurevych 2017). To prevent over-fitting, a drop-out with a value of 0.5 was used (Zaremba et al. 2014). At the output layer, softmax was used to predict the probability of each class, so that:

$$P_i = \frac{e^{z_i}}{\sum_{j=1}^{K} e^{(z_j)}} \tag{6.2}$$

where $P_i$ is the probability of class $i$, $z_i$ is the output value of class $i$, and $K$ is the total number of classes. Vessel parameters $(\varnothing, d_{ax}, d)$ were chosen based on the class with the highest probability:

$$h = \arg\max_i P_i \tag{6.3}$$

where $h$ is the predicted class. The network was trained by minimising the cross entropy between the prediction output and the output of the training data set.

The training data set consisted of 30,000 sequences, with 30 positions in each series. 3,000 sequences were generated for validation, and another 3,000 were generated for testing. Since the minimum radius of curvature for the PBN prototype in Chapter 5 was experimentally measured to be 70 mm and the maximum $d_{ax}$ that can be detected by the sensor is only $\approx 2$ mm, the insertion was modelled as a straight line (i.e. with no change in $d$ between successive

positions). This is because the error introduced ($\approx 0.03$ mm) by this approximation falls below the resolution used to discretise the sensor detection range ($\approx 0.1$ mm). In terms of simulating measurements from representative needle insertions, the following criteria were observed:

- Equal measurement windows, arbitrarily set to 30 insertion positions per run, for all simulations, in order to facilitate input into the network, without the need for padding.
- A combination of insertion, extraction, and insertion followed by extraction, should be included in the training set, to ensure the network is not only able to identify a vessel, but also to track its position in the event of extraction and reinsertion.
- Simulations starting from a variety of distances from the vessel, including when the first measurement is right on the vessel to capture the event of a superficial capillary right on the tissue surface.

Consequently, each run was set and executed as follows:

1. At first, a class is chosen randomly.
2. The chosen class is then located randomly at one out of thirty possible positions between 0 mm and 8.7 mm away from the needle tip (dash-lines in Figure 6.4).
3. At the desired location, the position of the vessel is modified by addition of a uniformly distributed random value between -0.05 - 0.05 mm (a range that is equal to the resolution of the class) in both $d_{ax}$ and $d$ to ensure that a suitable population of candidates for a given class is used during training.
4. The simulated probe starts at position 0 in Figure 6.4.
5. If the axial distance from the probe to the vessel is bigger than the vessel radius plus 0.3 mm ($d_{ax} \geq \frac{\varnothing}{2} + 0.3$), the probe is moved forward with 0.3 mm increments (yellow squares in Figure 6.4).

6. At the first instance where $d_{ax} < \frac{\varnothing}{2} + 0.3$ (Point Q in Figure 6.4), the probe is moved either: forwards (Figure 6.4 top), backwards (Figure 6.4 middle), or is stopped (Figure 6.4 bottom), until the $30^{th}$ position is reached, at which point the simulation is terminated.

It should be noted that the off-axis positions of green and blue squares in Figure 6.4 are equal to the off-axis positions of the yellow squares. A vertical displacement for these two was included to ease visualisation. Since the movement direction of the probe is used as an additional training parameter, the input of the network was set to be:

$$\begin{bmatrix} Perf_t \\ \mathbf{F}^\intercal \end{bmatrix} \tag{6.4}$$

Where $Perf_t$ is the perfusion at time $t$, and $\mathbf{F}^\intercal$ is a $3 \times 1$ vector that defines the movement direction of the probe, with

$$\mathbf{F} = \begin{cases} \begin{bmatrix} 1 & 0 & 0 \end{bmatrix}, & \text{if the probe is moving backwards} \\ \begin{bmatrix} 0 & 1 & 0 \end{bmatrix}, & \text{if the probe is stopping} \\ \begin{bmatrix} 0 & 0 & 1 \end{bmatrix}, & \text{if the probe is moving forwards} \end{cases} \tag{6.5}$$

Figure 6.5 shows the distribution of the classes generated for the training dataset (please note that the no-detection class, which has a frequency of $\approx 57,0000$, is not shown in figure). Due to the way in which it was generated, the class distribution shows an imbalance in the training dataset, with three peaks representing classes with $d_{ax} \leq \frac{\varnothing}{2} + 0.3$ for 0.3, 0.6, and 0.9 mm vessel diameter, respectively. To solve this problem, Tran et al. (2018) used a cost matrix to penalise the loss from a class with a higher number of samples (i.e. a higher frequency of occurrence). The misclassification cost of class $i$ ($C[i,i]$) was thus defined as:

$$C[i,i] = \left(\frac{1}{n_i}\right)^{\gamma} \tag{6.6}$$

where $n_i$ is the number of samples in class $i$, and $\gamma \in [0,1]$ is a trade-off parameter.

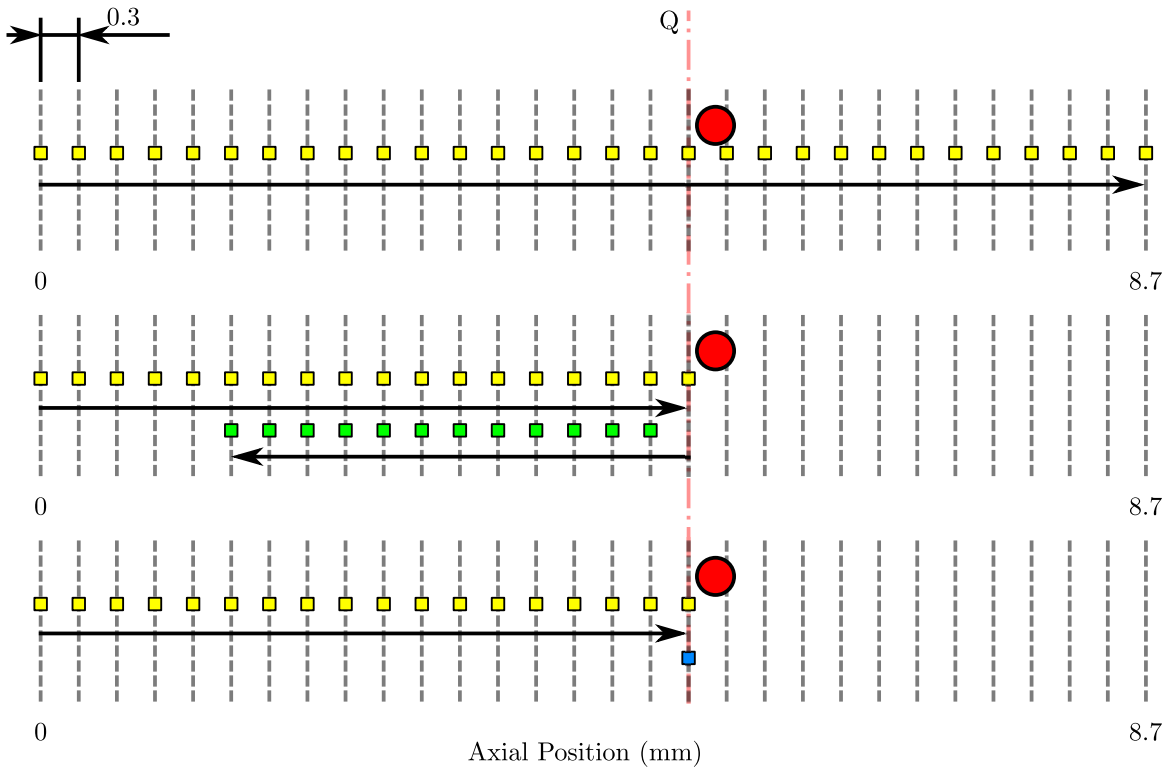


**Figure 6.4:** The dash-lines represent the thirty possible positions of the chosen class during the simulation. If $d_{ax} \geq \frac{\varnothing}{2} + 0.3$ the probe is moved forward. At the first instance where $d_{ax} < \frac{\varnothing}{2} + 0.3$ (Point Q), three possible probe movements are chosen until the $30^{th}$ position is reached: forwards (top), backwards (middle), and stop (bottom). Yellow squares represent probe positions while the probe is moved forward, green squares while the probe is moved backward, and the blue square while the probe is stopped. It should be noted that the off-axis distance of a simulation run is constant for all measurement points

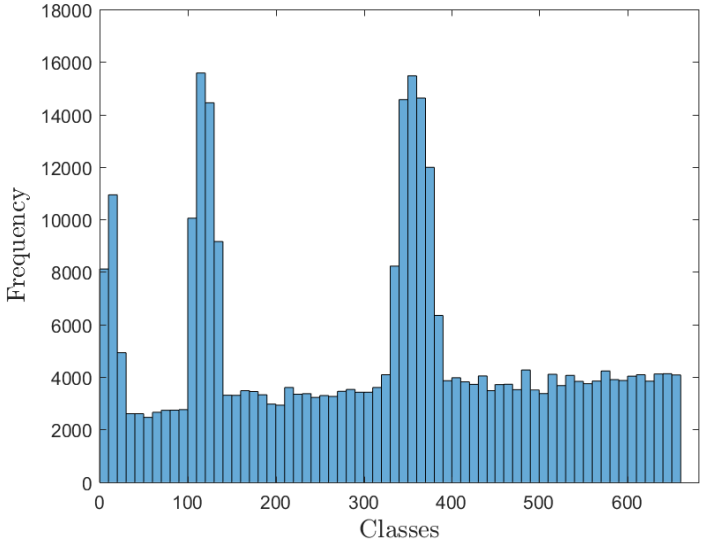


**Figure 6.5:** Distribution of the classes shows imbalance. In this histogram, the frequency of the no-detection class is not included, and has a value of $\approx$ 57,000

The performance of the network was assessed in three steps. Firstly, the optimum $\gamma$ value was obtained by using the validation dataset to evaluate the ability of the network to correctly detect the presence of a vessel inside the detection range of the sensor. The evaluation was performed by using a confusion matrix (Table 6.1). The confusion matrix classifies the prediction into four categories: true positive ($t_p$), true negative ($t_n$), false positive ($f_p$), and false negative ($f_n$). Since the dataset is highly imbalanced, *accuracy* ($\frac{t_p+t_n}{t_n+t_p+f_p+f_n}$) cannot be used to measure the performance of the trained network. Therefore, the following evaluation metrics were used (Tran et al. 2018):

$$\text{Precision} = \frac{\sum t_p}{\sum(t_p + t_n)} \tag{6.7}$$

$$\text{Recall} = \frac{\sum t_p}{\sum(t_p + f_n)} \tag{6.8}$$

$$F_1 = 2 \cdot \frac{\text{Precision} \cdot \text{Recall}}{\text{Precision} + \text{Recall}} \tag{6.9}$$

**Table 6.1:** Confusion matrix to find the optimise $\gamma$ value. $t_n$: true negative, $t_p$: true positive, $f_p$: false positive, $f_n$: false negative

| Actual \ Predictions | No-Detection | Vessel Detected |
|---|---|---|
| No-Detection | $t_n$ | $f_p$ |
| Vessel Detected | $t_p$ | $f_n$ |

Secondly, using the optimum $\gamma$ value, the confusion matrix for each vessel diameter was investigated using the test dataset. Thirdly, the network was used to predict the vessel parameters for real insertion experiments, where successive measurements from the insertion experiments in Chapter 5.3 were used to evaluate the performance of the trained network. The network was programmed in Python using the Tensorflow LSTM library.

### 6.2.2 Results

Figure 6.6a and 6.6b show a comparison between the simulated and measured perfusion values. To ease comparison, all perfusion values were normalised against the perfusion value at 0.75 mm axial and 0.00 mm off-axis distance. The simulation shows good agreement with the

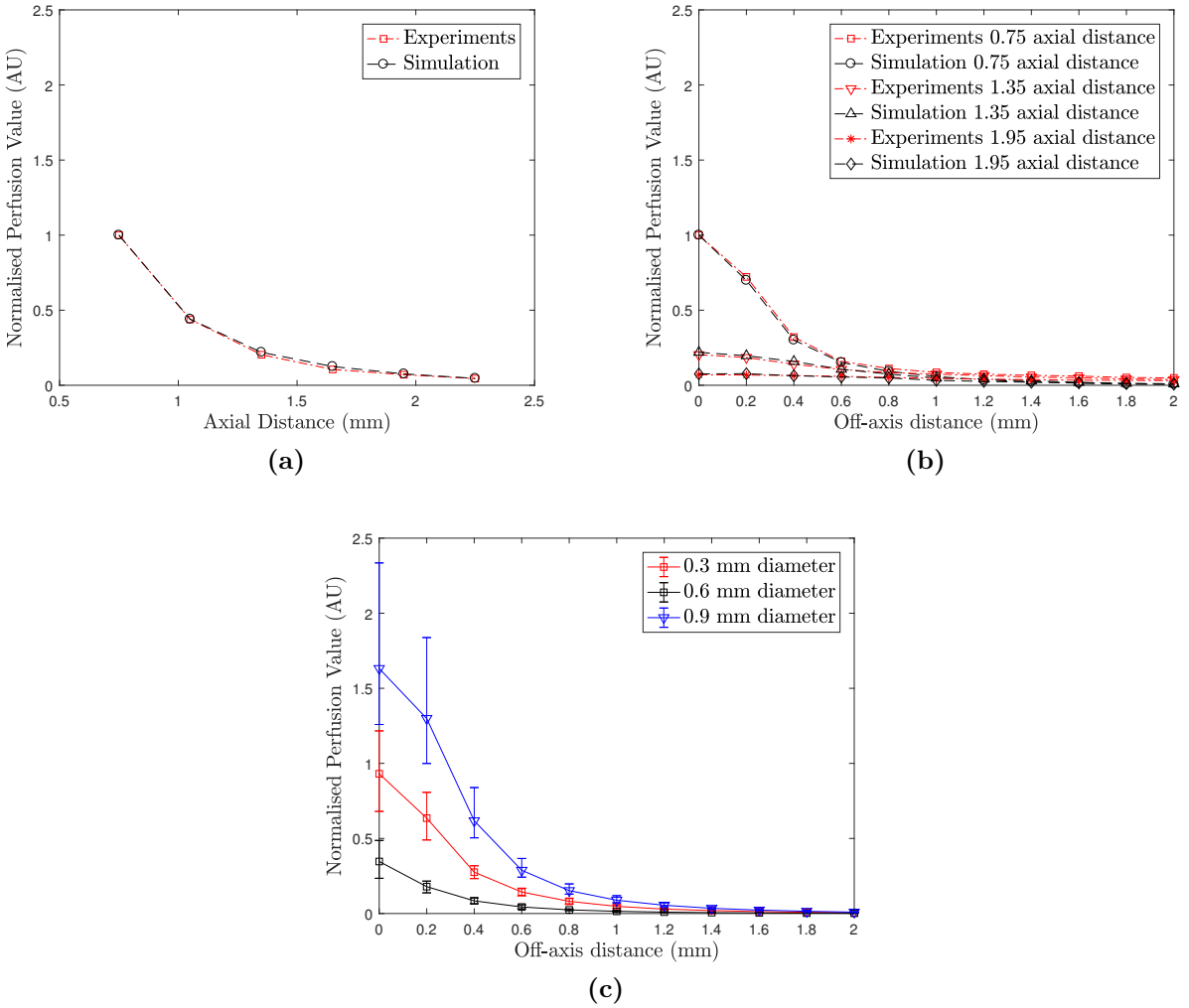


**Figure 6.6:** a) Comparison of the axial normalised perfusion value between experiments (dash-dot line) and simulation (dash-line) at 0 mm off-axis position; b) comparison of the off-axis normalised perfusion value between experiments (dash-dot line) and simulation (dash-line) at three axial distances: 0.75 mm, 1.35 mm, and 1.95 mm; c) The error-bar shows the maximum and minimum perfusion values for each vessel diameter at 0.75 mm axial distance, with varying tissue optical properties and flow velocity rates

experiments. The main focus of vessel detection in a steerable needle system is to obtain information about its pose and diameter. Therefore, the extended simulation results were used to show the possible range of perfusion values given a vessel diameter and position, with variable tissue optical properties and flow velocity rates. Figure 6.6c shows these perfusion ranges for each vessel diameter at 0.75 mm axial distance.

The optimum $\gamma$ value was obtained by training the network for 1,000 epochs while the value of $\gamma$ was set to a number between 0 and 1, in 0.1 increments. Figure 6.7 shows that the smaller the $\gamma$ value, the lower the Recall. However, the $\gamma$ value is also inversely related to Precision.

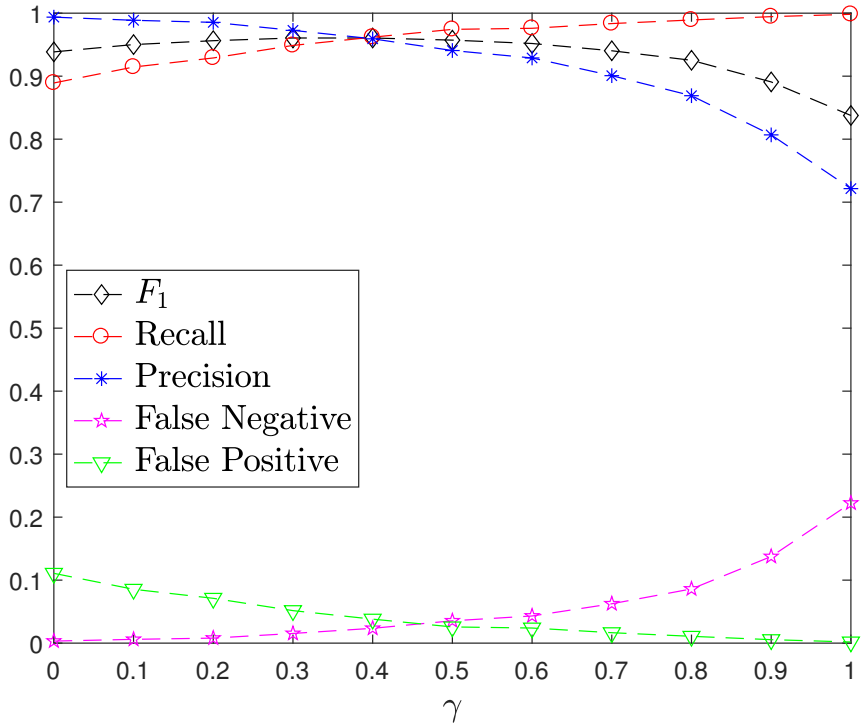


**Figure 6.7:** Network performance evaluation using Recall, Precision and $F_1$-score as a function of $\gamma$, with corresponding false positive and false negative values

The optimum value of $\gamma$ ($\gamma = 0.4$) was thus chosen based on the best $F_1$-score. Using this $\gamma$ value, the performance of the network was evaluated using the test dataset, which gave:

- Precision: 0.956
- Recall: 0.959
- $F_1$: 0.957

The second evaluation was performed to investigate the ability of the network to predict the correct diameter of the vessel. Table 6.2 shows the confusion matrix of this prediction. For the correctly predicted diameter, the root-mean-square errors (RMSE) of the position prediction were 0.14, 0.19, and 0.27 mm for 0.3, 0.6, and 0.9 mm vessel diameters, respectively. There were several cases where a vessel was predicted in the no-detection area state. Further analysis shows that it was in the area close to the maximum detection range of the sensor.

Finally, the network performance was evaluated using real data from insertion experiments. The insertions were performed and recorded at seven positions starting from 2.55 mm down

**Table 6.2:** Confusion matrix of the prediction using test data set generated from simulation, ND: No-detection

| Actual \ Predictions | ND | 0.3 | 0.6 | 0.9 |
|---|---|---|---|---|
| ND | 0.975 | 0.007 | 0.011 | 0.007 |
| 0.3 | 0.031 | 0.804 | 0.122 | 0.043 |
| 0.6 | 0.049 | 0.061 | 0.724 | 0.166 |
| 0.9 | 0.038 | 0.019 | 0.21 | 0.732 |

to 0.75 mm axial distance, with 0.3 mm increments. In total, there were 160 sequences (1120 samples). The experiments were only performed for a 0.6 mm in diameter vessel, with a 20 mm/s flow velocity rate. Figure 6.8a shows an example of successive perfusion values from the insertion experiment of a vessel with a 0.67 mm off-axis distance. Figure 6.8 shows the prediction probability of vessel parameters (diameter and positions) at points A, B, C, D, E, F, and G. The first row of each column in Figure 6.8 corresponds to the probability of a vessel with a diameter of 0.3 mm. The second and the third row correspond to a vessel with a diameter of 0.6 and 0.9 mm, respectively. The total prediction probability of the three rows in each column added with the no-detection state is equal to 1. At the end of the insertion (point G), the network correctly predicted the vessel diameter. The axial and off-axis distance predictions were 0.55 and 0.70 mm, respectively, where the actual axial distance at the end of the insertion was 0.75 mm.

**Table 6.3:** Confusion matrix of the prediction using data from insertion experiments, ND: No-detection

| Actual \ Predictions | ND | 0.3 | 0.6 | 0.9 |
|---|---|---|---|---|
| ND | 0.81 | 0.01 | 0.12 | 0.06 |
| 0.6 | 0.13 | 0.03 | 0.59 | 0.25 |

Table 6.3 shows the confusion matrix of predictions on the vessel diameter obtained for the insertion experiments data. The prediction in Table 6.3 has higher false negative and false positive rates compared to the predictions in Table 6.2. Similar to simulation results, false negative predictions were found for the experimental data points in the area close to the maxi-

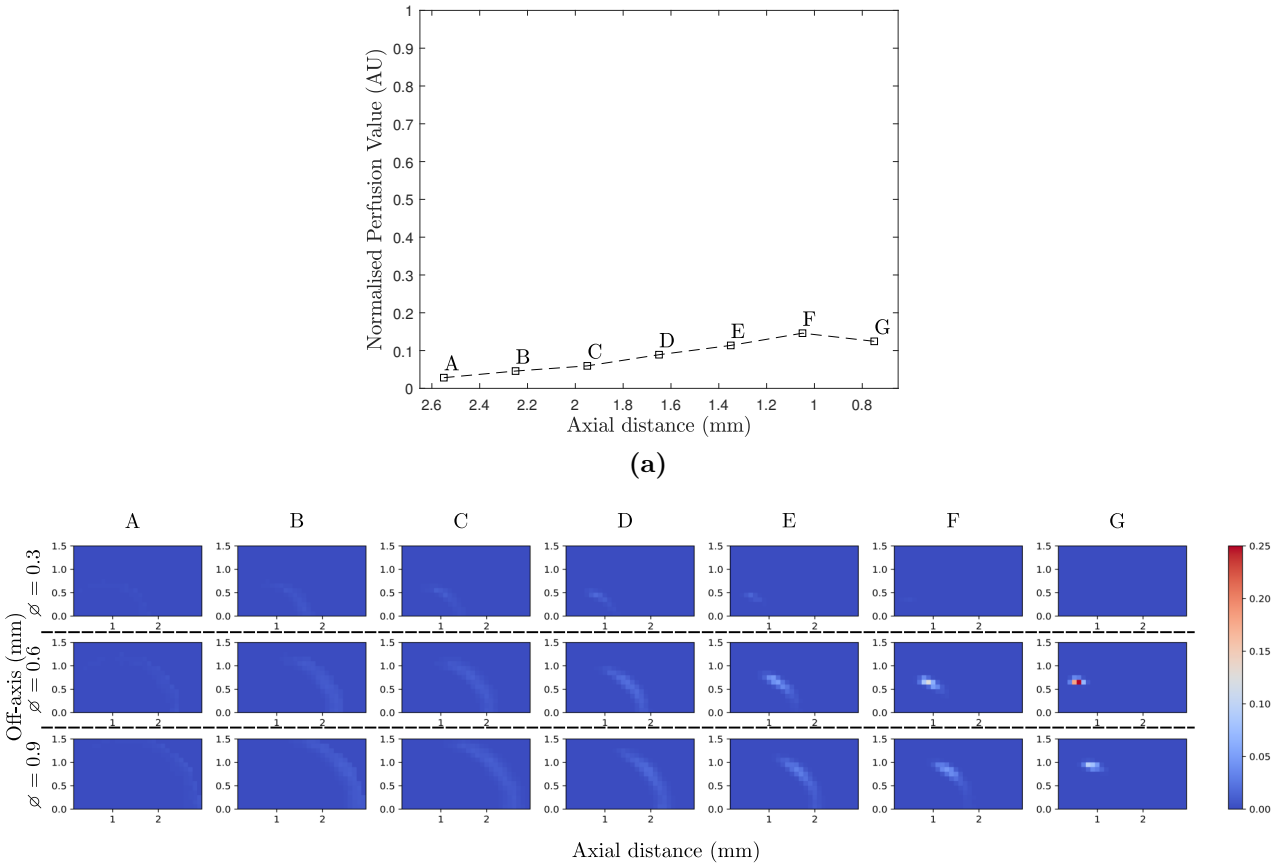


**Figure 6.8:** a) An example of insertion experiments with off-axis distance at 0.67 mm, which was used to evaluate the performance of the trained network; b) The prediction probability at instances A-G for three vessel diameters: 0.3 mm (top), 0.6 mm (middle), and 0.9 mm (bottom). The total probability of the three rows in each column added with the probability of no-detection is equal to 1. At the end of the insertion the actual position of the vessel was at 0.67 mm off-axis distance and 0.75 mm axial distance

mum detection range of the sensor. Nonetheless, for the correctly predicted diameter, position prediction RMSE of the experiments was 0.18, which is similar to the RMSE of simulation predictions (RMSE = 0.19).

## 6.3 Vessel Detection with Multiple Probes

In section 6.2, an LSTM was used to predict the vessel position and diameter from successive measurements of a single probe, but where the vessel's full pose in three-dimensional space remained unknown. This is because many different vessel poses can result in the same pair of off-axis and axial distances. To remove this ambiguity, in this section, the LSTM network was

modified to incorporate measurements from four forward-looking laser Doppler sensors.

### 6.3.1 Materials and Methods

The network has the same architecture as the LSTM network described in section 6.2.1: a two-layer LSTM with 100 LSTM cells in each layer. However, the input and the output were altered. Instead of using one perfusion value with a directional vector as an input, four perfusion values from four probes were simultaneously fetched and fed to the network. The input was presented in this form:

$$\begin{bmatrix} Perf_{1t} \\ Perf_{2t} \\ Perf_{3t} \\ Perf_{4t} \\ \mathbf{F}^{\intercal} \end{bmatrix} \tag{6.10}$$

where $Perf_{1t}, Perf_{2t}, Perf_{3t}, Perf_{4t}$ are the perfusion values for probe 1, 2, 3, 4 at time $t$, respectively. $\mathbf{F}^{\intercal}$ is a $3 \times 1$ vector that defines the movement direction of the probes, as described in 6.5.

Instead of specifying the vessel diameter and pose, in this section the network was used to predict the "no-go" area directly. To do this, firstly, the detection area of the sensors was defined (Figure 6.9). As can be seen, both the needle coordinate system $(x_n, y_n, z_n)$ and the probe coordinate system $(x_p, y_p, z_p)$ are located at the tip of the needle. The probe coordinate system is placed at an angle of -14.8° with respect to the needle coordinate system. The red-dash line in Figure 6.9 shows the off-axis detection area of the sensors. At a $d_{ax}$ distance from the probe, the off-axis detection area is a square with rounded corners. The radius of the rounded corner is equal to the maximum off-axis detection range of the sensor ($det_{ax}$) at that axial distance, where the side of the square ($dr_{ax}$) has a length of:

$$dr_{ax} = 2(d_{pn} + det_{ax}) \tag{6.11}$$

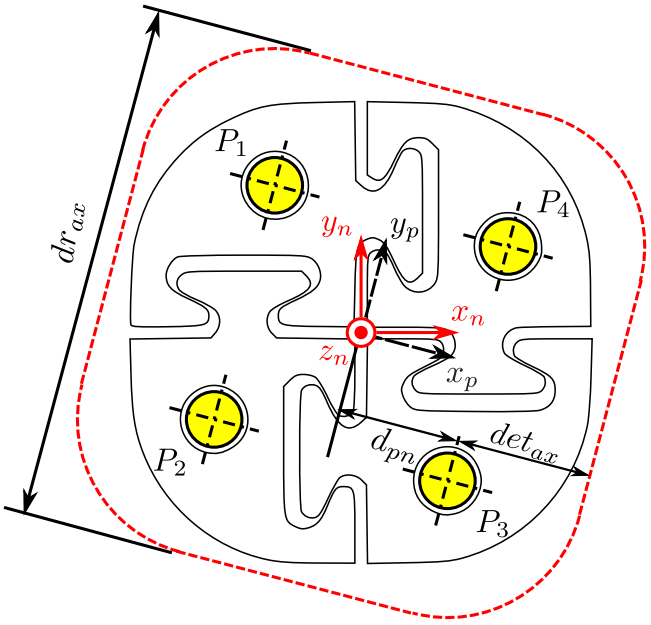


**Figure 6.9:** The red-dash line represents the detection range of the probe in the $x_p y_p$-plane. There are two coordinate systems shown, the needle coordinate system $(x_n, y_n, z_n)$ and probe coordinate system $(x_p, y_p, z_p)$. Both of the coordinate systems are located at the tip of the needle. with the second rotated $-14.8°$ with respect to the first. $P_1$: probe 1; $P_2$: probe 2; $P_3$: probe 3; $P_4$: probe 4; $d_{pn}$: distance from the probe to the $y_p$-axis; $det_{ax}$: maximum off-axis detection range at a certain axial distance; $dr_{ax}$: detection range for the four probes

where $d_{pn}$ is the distance from the probe to the $y_p$-axis. The position of each of the 4 probes in the needle coordinate system and in the probe coordinate system is listed in Table 6.4. The position of each probe in the probe coordinate system was calculated by

$$P_{n_p} = {}^{y_n}_{y_p}R \times P_{n_n} \tag{6.12}$$

where $P_{n_p}$ is the position of probe $n$ in the probe coordinate system, $P_{n_n}$ is the position of the probe $n$ in the needle coordinate system, and ${}^{y_n}_{y_p}R$ is the rotation matrix of the needle coordinate system with respect to the probe coordinate system. With the maximum axial detection range of the probes set at 2.4 mm, the detection volume was discretised into voxels, with the size of each voxel equal to $0.3 \times 0.3 \times 0.3$ mm. Using this voxel size, there were 1805 voxels inside the detection range of the sensors, where each voxel was used to represent a label (class). The network was then used to predict whether a voxel is safe (it is not occupied by a vessel) or it is not safe (it is occupied by a vessel). The voxel value is set into 0 if it is safe, while the value of not safe voxel is set to 1.

**Table 6.4:** Position of laser Doppler probes in the needle coordinate system $(x_n, y_n, z_n)$ and in the probe coordinate system $(x_p, y_p, z_p)$

| **Probe** | $x_n$ | $y_n$ | $z_n$ | $x_p$ | $y_p$ | $z_p$ |
|---|---|---|---|---|---|---|
| 1 | -0.67 | 1.15 | 0.3 | -0.94 | 0.94 | 0.3 |
| 2 | -1.15 | -0.67 | 0.3 | -0.94 | -0.94 | 0.3 |
| 3 | 0.67 | -1.15 | 0.3 | 0.94 | -0.94 | 0.3 |
| 4 | 1.15 | 0.67 | 0.3 | 0.94 | 0.94 | 0.3 |

Since the vessel can occupy several voxels at once, the problem becomes that of a multi-label classification where several labels (classes) can have a value of 1. It should be noted that it is a different problem compared to the multi-class classification in section 6.2. In multi-class classification, even though there are several classes, the prediction is chosen based on the class that has the highest probability value. To solve the multi-label classification problem, binary relevance is used instead. Binary relevance decomposes the multi-label learning into an independent binary learning problem for a $q$ number of classes (Zhang et al. 2018). The probability of each class was computed using logistic regression:

$$\sigma(z_i)_i = \frac{1}{1 + \mathrm{e}^{-z_i}} \tag{6.13}$$

where $\sigma(z_i)_i$ is the probability value of class $i$. The class prediction was defined by:

$$h_i = \begin{cases} 0, & \text{if } \sigma(z_i)_i < 0.5 \\ 1, & \text{if } \sigma(z_i)_i \geq 0.5 \end{cases} \tag{6.14}$$

where $h_i$ is the prediction of the class $i$.

The training dataset consisted of 18,000 sequences with 30 positions in each sequence. 9,000 sequences were generated for validation, and another 9,000 for testing. To generate successive measurements for training, validation, and test datasets, the vessel was assumed to be straight within the detection range of the sensor. The vessel coordinate system ($x_v, y_v, z_v$ in Figure 6.10) was used to define the orientation of the vessel, where the vessel always passes through the origin (i.e. $x_v = 0, y_v = 0, z_v = 0$). As can be seen in Figure 6.10, the vessel has an angle of

$\phi$ with respect to the $z_v$ axis and the projection of the vessel in the $x_v y_v$-plane has an angle of $\theta$. The orientation of the vessel was defined using these two angles. In the insertion simulation, the value of $\phi$ was randomised between 60° and 120° with 5° increments, while the value of $\theta$ was randomised between 0° and 175° with 5° increments. The vessel coordinates were then located in the global coordinate system $(x, y, z)$. The value of the vessel coordinate in the $z$ direction (i.e. depth) was chosen randomly to be one out of thirty possible ones ($z = 0$ to $z = -8.7$ mm in -0.3 mm decrements). For $\theta \neq 90°$, the location of the vessel coordinate in the $x$ direction was set to 0, while the location in the $y$ direction was chosen randomly between -2 and 2 mm, with 0.2 mm increments. For $\theta = 90°$, the $y$ position was set at 0 while the $x$ position was randomised between -2 and 2 mm with 0.2 mm increments. At the beginning of the insertion, the probe coordinate system ($x_p, y_p, z_p$ in Figure 6.10) was located at the origin of the global coordinate system ($x = 0, y = 0, z = 0$). The probe (green line in Figure 6.10) was located at a fixed position in the probe coordinate system. The probe coordinate system was then moved forward with a 0.3 mm increments. If the $z$ position of the probe coordinate system was less than the $z$ position of the vessel coordinate system, one out of three options was chosen for the next step until the $29^{th}$ step was reached: move backward, stop or move forward.

The value of class $i$ was set to 1 if the distance from the voxel in the global coordinate system to the vessel was less than the vessel diameter. The axial distance ($d_{ax}$) and off-axis distance ($d$) from the probe to the vessel were calculated using the simple line-to-line distance. The vessel and the probe were represented as lines expressed in parametric notation (Weisstein 2002*b*):

$$\mathbf{l_{pn}} = \mathbf{x_1} + (\mathbf{x_2} - \mathbf{x_1})t_1 \tag{6.15}$$

$$\mathbf{v} = \mathbf{x_3} + (\mathbf{x_4} - \mathbf{x_3})t_2 \tag{6.16}$$

where $\mathbf{l_{pn}}$ represents probe $n$, $n$ = 1,2,3,4, and $\mathbf{v}$ represents the vessel. The line $\mathbf{l_{pn}}$ passes through points $\mathbf{x_1}$ and $\mathbf{x_2}$ and the vessel passes through points $\mathbf{x_3}$ and $\mathbf{x_4}$. To check whether the lines are in a plane (coplanar) or not (skew), the following equation was used (Weisstein

2002*b*):

$$\mathbf{c} \cdot [\mathbf{a} \times \mathbf{b}] = c_p \tag{6.17}$$

where:

$$\mathbf{a} = \mathbf{x_2} - \mathbf{x_1} \tag{6.18}$$

$$\mathbf{b} = \mathbf{x_4} - \mathbf{x_3} \tag{6.19}$$

$$\mathbf{c} = \mathbf{x_3} - \mathbf{x_1} \tag{6.20}$$

The lines were coplanar if $c_p = 0$, otherwise they were considered to be skew lines. If two lines are in the same plane, they must be either parallel or intersect. The value of $d_{ax}$ and $d$ were then calculated by:

$$d = \begin{cases} \left| \frac{\mathbf{a}}{|\mathbf{a}|} \times \mathbf{c} \right|, & \text{if the lines were parallel} \\ 0, & \text{if the lines intersected} \\ \frac{|\mathbf{c} \cdot (\mathbf{a} \times \mathbf{b}|)}{|\mathbf{a} \times \mathbf{b}|}, & \text{if the lines were skew} \end{cases} \tag{6.21}$$

$$d_{ax} = \begin{cases} 0, & \text{if the lines were parallel} \\ \frac{(\mathbf{c} \times \mathbf{b}) \cdot (\mathbf{a} \times \mathbf{b})}{|\mathbf{a} \times \mathbf{b}|^2}, & \text{if the lines intersected} \\ \frac{(\hat{\mathbf{a}} \cdot \hat{\mathbf{b}})(\hat{\mathbf{b}} \cdot \mathbf{c}) + (\hat{\mathbf{a}} \cdot \mathbf{c})(\hat{\mathbf{b}} \cdot \hat{\mathbf{b}})}{(\hat{\mathbf{a}} \cdot \hat{\mathbf{b}})^2 - (\hat{\mathbf{a}} \cdot \hat{\mathbf{a}})(\hat{\mathbf{a}} \cdot \hat{\mathbf{b}})}, & \text{if the lines were skew} \end{cases} \tag{6.22}$$

where $\hat{\mathbf{a}}, \hat{\mathbf{b}}, \hat{\mathbf{c}}$ are unit vectors of $\mathbf{a}, \mathbf{b}, \mathbf{c}$, respectively.

In the multi-label classification, the imbalance in the dataset was evaluated in each class using (Zhang et al. 2015):

$$ImR_i = \frac{\max(\mid \mathcal{D}_i^+ \mid, \mid \mathcal{D}_i^- \mid)}{\min(\mid \mathcal{D}_i^+ \mid, \mid \mathcal{D}_i^- \mid)} \tag{6.23}$$

where $ImR_i$ is the imbalance ratio of class $i$, $\mid \mathcal{D}_i^+ \mid$ is the total number of relevant values (the value of the class is 1) of class $i$, and $\mid \mathcal{D}_i^- \mid$ is the total number of irrelevant values (the value of the class is 0) of class $i$ in the training data sets. The average imbalance ratio ($ImR$) is:

$$ImR = \frac{1}{q} \sum_{i=1}^{q} ImR_i \tag{6.24}$$

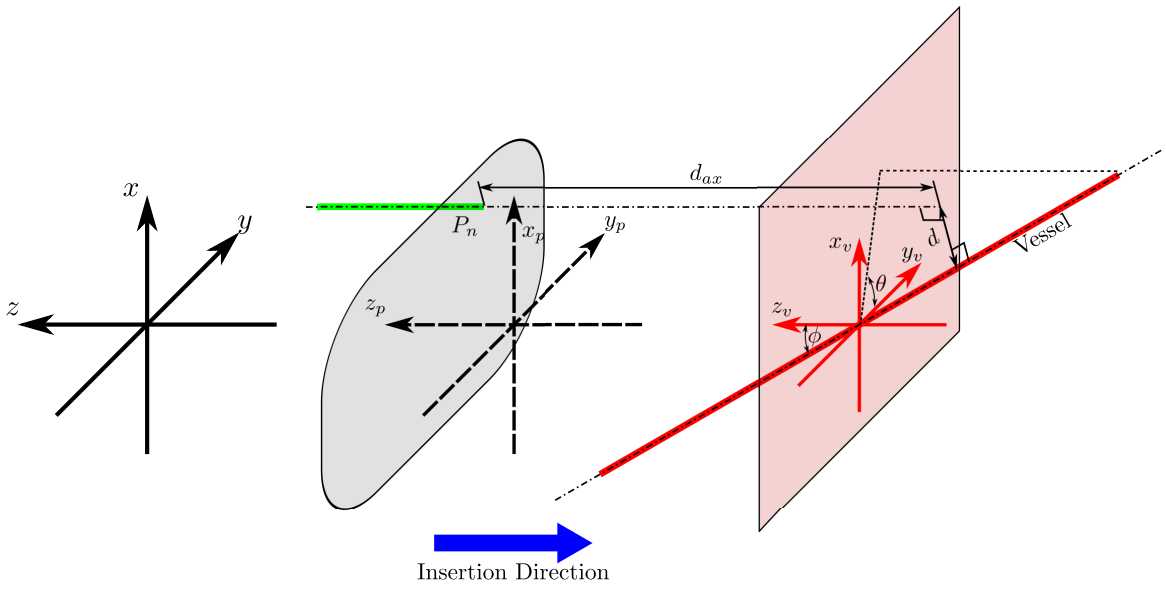


**Figure 6.10:** Three-dimensional representation of a vessel (red line). The vessel was defined in the vessel coordinate system $(x_v, y_v, z_v)$ with an angle of $\phi$ with respect to the $z_v$-axis. The projection of the vessel onto the $x_v y_v$-plane has an angle of $\theta$. The vessel coordinate system was located randomly in the global coordinate system $(x, y, z)$. Probe $n$ $(P_n)$ is represented as a green line in the figure. The probe was located in a fixed position with respect to the probe coordinate system $(x_p, y_p, z_p)$. During insertion, the probe coordinate system was moved along the $z$-axis. At the beginning of the insertion, the probe coordinate system was located at $x = 0, y = 0, z = 0$. Measures for the axial $(d_{ax})$ and off-axis $(d)$ distances were computed using the line to line distance

where $q$ is the total number of classes. Usually the number of relevant values in the data sets is less than the number of irrelevant values. During training, the cost of misclassification of relevant values $(C)$ was increased by:

$$C = (ImR)^{\gamma_m} \tag{6.25}$$

where, as described in section 6.2.1, $\gamma_m \in [0, 1]$ is a trade-off parameter.

As in the previous section, the trained network was evaluated using precision, recall, the $F_1$-score, and Hamming loss. The Hamming loss evaluates the fraction of misclassified prediction-label pairs (Zhang & Zhou 2014). Since Hamming loss is a loss function, the lower the hamming loss, the better the network performance. Since the detection area in Figure 6.9 was based on the maximum detection area for a 0.9 mm in diameter vessel, the evaluation was only conducted if there was enough information from the perfusion value to define the "no-go" area of the vessel (i.e. the perfusion value from at least one of the four probes was not in the no-detection state).

The trained network was then used to predict the "no-go" area for real insertion experiments. In the experiments, a vessel phantom with a 0.6 mm diameter and flow velocity rate of 20 mm/s, was used. In the needle coordinate system, the vessel is at $\phi = 90°$ and $\theta = 0°$. Vessel orientation was then transformed into the probe coordinate system. Details for the experiments are those previously described in Chapter 5.3.

### 6.3.2 Results

As described in section 6.2.2, the value of $\gamma_m$ was increased from 0 to 1 with 0.1 increments. Figure 6.11 shows the comparison of evaluation metrics (precision, recall, $F_1$-score, and hamming loss) as a function of $\gamma_m$, with $ImR = 89.7$. The best $F_1$-score (0.55) was obtained for $\gamma_m = 0.3$, while the best hamming loss (0.024) was obtained for $\gamma_m = 0.2$. At $\gamma_m = 0.4$, the $F_1$-score decreased to 0.52, while the hamming loss became 0.038. However, its recall value was more than 10% higher compared to the recall value for $\gamma_m = 0.3$. Since recall is related to the ability to correctly predict the positive value (a high risk region), the network that was trained using $\gamma_m = 0.4$ despite this value not providing the best hamming loss or $F_1$-score. In the test data sets generated from the simulation, the precision, recall, $F_1$-score and hamming loss of the network were found to be:

- Precision: 0.43
- Recall: 0.78
- $F_1$-score: 0.56
- Hamming loss: 0.035

Figure 6.12 shows an example of the network's ability to predict the presence and pose of a vessel that was not in a plane perpendicular to the needle insertion axis. The vessel coordinate system was located at $x = 0, y = 0.8, z = -1.8$. The orientation of the vessel was set at $\theta = 120°$ and $\phi = 75°$. The successive perfusion values ($A_1$ to $E_1$in Figure 6.12a) were generated using simulation by moving the probe coordinate system from $z = 0$ to $z = -1.5$ in -0.3 mm

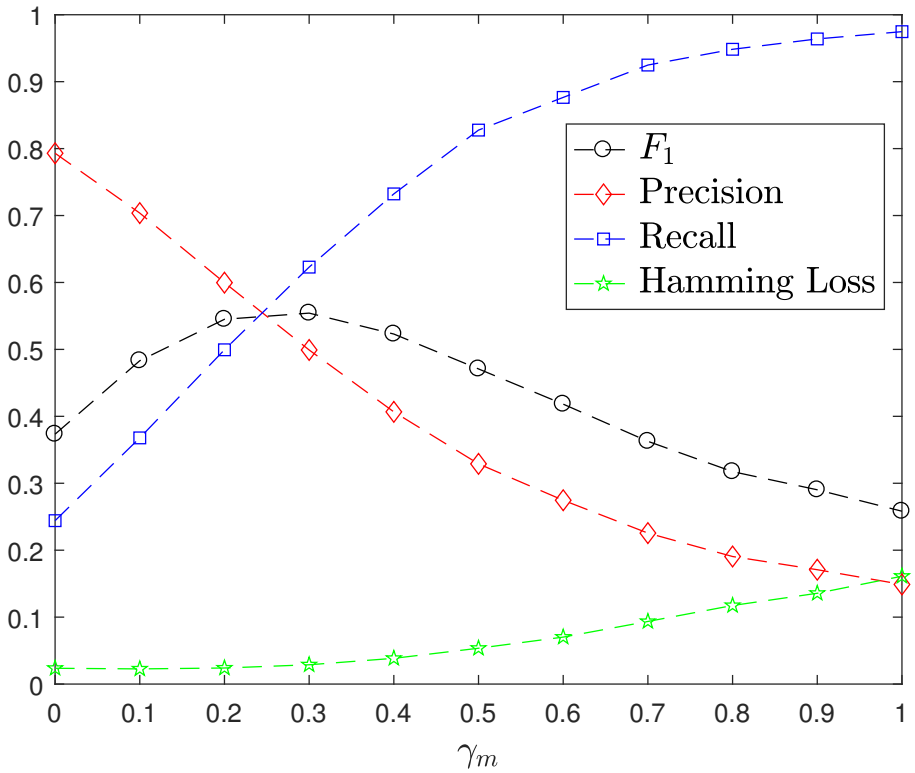


**Figure 6.11:** Multilabel network performance evaluation using $F_1$, Precision, Recall, and Hamming Loss as a function of $\gamma$

decrements. The blue area in Figure 6.12b shows voxels that were predicted to be occupied by the vessel. The red circles in Figure 6.12b represent actual voxels occupied by the vessel. To ease comparison, the voxels were projected in the $x_p y_p$-plane (Figure 6.12b top) and $x_p z_p$-plane (Figure 6.12b bottom). Starting from Point $C_1$, the network predicted the vessel orientation and position accurately.

The network was then used to predict the "no-go" area based on data from real insertion experiments. In total, there were 40 insertion experiments with each experiment consisting of seven forward insertion sequences (total number of samples: 280). Figure 6.13a shows the the perfusion values for the four probes while the probes were advancing toward the vessel at seven example positions ($A_0$ - $G_0$). The vessel was located at $z = -2.25, x = 0, y = -0.2$ mm. The red circles represent voxels where the vessel was located, while the blue squares highlight voxels predicted to contain the vessel. At the beginning of the measurements (Point $A_0$), the vessel was inside the detection volume of the sensor; however, the network did not predict this. As explained in section 6.3.1, the reason for the missed detection relates to the fact that the

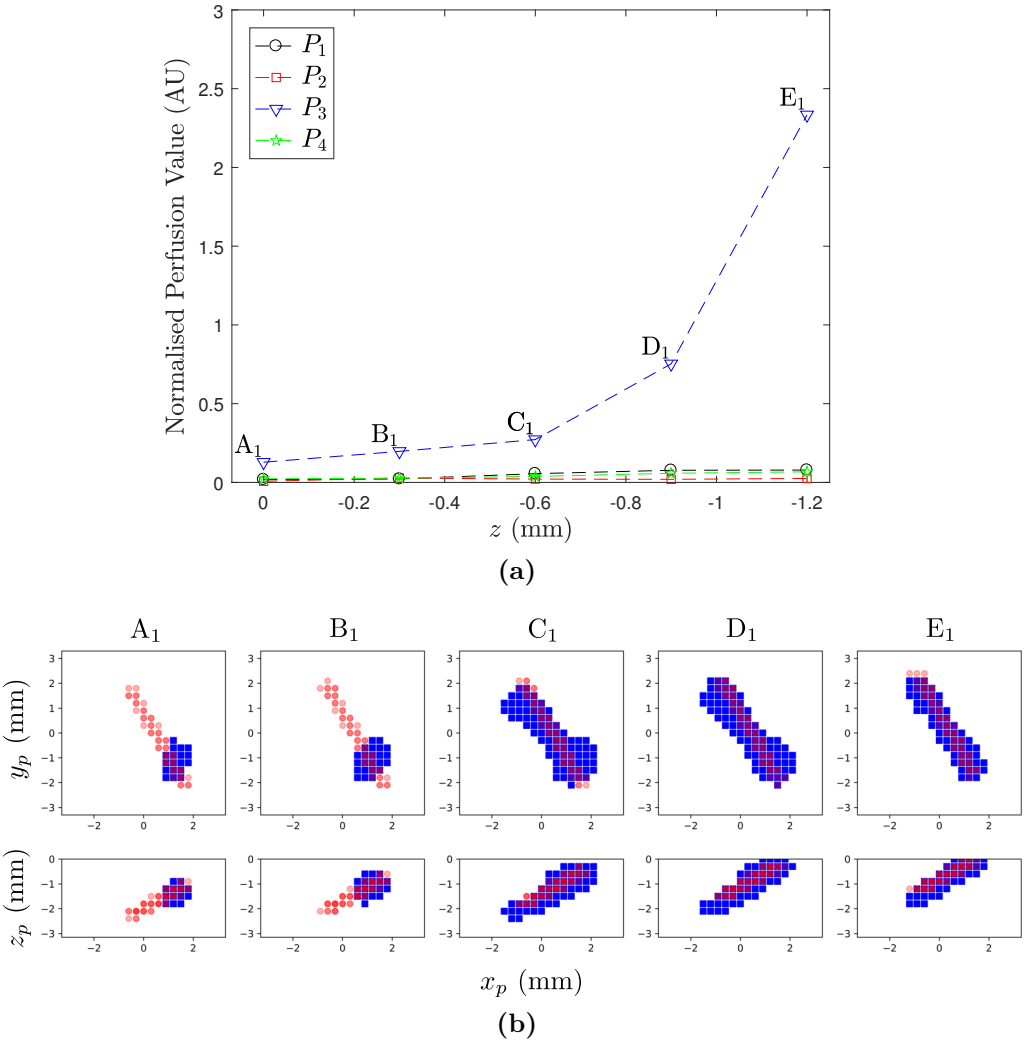


**Figure 6.12:** a) An example of simulated perfusion values for a vessel located at $x = 0, y = 0.8, z = -1.8$, with $\theta = 120°$ and $\phi = 75°$; b) Projection of the actual (red-circles) and predicted (blue-squares) vessel area inside the detection area of the sensors on the $x_p y_p$-plane (top) and on the $x_p z_p$-plane (bottom), with its corresponding perfusion values (Point $A_1$ - $E_1$)

detection volume of the sensor was defined with the maximum detection range for a 0.9 mm vessel. At Point $A_0$, the vessel location was still out of the the detection range of the probes for a 0.6 mm in diameter vessel. Prediction of the vessel pose, however, is shown to improve with each successive measurement, where, at the end of the insertion (Point $G_0$), the entire vessel volume is correctly predicted. The prediction evaluation metrics for the experiments were found to be:

- Precision: 0.21
- Recall: 0.54

- $F_1$-score: 0.30

- Hamming loss: 0.078

It should be noted that, if the evaluation metrics were performed only at Point $G_0$, the recall value increased to 0.77, which means a 77% prediction accuracy in the vessel volume at Point $G_0$.

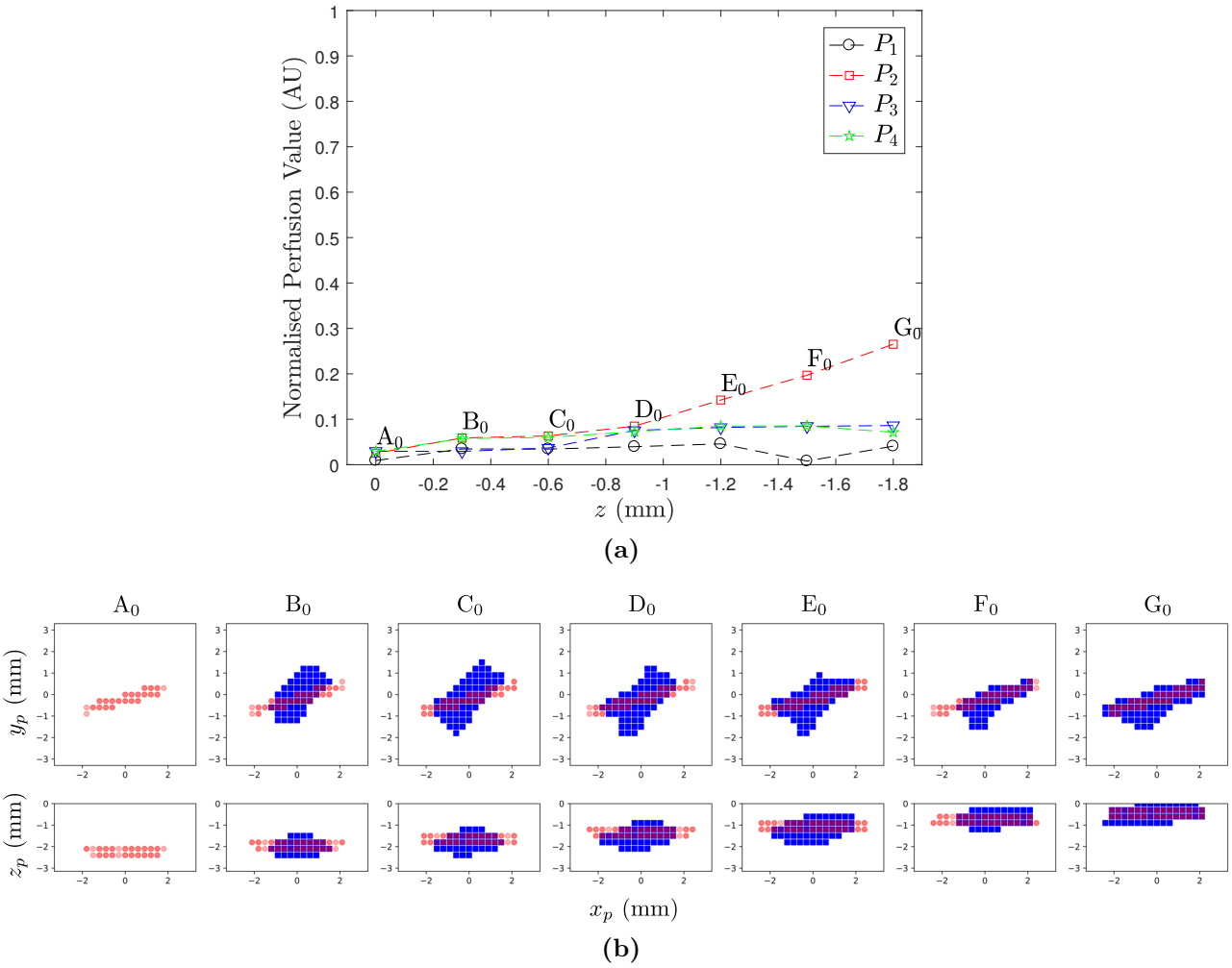


**Figure 6.13:** a) Example perfusion values from the insertion experiments. The measurements were taken while the needle was located at $z = 0$ to $z = -1.8$, in $-0.3$ decrements; b) Projection of the actual (red-circles) and predicted (blue-squares) vessel area inside the detection area of the sensors on the $x_p y_p$-plane (top) and on the $x_p z_p$-plane (bottom), with its corresponding perfusion values (Point $A_0$ - $G_0$)

## 6.4 Discussion

In section 6.2, an LSTM network was used to predict a vessel diameter and position based on successive measurements from a single probe. The confusion matrix in Table 6.2 shows that, in addition to false negatives, there was vessel diameter misclassification as well. The diameter misclassification was predominantly between two classes with a small diameter difference. The misclassification of vessels with a diameter of 0.6 mm into a 0.9 mm diameter vessel, however, was higher compared to misclassification into a 0.3 mm diameter vessel. The reason for this may be because of the probe's detection range for a 0.6 mm in diameter vessel being closer to the probe's detection range for a vessel which is 0.9 mm in diameter (Figure 6.3). It should be noted that, here, all vessel diameters were assumed to have the same range of flow velocity rates (10 - 20 mm/s). In future work, the flow velocity range for each vessel diameter could be assigned a different set of values (Piechnik et al. 2008) that should be easier for the network to discriminate.

The results of section 6.2 can be used in conjunction with the algorithm developed in Chapter 4. The vessel diameter and positions can be applied directly to define the vessel pose based on the circle-circle tangent of two or more probes. Moreover, it is not limited to a given pair of tissue and vessel properties and information about the vessel diameter and position can be added to the no-go area information generated using the algorithm developed in Chapter 5.

Even though it is possible to incorporate the prediction achieved with a single probe into the algorithms presented in previous chapters, the assumption that the vessel is in a plane perpendicular to the needle insertion axis might limit its applicability. Therefore, in section 6.3, another LSTM network was trained to predict the vessel pose directly. As can be seen in Figure 6.13, the prediction improves as the needle approaches vessel. This means that, in order to obtain more information about the vessel pose, the insertion may need to continue once a vessel is first detected. Since the prediction area provides information about the position of the vessel in the $z_p$-direction when the vessel is first detected (Point-$B_0$ in Figure 6.13), the maximum insertion length that is required to acquire more vessel information can be determined, as to avoid inadvertent vessel damage.

Figure 6.11 shows that the higher the recall value, the lower the precision value. Since penetrating a vessel during minimally invasive brain surgery can be fatal to the patient, a network with a higher recall value and worse hamming loss and $F_1$-score were chosen. Here, a binary relevance method was used for multi-label learning of an LSTM network, which shows good prediction results. However, binary relevance lacks any label correlation (Zhang et al. 2018). To incorporate label correlation, another network architecture that performs better with spatial and temporal data, such as convolutional LSTM network, might be used (Xingjian et al. 2015).

The goal of the vessel detection in a steerable needle system is to generate a "no-go" area in front of the needle. In section 6.3 the "no-go" area was defined while all of the segments were aligned. Since the PBN is steered by introducing an offset between segments, if the leading segment/s detects a vessel, all of the probes need to be aligned to predict the "no-go" area appropriately. The detection method in Chapter 6.3 can still be performed by storing the position information so that the perfusion measurements from each probe can be sorted according to position, but this could not be explored in the time available.

The results from section 6.2 and 6.3 show that the network can predict information about the vessel even though the optical properties of the tissue differ within a certain range ($\mu_s'$ : 0.75±0.2 $mm^{-1}$). If the optical properties range varies significantly, for example in the a grey matter phantom compared to a white matter phantom, the network may be unable to identify a generalisation. However, since the tissue greyness can be observed using a laser Doppler system based on the intensity of the detected light (Wårdell et al. 2016), light intensity could be added as a further network input to differentiate between white and grey matter.

Even though the networks were trained using simulation data, the results show that these can be used to predict experimental measurements correctly. Use of the simulation data sped up the training process for different probes and needle properties (e.g. LDF with a different wavelength, a different needle size, a different configuration of probe numbers and positions). Consequently, real insertion experiments can be performed in the evaluation stage only, resulting in significant time and effort gains. In this chapter, the vessel was assumed to be static. Previously, a high-resolution material tracking set-up based on Particle Image Velocimetry (PIV) was used to

investigate tool-tissue interactions (Leibinger et al. 2016). By combining this method with a vessel embedded within the sample, the movement of the vessel during insertion could be predicted. This movement prediction could then be applied in the simulation so that the LSTM network would take into account the effect of vessel movement.

## 6.5 Conclusion

In this chapter, LSTM networks have been used to predict the vessel diameter and position based on successive measurements of a single probe and to predict the vessel pose based on simultaneous measurements from four probes embedded in a 4 mm PBN. Single probe prediction could classify the vessel diameter for unknown vessel and tissue properties with an accuracy of 75%. For the correctly predicted diameter, the position could be accurately predicted with a sub-millimetre error (0.27 mm). The no-go area based on measurements from four probes also shows promising results. After several measurements, the network could predict the pose of the vessel, with an average 77% final overlap between actual and predicted vessel areas. Even though the LSTMs were trained using simulation data, these still perform well in predicting vessel pose from real experiments. In this chapter, the no-go volume in front of the needle captures the full information about the vessel's pose and diameter, showing a significant improvement over the algorithm developed in Chapter 5.

# Chapter 7

# Conclusion and Future Work

## 7.1 Conclusion

This thesis contributes to the field of steerable needles by improving their insertion safety via the development of a sensorisation system that enables the needle to detect the presence of a vessel which cannot otherwise be detected during preoperative imaging. A steerable needle system can follow curvilinear paths within a tissue to avoid anatomical obstacles or to rectify any target misalignment. A biologically inspired programmable bevel-tip needle (PBN) was developed in our group that was specifically designed to perform minimally invasive brain surgery. The multi-segment design of the needle allows the needle to steer in full three-dimensional space by exploiting asymmetric forces acting on the needle tip while changing its offset configuration. Avoiding haemorrhage is still a challenge in minimally invasive brain surgery, where several solutions have been proposed to be implemented in a rigid needle system. Even though a steerable needle system was designed to be able to avoid an obstacle, prior to this thesis, the presence of a vessel that is undetected in preoperative images had not been considered.

This thesis also has a contribution in the manufacturing strategy of the PBN. A PBN with a diameter of 2.5 mm was successfully manufactured using a metal 3D printer machine (Chapter 3.2). A manufacturing strategy was developed based on the manufacturing results of a benchmark part. The benchmark part had key parameters that needed to be optimised: build angle

and distance between support structures. By assessing the benchmark part instead of the real component, the manufacturing strategy was developed in a faster and more systematic way. Even though the metal PBN is too stiff to be used as a steerable needle, the building strategy developed in Chapter 3.2 can be implemented to build any high aspect ratio part.

Our subcontractor has successfully produced a 2.5 mm diameter PBN using a micro-extrusion process from a biocompatible polymer. Since the needle relies on tool-tissue interaction on its tip to steer, a consistent tip angle is required. Using a fixture that was manufactured by a resin-based 3D printer (Chapter 3.3), the bevel tip angle was produced accurately with a high consistency. Even though in Chapter 3.3 two bevel tip angles were produced (30° and 45°), since it was manufactured using a 3D printer, the fixture can be easily modified to produce any bevel tip angle. This flexibility is useful in the development of the PBN to find the optimum bevel tip angle.

To detect a vessel in front of the needle, the PBN sensorisation started with a feasibility study of embedding a forward-looking sensor within a segment (Chapter 4.2). The minimum requirement of the sensor detection range was defined based on the geometry of the 2.5 mm PBN. Since the sensor was located parallel but offset to the central needle axis, a laser Doppler flowmetry (LDF) system was chosen since it has a few millimetre off-axis detection range. An LDF system embedded in a rigid needle was used in the literature to detect a vessel during DBS implantation procedure (Wårdell et al. 2016). To fully optimise the capability of a steerable needle system to avoid an obstacle, the sensor should also give information about vessel pose. However, the perfusion value from the LDF system does not give any information about vessel pose and diameter. In this thesis, the investigation to deploy LDF sensors in the PBN resulted in three main findings.

Firstly, in Chapter 4.3, it was found that successive measurements of a single LDF probe, while the needle is advancing, can be used to infer the position of the vessel. Successive measurements were required since many vessel positions resulted in a certain perfusion value. In Chapter 4.3, the perfusion value was assigned to its corresponding positions using a look-up table. Even though the look-up table was only applicable for specific tissue and vessel properties, it gave

valuable insight into the development of the LSTM based vessel detection (Chapter 6.2). In Chapter 6.2, the LSTM network was able to predict the vessel position and diameter with a high accuracy (75% diameter prediction accuracy and 0.27 mm positional RMSE). These predictions were not limited to specific tissue and vessel properties. Even though the performance of the network was highly dependent on the dataset that was used to train the network, the use of simulation in generating the training dataset increased the flexibility to enrich it. Also, even though the network was trained using data from the simulation, Chapter 6.2.2 showed that the network was able to predict the vessel diameter and positions from real experimental data.

The second finding was the requirement to use multiple forward-looking sensors to obtain vessel pose information. This is because, in three-dimensional space, many vessel poses can have the same pair of off-axis and axial distances from the probe. Using the measurements of two LDF probes, Chapter 4.3 introduced the notion of using multiple LDF sensors to reduce the possibility of vessel pose ambiguity. The successive measurements were able to inform the off-axis and axial distance from the vessel to the probe. The off-axis distance was then used to generate a detection circle for each probe. Using an assumption that the vessel was in the perpendicular plane to the insertion axis, vessel poses were reduced to four, using tangent lines between these two detection circles.

In Chapter 4, four LDF sensors were used instead of two to classify the vessel pose. Using the same assumption as in Chapter 4.3 that the vessel was located in the plane perpendicular to the insertion axis, relative measurements from four probes were exploited to classify a "no-go" region in front of the needle (Chapter 5.3). Cross-talk between probes was observed during the characterisation. Since it was difficult to model the cross-talk between these, the measurements were performed by switching the channels one by one. Relative measurements acted like a normalisation so that the classification could be performed for any set of tissue optical properties. Since it relied on relative measurements, each channel was calibrated using motility standard beforehand. The results in Section 5.3 showed that the relative measurements had a very high accuracy in predicting vessel poses (2° angular RMSE and 0.1 mm position RMSE). However, the algorithm developed in Chapter 5 did not provide information about vessel axial distance and vessel diameter.

Chapter 6.3 implemented an LSTM network to define a "no-go" area from successive measurements of four probes. Unlike vessel pose prediction in Chapter 4 and 5, the use of the LSTM network enabled the assumption that the vessel is in a perpendicular plane with the insertion axis to be eliminated. Releasing this assumption increased the applicability of the algorithm in real world scenarios. Similar to Chapter 6.2, the LSTM network in Chapter 6.3 was trained using a dataset generated by simulation. Even though the network did not explicitly give the vessel diameter information and the vessel pose angle and position, it directly gave the area that must not be penetrated by the needle. Evaluation of the network using simulation data gave 73% recall value. Meanwhile, using the data from the real experiment, at the end of the insertion, the network gave 76% recall value. This means that, in the real experiment's data, 76% of the vessel volume was correctly predicted by the network. The results in Chapter 6.3 suggest that a network with a higher recall value can be achieved by setting a higher weight in predicting the positive value. The increase in recall value, however, will also increase false positives.

The third finding was the effect of using a constant insertion speed on the perfusion value measurement of an LDF sensor. During insertion, the tissue in front of the needle tip was displaced. This tissue displacement increased the background perfusion value of the LDF system (Chapter 5.2). Using a robotic system to perform the insertion, a constant insertion speed resulted in a constant background perfusion value. The experiments in the grey matter phantom showed that the faster the insertion speed, the higher the background perfusion value. Using 0.2 mm/s insertion speed, experiments described in Chapter 5.2 demonstrated that the vessel in front of the probe could still be predicted by observing the monotonically increasing perfusion value. The use of continuous insertion instead of incremental insertion, as in Wårdell et al. (2016), could reduce the time to perform the surgical procedure.

In addition, the sensorisation method developed here can be applied to other steerable needle systems. The concept of using forward-looking sensors in a steerable needle can increase the safety of steerable needle insertion in general. Also, the successive measurements combined with multiple forward-looking sensors to get vessel pose information are not limited in the use of a Laser Doppler flowmetry system. This concept may be translated into other laser-based

systems that lack quantitative data from the vessel, such as remission spectroscopy (Markwardt et al. 2017) and CGD (Liang et al. 2013).

## 7.2 Limitations and Future Work

There are several limitations to the research presented in this thesis. These limitations and future work are discussed in this section.

The blood flow velocity rate was set at a constant value during the experiments. However, there are cardiovascular oscillations such as heartbeat, respiration, and Mayer waves that affect the blood flow velocity rate (Yücel et al. 2016). These oscillations frequencies are ranging from 0.0095 Hz to 2 Hz (Kvernmo et al. 1998). To achieve a more realistic vessel phantom, these oscillations could be mimicked during the experiments using a programmable syringe pump. The change in the blood flow velocity rate could also be simulated to generate the training dataset for the LSTM network so that the model could take into account these oscillations.

All of the experiments were performed in a controlled environment using tissue phantoms. As future work, experiments can be performed in *ex-vivo* brain tissue while still using the vessel phantom. The vessel phantom that was used during the experiments had a reduced scattering coefficient of 1.8 $mm^{-1}$ that was close to the scattering coefficient of human blood (Friebel et al. 2006). However, the absorption coefficient of the blood vessel phantom ($\mu_a$: 0.015 $mm^{-1}$) was less than the absorption coefficient of human blood ($\approx$ 0.3 $mm^{-1}$). To increased $\mu_a$, India ink could be added into the phantom (Flock et al. 1992). Experiments could also be performed using human blood if required.

During the insertion experiments in Chapter 5 the 4 mm PBN was used instead of the 2.5 mm PBN. The reason for using the 4 mm PBN was due to the size limitation of the commercially available LDF probe. In the setup presented in this thesis, the LDF probe consisted of two optical fibres, each of which with a 0.3 mm diameter. Up to 60 mm from the tip of the probe, the cladding of each fibre was stripped, which reduced its diameter to 0.15 mm. The total diameter of the probe tip was 0.3 mm while the diameter of the rest of the probe was 0.6

mm. Since stripping the cladding can be performed accurately only at a certain length (60 mm for example), the current sensor is not suitable to be embedded in the 2.5 mm diameter PBN that has a 0.3 mm diameter working channel. The cladding removal also results in a more brittle fibre that is easily broken. In future work, a collaboration with the LDF manufacturer (Oxford Optronix ltd., Abingdon, Oxford, UK) will be established to produce a probe with a smaller diameter (e.g. using optical fibres with a diameter of 0.125 mm to build the probe (FIP100110125, CM Scientific, Silsden UK)).

The maximum off-axis detection range for the current LDF probe was 2.5 mm for a 0.9 mm vessel diameter at a flow velocity rate of 20 mm/s (Chapter 6). The detection range of the LDF probe increases with an increase of the separation distance between fibres (Larsson et al. 2002). Larsson et al. (2002) also showed that the lower the reduced scattering coefficient or absorption coefficient, the deeper the detection range of the sensor. In the wavelength range of 670 nm - 1064 nm, the reduced scattering coefficient of the human grey and white matter decreases with the increase in the wavelength (Yaroslavsky et al. 2002). Since the fibre separation distance is constrained by the diameter of the working channel, a longer wavelength can be used to improve the probe detection range.

The laser Doppler monitor that was used has a maximum dynamic range of 20 mm/s, as can be seen in the results of Chapter 5.2. An artery with a diameter of $\approx 1$ mm could have a flow velocity of up to 150 mm/s (Piechnik et al. 2008). This flow velocity is much higher than the dynamic limit of the LDF monitor. Therefore, the development of an LDF monitor that has a higher dynamic range is required. A higher dynamic range can be achieved by using a higher data acquisition rate (Liang et al. 2013). Liang et al. (2013) calculated that using a 1,300 nm wavelength with a 400 kHz sampling rate could increase the maximum Doppler velocity detection range to 130 mm/s.

To avoid the cross-talk between each probe while recording the perfusion value in front of the needle, measurements were conducted by activating each channel in turn. Currently, the switching was performed manually. Therefore, a four-channel system with the ability to switch the readings from each channel to avoid inter-channel cross-talk should be developed. Also, a

digital communication interface to enable two-way data exchange between the Doppler system and needle controller is required. The switching strategy could also be developed so that the switching is only performed by activating the illumination lights in turn, while all the detectors are always active. Using this switching strategy, the illumination light from one probe could be detected by all four detectors. Since the distance between each detection fibre to the illumination fibre is different, depth discrimination could be performed (Liebert et al. 1998).

During the perfusion value simulations, the vessel was simulated in a plane perpendicular to the sensor axis due to software limitations. In the experiments, the vessel was located at a 5° angle with respect to the perpendicular plane. Nonetheless, the comparison between the experimental values and simulation values showed good agreement. Therefore, in Chapter 6, it was assumed that the simulated perfusion value for a probe was only a function of axial and off-axis distance (equation 6.22 and 6.21). To investigate the accuracy of this assumption, experiments might be performed to measure the perfusion value for a vessel with a high tilt angle.

Total light intensity (TLI) in the detector can be used to determine tissue greyness. Therefore, it can be used to define whether the probe is inside grey matter or white matter (Wårdell et al. 2016). In this thesis, the TLI data from the LDF system have not been used in conjunction with the perfusion value measurements. Also, even though dynamic characterisation was investigated in Chapter 5.2, the increase of background perfusion value was not implemented in the LSTM network developed in 6. PIV measurements can be used to investigate the velocity distribution in front of the needle (Leibinger et al. 2016). Using Monte-Carlo simulation, these velocity distributions can be used to model the effect of the insertion speed on the background perfusion value. During the study in this thesis, it was assumed that the vessel was static. The PIV measurements could also be used to investigate the movement of the vessel during needle insertion. As future work, TLI measurements, background perfusion value addition, and vessel movement could be taken into account while developing the LSTM network.

Finally, the high-risk area that was predicted using the LSTM network developed in Chapter 6.3

was not used to update the obstacle map in the global coordinate system. Therefore, a method to update the obstacle map in the global coordinate system and subsequent development of a suitable obstacle avoidance algorithm would need to be investigated. Also, the network only used the input from successive perfusion values and movement directions without using any information about the voxel state from pre-operative images and the updated voxel states from the measurements. To incorporate this information, a network that can capture spatiotemporal information, such as a Convolution-LSTM (Xingjian et al. 2015), could be adopted.

# Bibliography

Abayazid, M., Kemp, M. & Misra, S. (2013), 3d flexible needle steering in soft-tissue phantoms using fiber bragg grating sensors, *in* 'Robotics and Automation (ICRA), 2013 IEEE International Conference on', IEEE, pp. 5843–5849.

Abayazid, M., Moreira, P., Shahriari, N., Patil, S., Alterovitz, R. & Misra, S. (2015), 'Ultrasound-guided three-dimensional needle steering in biological tissue with curved surfaces', *Medical Engineering and Physics* **37**(1), 145–150.

Abayazid, M., Pacchierotti, C., Moreira, P., Alterovitz, R., Prattichizzo, D. & Misra, S. (2016), 'Experimental evaluation of co-manipulated ultrasound-guided flexible needle steering', *The International Journal of Medical Robotics and Computer Assisted Surgery* **12**(2), 219–230.

Abayazid, M., Roesthuis, R. J., Reilink, R. & Misra, S. (2013), 'Integrating deflection models and image feedback for real-time flexible needle steering', *IEEE Transactions on Robotics* **29**(2), 542–553.

Abayazid, M., Vrooijink, G. J., Patil, S., Alterovitz, R. & Misra, S. (2014), 'Experimental evaluation of ultrasound-guided 3d needle steering in biological tissue', *International journal of computer assisted radiology and surgery* **9**(6), 931–939.

Abdel Ghany, K. & Moustafa, S. (2006), 'Comparison between the products of four rpm systems for metals', *Rapid Prototyping Journal* **12**(2), 86–94.

Abolhassani, N., Patel, R. & Moallem, M. (2007), 'Needle insertion into soft tissue: A survey', *Medical engineering & physics* **29**(4), 413–431.

Abolhassani, N., Patel, R. V. & Ayazi, F. (2007), 'Minimization of needle deflection in robot-assisted percutaneous therapy', *The international journal of medical Robotics and computer assisted surgery* **3**(2), 140–148.

Adebar, T. K., Fletcher, A. E. & Okamura, A. M. (2014), '3-d ultrasound-guided robotic needle steering in biological tissue', *IEEE Transactions on Biomedical Engineering* **61**(12), 2899–2910.

Adebar, T. K., Greer, J. D., Laeseke, P. F., Hwang, G. L. & Okamura, A. M. (2016), 'Methods for improving the curvature of steerable needles in biological tissue', *IEEE Transactions on Biomedical Engineering* **63**(6), 1167–1177.

Akarçay, H. G., Preisser, S., Frenz, M. & Rička, J. (2012), 'Determining the optical properties of a gelatin-tio 2 phantom at 780 nm', *Biomedical optics express* **3**(3), 418–434.

Allouch, H., Pfeifenbring, S., Behnke-Mursch, J., Halatsch, M.-E. & Mursch, K. (2014), 'Real-time ultrasound monitoring during intracranial needle biopsies: operative results and detection of complications in 100 cases', *World neurosurgery* **82**(1), 202–206.

Antonio-Lopez, J. E., Eznaveh, Z. S., LiKamWa, P., Schülzgen, A. & Amezcua-Correa, R. (2014), 'Multicore fiber sensor for high-temperature applications up to 1000 c', *Optics letters* **39**(15), 4309–4312.

Ayvali, E. & Desai, J. P. (2015), 'Optical flow-based tracking of needles and needle-tip localization using circular hough transform in ultrasound images', *Annals of biomedical engineering* **43**(8), 1828–1840.

Ayvali, E., Liang, C.-P., Ho, M., Chen, Y. & Desai, J. P. (2012), 'Towards a discretely actuated steerable cannula for diagnostic and therapeutic procedures', *The International journal of robotics research* **31**(5), 588–603.

Barua, N. U., Gill, S. S. & Love, S. (2014), 'Convection-enhanced drug delivery to the brain: Therapeutic potential and neuropathological considerations', *Brain pathology* **24**(2), 117–127.

Bériault, S. et al. (2014), 'Neuronavigation using susceptibility-weighted venography: application to deep brain stimulation and comparison with gadolinium contrast', *Journal of neurosurgery* **121**(1), 131–141.

Bernardes, M., Adorno, B. V., Poignet, P. & Borges, G. (2013), 'Robot-assisted automatic insertion of steerable needles with closed-loop imaging feedback and intraoperative trajectory replanning', *Mechatronics* **23**(6), 630–645.

Binder, D. K., Rau, G. & Starr, P. A. (2003), 'Hemorrhagic complications of microelectrode-guided deep brain stimulation', *Stereotactic and functional neurosurgery* **80**(1-4), 28–31.

Bui, V. K., Park, S., Park, J.-O. & Ko, S. Y. (2016), 'A novel curvature-controllable steerable needle for percutaneous intervention', *Proceedings of the Institution of Mechanical Engineers, Part H: Journal of Engineering in Medicine* **230**(8), 727–738.

Burrows, C., Liu, F., Leibinger, A., Secoli, R. & Rodriguez, y. B. F. (2017), Multi-target planar needle steering with a bio-inspired needle design, SPRINGER INT PUBLISHING AG, pp. 51–60.

Burrows, C., Secoli, R. & y Baena, F. R. (2013), Experimental characterisation of a biologically inspired 3d steering needle, *in* '2013 13th International Conference on Control, Automation and Systems (ICCAS)', IEEE, pp. 1252–1257.

Byun, H.-S. & Lee, K. H. (2003), Design of a new test part for benchmarking the accuracy and surface finish of rapid prototyping processes, *in* 'International Conference on Computational Science and Its Applications', Springer, pp. 731–740.

Carr, K. & Ferreira, P. (1995), 'Verification of form tolerances part ii: cylindricity and straightness of a median line', *Precision Engineering* **17**(2), 144–156.

Carriere, J., Khadem, M., Rossa, C., Usmani, N., Sloboda, R. & Tavakoli, M. (2018), 'Surgeon-in-the-loop 3-d needle steering through ultrasound-guided feedback control', *IEEE Robotics and Automation Letters* **3**(1), 469–476.

Castillo, L. (2005), 'Study about the rapid manufacturing of complex parts of stainless steel and titanium', *TNO report with the collaboration of AIMME* .

Cerkvenik, U., van de Straat, B., Gussekloo, S. W. & van Leeuwen, J. L. (2017), 'Mechanisms of ovipositor insertion and steering of a parasitic wasp', *Proceedings of the National Academy of Sciences* **114**(37), E7822–E7831.

Chevrie, J., Shahriari, N., Babel, M., Krupa, A. & Misra, S. (2018), 'Flexible needle steering in moving biological tissue with motion compensation using ultrasound and force feedback', *IEEE Robotics and automation letters* .

Cioboata, D., Palade, D., Abalaru, A., Stanciu, D., Savu, L., Logofatu, C. & Traistaru, F. (2012), 'Considerations regarding evaluation of the accuracy assessment of the roundness', *The Scientific Bulletin of Valahia University–Materials and Mechanics.* **7**, 74–80.

De Benedictis, A., Trezza, A., Carai, A., Genovese, E., Procaccini, E., Messina, R., Randi, F., Cossu, S., Esposito, G., Palma, P. et al. (2017), 'Robot-assisted procedures in pediatric neurosurgery', *Neurosurgical focus* **42**(5), E7.

de Mul, F. (2004), *Monte Carlo simulation of Light transport in Turbid Media*, pp. 465–533.

de Mul, F. d., Koelink, M., Kok, M., Harmsma, P., Greve, J., Graaff, R. & Aarnoudse, J. (1995), 'Laser doppler velocimetry and monte carlo simulations on models for blood perfusion in tissue', *Applied optics* **34**(28), 6595–6611.

DiLuca, M. & Olesen, J. (2014), 'The cost of brain diseases: a burden or a challenge?', *Neuron* **82**(6), 1205–1208.

DiMaio, S. P. & Salcudean, S. (2003), Needle steering and model-based trajectory planning, *in* 'International Conference on Medical Image Computing and Computer-Assisted Intervention', Springer, pp. 33–40.

Dupont, P. E., Lock, J., Itkowitz, B. & Butler, E. (2010), 'Design and control of concentric-tube robots', *IEEE Transactions on Robotics* **26**(2), 209–225.

Engh, J. A., Podnar, G., Khoo, S. Y. & Riviere, C. (2006), Flexible needle steering system for percutaneous access to deep zones of the brain, *in* 'Bioengineering Conference, 2006. Proceedings of the IEEE 32nd Annual Northeast', IEEE, pp. 103–104.

Engh, J. A., Podnar, G., Kondziolka, D. & Riviere, C. N. (2006), Toward effective needle steering in brain tissue, *in* 'Engineering in Medicine and Biology Society, 2006. EMBS'06. 28th Annual International Conference of the IEEE', IEEE, pp. 559–562.

Fahad, M. & Hopkinson, N. (2012), A new benchmarking part for evaluating the accuracy and repeatability of additive manufacturing (am) processes, *in* '2nd International Conference on Mechanical, Production and Automobile Engineering (ICMPAE 2012), Singapore, Apr', pp. 28–29.

Fallahi, B., Rossa, C., Sloboda, R. S., Usmani, N. & Tavakoli, M. (2017), 'Sliding-based image-guided 3d needle steering in soft tissue', *Control Engineering Practice* **63**, 34–43.

Fenoy, A. J. & Simpson Jr, R. K. (2014), 'Risks of common complications in deep brain stimulation surgery: management and avoidance', *Journal of neurosurgery* **120**(1), 132–139.

Field, M., Witham, T. F., Flickinger, J. C., Kondziolka, D. & Lunsford, L. D. (2001), 'Comprehensive assessment of hemorrhage risks and outcomes after stereotactic brain biopsy', *Journal of neurosurgery* **94**(4), 545–551.

Flock, S. T., Jacques, S. L., Wilson, B. C., Star, W. M. & van Gemert, M. J. (1992), 'Optical properties of intralipid: a phantom medium for light propagation studies', *Lasers in surgery and medicine* **12**(5), 510–519.

Franceschini, G. (2006), The mechanics of human brain tissue, PhD thesis, University of Trento.

Frasson, L., Ferroni, F., Ko, S. Y., Dogangil, G. & y Baena, F. R. (2012), 'Experimental evaluation of a novel steerable probe with a programmable bevel tip inspired by nature', *Journal of robotic surgery* **6**(3), 189–197.

Frasson, L., Parittotokkaporn, T., Schneider, A., Davies, B., Vincent, J., Huq, S., Degenaar, P. & Baena, F. R. (2008), Biologically inspired microtexturing: Investigation into the sur-

face topography of next-generation neurosurgical probes, *in* '2008 30th Annual International Conference of the IEEE Engineering in Medicine and Biology Society', IEEE, pp. 5611–5614.

Fredriksson, I. (2009), Quantitative laser Doppler flowmetry, PhD thesis, Linköping University Electronic Press.

Fredriksson, I., Fors, C. & Johansson, J. (2007), 'Laser doppler flowmetry-a theoretical framework', *Department of Biomedical Engineering, Linköping University* pp. 6–7.

Fredriksson, I., Larsson, M. & Strömberg, T. (2009), 'Measurement depth and volume in laser doppler flowmetry', *Microvascular research* **78**(1), 4–13.

Fredriksson, I., Larsson, M. & Strömberg, T. (2010), 'Model-based quantitative laser doppler flowmetry in skin', *Journal of biomedical optics* **15**(5), 057002–057002.

Friebel, M., Roggan, A., Müller, G. J. & Meinke, M. C. (2006), 'Determination of optical properties of human blood in the spectral range 250 to 1100 nm using monte carlo simulations with hematocrit-dependent effective scattering phase functions', *Journal of biomedical optics* **11**(3), 034021.

Fuchs, K. (2002), 'Minimally invasive surgery', *Endoscopy* **34**(02), 154–159.

Garriga-Casanovas, A. & Rodriguez y Baena, F. (2018), 'Complete follow-the-leader kinematics using concentric tube robots', *The International Journal of Robotics Research* **37**(1), 197–222.

Gerard, I. J. et al. (2017), 'Brain shift in neuronavigation of brain tumors: A review', *Medical image analysis* **35**, 403–420.

Gerboni, G., Greer, J. D., Laeseke, P. F., Hwang, G. L. & Okamura, A. M. (2017), 'Highly articulated robotic needle achieves distributed ablation of liver tissue', *IEEE robotics and automation letters* **2**(3), 1367–1374.

Gilbert, H. B. & Webster, R. J. (2013), Can concentric tube robots follow the leader?, *in* '2013 IEEE International Conference on Robotics and Automation (ICRA)', IEEE, pp. 4881–4887.

Gillams, A. (2005), 'Image guided tumour ablation', *Cancer Imaging* **5**(1), 103.

Glozman, D. & Shoham, M. (2007), 'Image-guided robotic flexible needle steering', *IEEE Transactions on Robotics* **23**(3), 459–467.

Göbel, W., Brucker, D., Kienast, Y., Johansson, A., Kniebühler, G., Rühm, A., Eigenbrod, S., Fischer, S., Goetz, M., Kreth, F.-W. et al. (2012), 'Optical needle endoscope for safe and precise stereotactically guided biopsy sampling in neurosurgery', *Optics express* **20**(24), 26117–26126.

Goldberg, S. N., Grassi, C. J., Cardella, J. F., Charboneau, J. W., Dodd, G. D., Dupuy, D. E., Gervais, D., Gillams, A. R., Kane, R. A., Lee Jr, F. T. et al. (2005), 'Image-guided tumor ablation: standardization of terminology and reporting criteria', *Radiology* **235**(3), 728–739.

Goyette, A., Pichette, J., Tremblay, M.-A., Laurence, A., Jermyn, M., Mok, K., Paulsen, K. D., Roberts, D. W., Petrecca, K., Wilson, B. C. et al. (2015), 'Sub-diffuse interstitial optical tomography to improve the safety of brain needle biopsies: a proof-of-concept study', *Optics letters* **40**(2), 170–173.

Greff, K., Srivastava, R. K., Koutník, J., Steunebrink, B. R. & Schmidhuber, J. (2017), 'Lstm: A search space odyssey', *IEEE transactions on neural networks and learning systems* **28**(10), 2222–2232.

Haj-Hosseini, N., Richter, J. C., Milos, P., Hallbeck, M. & Wårdell, K. (2018), '5-ala fluorescence and laser doppler flowmetry for guidance in a stereotactic brain tumor biopsy', *Biomedical optics express* **9**(5), 2284–2296.

Hall, W. A. (1998), 'The safety and efficacy of stereotactic biopsy for intracranial lesions', *Cancer: Interdisciplinary International Journal of the American Cancer Society* **82**(9), 1749–1755.

*Handbook of optical biomedical diagnostics* (2002), SPIE Press, Bellingham, WA.

Hartley, C. & Cole, J. (1974), 'An ultrasonic pulsed doppler system for measuring blood flow in small vessels.', *Journal of Applied Physiology* **37**(4), 626–629.

Henken, K. R., Dankelman, J., van den Dobbelsteen, J. J., Cheng, L. K. & van der Heiden, M. S. (2014), 'Error analysis of fbg-based shape sensors for medical needle tracking', *IEEE/ASME Transactions on mechatronics* **19**(5), 1523–1531.

Hennessy, R., Goth, W., Sharma, M., Markey, M. K. & Tunnell, J. W. (2014), 'Effect of probe geometry and optical properties on the sampling depth for diffuse reflectance spectroscopy', *Journal of biomedical optics* **19**(10), 107002–107002.

Hertel, F., Feiden, W. & Bettag, M. (2005), 'The value of micro-doppler in stereotactic brain biopsy', *min-Minimally Invasive Neurosurgery* **48**(03), 165–168.

Hill, K. O. & Meltz, G. (1997), 'Fiber bragg grating technology fundamentals and overview', *Journal of lightwave technology* **15**(8), 1263–1276.

Hochreiter, S. & Schmidhuber, J. (1997), 'Long short-term memory', *Neural computation* **9**(8), 1735–1780.

Huang, C.-H. et al. (2013), 'High-resolution structural and functional assessments of cerebral microvasculature using 3d gas $\delta$r2*-mmra', *PloS one* **8**(11), e78186.

Iordachita, I., Sun, Z., Balicki, M., Kang, J. U., Phee, S. J., Handa, J., Gehlbach, P. & Taylor, R. (2009), 'A sub-millimetric, 0.25 mn resolution fully integrated fiber-optic force-sensing tool for retinal microsurgery', *International journal of computer assisted radiology and surgery* **4**(4), 383–390.

Khadem, M., Rossa, C., Usmani, N., Sloboda, R. S. & Tavakoli, M. (2017), 'Semi-automated needle steering in biological tissue using an ultrasound-based deflection predictor', *Annals of biomedical engineering* **45**(4), 924–938.

Ko, S. Y., Frasson, L. & y Baena, F. R. (2011), 'Closed-loop planar motion control of a steerable probe with a programmable bevel inspired by nature', *IEEE Transactions on Robotics* **27**(5), 970–983.

Ko, S. Y. & Rodriguez y Baena, F. (2013), 'Toward a miniaturized needle steering system

with path planning for obstacle avoidance', *IEEE Transactions on Biomedical Engineering* **60**(4), 910–7.

Ko, S. Y. & y Baena, F. R. (2013), 'Toward a miniaturized needle steering system with path planning for obstacle avoidance', *IEEE Transactions on Biomedical Engineering* **60**(4), 910–917.

Krieger, A., Iordachita, I. I., Guion, P., Singh, A. K., Kaushal, A., Ménard, C., Pinto, P. A., Camphausen, K., Fichtinger, G. & Whitcomb, L. L. (2011), 'An mri-compatible robotic system with hybrid tracking for mri-guided prostate intervention', *IEEE Transactions on Biomedical Engineering* **58**(11), 3049–3060.

Kruth, J., Vandenbroucke, B., Van Vaerenbergh, J. & Mercelis, P. (2005), 'Benchmarking of different sls/slm processes as rapid manufacturing techniques', *Laser* **1**, 3D.

Kvernmo, H. D., Stefanovska, A., Bracic, M., Kirkebøen, K. A. & Kvernebo, K. (1998), 'Spectral analysis of the laser doppler perfusion signal in human skin before and after exercise', *Microvascular research* **56**(3), 173–182.

Kwoh, Y. S., Hou, J., Jonckheere, E. A. & Hayati, S. (1988), 'A robot with improved absolute positioning accuracy for ct guided stereotactic brain surgery', *IEEE Transactions on Biomedical Engineering* **35**(2), 153–160.

Larsson, M., Steenbergen, W. & Strömberg, T. (2002), 'Influence of optical properties and fiber separation on laser doppler flowmetry', *Journal of Biomedical Optics* **7**(2), 236–244.

Lehmann, T., Rossa, C., Usmani, N., Sloboda, R. S. & Tavakoli, M. (2018), 'Intraoperative tissue youngs modulus identification during needle insertion using a laterally actuated needle', *IEEE Transactions on Instrumentation and Measurement* **67**(2), 371–381.

Leibinger, A. (2016), Investigation of tool-tissue interactions for application to surgical needle insertion, PhD thesis, Imperial College London.

Leibinger, A., Burrows, C., Oldfield, M. J. & y Baena, F. R. (2015), 'Tissue motion due to needle deflection', pp. 1873–1876.

Leibinger, A., Oldfield, M. J. & y Baena, F. R. (2016), 'Minimally disruptive needle insertion: a biologically inspired solution', *Interface focus* **6**(3), 20150107.

Leibinger, A., Oldfield, M. & y Baena, F. R. (2014), Multi-objective design optimization for a steerable needle for soft tissue surgery, *in* 'The 15th International Conference on Biomedical Engineering', Springer, pp. 420–423.

Li, M., Li, G., Gonenc, B., Duan, X. & Iordachita, I. (2017), 'Towards human-controlled, real-time shape sensing based flexible needle steering for mri-guided percutaneous therapies', *The International Journal of Medical Robotics and Computer Assisted Surgery* **13**(2).

Li, P., Jiang, S., Liang, D., Yang, Z., Yu, Y. & Wang, W. (2017), 'Modeling of path planning and needle steering with path tracking in anatomical soft tissues for minimally invasive surgery', *Medical Engineering and Physics* **41**, 35–45.

Li, Q. H., Zamorano, L., Pandya, A., Perez, R., Gong, J. & Diaz, F. (2002), 'The application accuracy of the neuromate robota quantitative comparison with frameless and frame-based surgical localization systems', *Computer Aided Surgery* **7**(2), 90–98.

Liang, C.-P., Wierwille, J., Moreira, T., Schwartzbauer, G., Jafri, M. S., Tang, C.-M. & Chen, Y. (2011), 'A forward-imaging needle-type oct probe for image guided stereotactic procedures', *Optics express* **19**(27), 26283–26294.

Liang, C.-P., Wu, Y., Schmitt, J., Bigeleisen, P. E., Slavin, J., Jafri, M. S., Tang, C.-M. & Chen, Y. (2013), 'Coherence-gated doppler: a fiber sensor for precise localization of blood flow', *Biomedical optics express* **4**(5), 760–771.

Liebert, A., Leahy, M. & Maniewski, R. (1998), 'Multichannel laser-doppler probe for blood perfusion measurements with depth discrimination', *Medical and Biological Engineering and Computing* **36**(6), 740–747.

Light, E. D., Mukundan, S., Wolf, P. D. & Smith, S. W. (2007), 'Real-time 3-d intracranial ultrasound with an endoscopic matrix array transducer', *Ultrasound in Medicine and Biology* **33**(8), 1277–1284.

Lipton, Z. C., Berkowitz, J. & Elkan, C. (2015), 'A critical review of recurrent neural networks for sequence learning', *arXiv preprint arXiv:1506.00019* .

Majewicz, A., Siegel, J. J., Stanley, A. A. & Okamura, A. M. (2014), Design and evaluation of duty-cycling steering algorithms for robotically-driven steerable needles, *in* 'Robotics and Automation (ICRA), 2014 IEEE International Conference on', IEEE, pp. 5883–5888.

Majewicz, A., Wedlick, T. R., Reed, K. B. & Okamura, A. M. (2010), Evaluation of robotic needle steering in ex vivo tissue, *in* 'Robotics and Automation (ICRA), 2010 IEEE International Conference on', IEEE, pp. 2068–2073.

Maresca, P., Gómez, E., Caja, J., Barajas, C. & Berzal, M. (2012), A proposal for the metrological characterization of circular features with digital optical machines, *in* 'AIP Conference Proceedings', Vol. 1431, AIP, pp. 158–168.

Markwardt, N. A., Stepp, H., Franz, G., Sroka, R., Goetz, M., Zelenkov, P. & Rühm, A. (2017), 'Remission spectrometry for blood vessel detection during stereotactic biopsy of brain tumors', *Journal of biophotonics* **10**(8), 1080–1094.

Matheson, E., Secoli, R., Burrows, C., Leibinger, A. & Rodriguez y Baena, F. (2018), 'Cyclic motion control for programmable bevel-tip needles to reduce tissue deformation', *Journal of Medical Robotics Research* p. 1842001.

McPhillips, R., Qiu, Z., Jiang, Y., Mahboob, S. O., Wang, H., Meggs, C., Schiavone, G., Sanmartin, D. R., Eljamel, S., Desmulliez, M. P. et al. (2015), Ex-vivo navigation of neurosurgical biopsy needles using microultrasound transducers with m-mode imaging, *in* 'Ultrasonics Symposium (IUS), 2015 IEEE International', IEEE, pp. 1–4.

Mercelis, P. & Kruth, J.-P. (2006), 'Residual stresses in selective laser sintering and selective laser melting', *Rapid prototyping journal* **12**(5), 254–265.

Miga, M. I. (2016), 'Computational modeling for enhancing soft tissue image guided surgery: an application in neurosurgery', *Annals of biomedical engineering* **44**(1), 128–138.

Misra, S., Reed, K. B., Schafer, B. W., Ramesh, K. & Okamura, A. M. (2010), 'Mechanics of flexible needles robotically steered through soft tissue', *The International journal of robotics research* **29**(13), 1640–1660.

Moreira, P. & Misra, S. (2015), 'Biomechanics-based curvature estimation for ultrasound-guided flexible needle steering in biological tissues', *Annals of biomedical engineering* **43**(8), 1716–1726.

Moylan, S., Slotwinski, J., Cooke, A., Jurrens, K. & Donmez, M. A. (2012), Proposal for a standardized test artifact for additive manufacturing machines and processes, *in* 'Proceedings of the 2012 annual international solid freeform fabrication symposium', Austin, TX, pp. 6–8.

Mumtaz, K., Vora, P. & Hopkinson, N. (2011), A method to eliminate anchors/supports from directly laser melted metal powder bed processes, *in* 'Proc. Solid Freeform Fabrication Symposium', Sheffield, pp. 55–64.

Neubach, Z. & Shoham, M. (2010), 'Ultrasound-guided robot for flexible needle steering', *IEEE Transactions on Biomedical Engineering* **57**(4), 799–805.

Öberg, P. Å. (1999), 'Tissue motion - a disturbance in the laser-doppler blood flow signal?', *Technology and Health Care* **7**(2-3), 185–92.

Okamura, A. M., Simone, C. & O'leary, M. D. (2004), 'Force modeling for needle insertion into soft tissue', *IEEE transactions on biomedical engineering* **51**(10), 1707–1716.

Oldfield, M., Burrows, C., Kerl, J., Frasson, L., Parittotokkaporn, T., Beyrau, F. & Rodriguez y Baena, F. (2014), 'Highly resolved strain imaging during needle insertion: results with a novel biologically inspired device', *Journal of the mechanical behavior of biomedical materials* **30**, 50–60.

Oldfield, M. J., Leibinger, A., Seah, T. E. T. & y Baena, F. R. (2015), 'Method to Reduce Target Motion Through NeedleTissue Interactions', *Annals of biomedical engineering* .

Parittotokkaporn, T. (2011), A Novel Bio-Inspired Insertion Method for Application to Next Generation Percutaneous Surgical Tools, PhD thesis, Imperial College London.

Patel, N. K., Plaha, P. & Gill, S. S. (2007), 'Magnetic resonance imaging-directed method for functional neurosurgery using implantable guide tubes', *Operative Neurosurgery* **61**(suppl_5), ONS358–ONS366.

Patil, S., Burgner, J., Webster, R. J. & Alterovitz, R. (2014), 'Needle steering in 3-d via rapid replanning', *IEEE Transactions on Robotics* **30**(4), 853–864.

Peters, T. & Cleary, K. (2008), *Image-guided interventions: technology and applications*, Springer Science & Business Media.

Pichette, J., Goyette, A., Picot, F., Tremblay, M.-A., Soulez, G., Wilson, B. C. & Leblond, F. (2015*a*), 'Sensitivity analysis aimed at blood vessels detection using interstitial optical tomography during brain needle biopsy procedures', *Biomedical optics express* **6**(11), 4238–4254.

Pichette, J., Goyette, A., Picot, F., Tremblay, M.-A., Soulez, G., Wilson, B. C. & Leblond, F. (2015*b*), 'Sensitivity analysis aimed at blood vessels detection using interstitial optical tomography during brain needle biopsy procedures', *Biomedical optics express* **6**(11), 4238–4254.

Piechnik, S. K., Chiarelli, P. A. & Jezzard, P. (2008), 'Modelling vascular reactivity to investigate the basis of the relationship between cerebral blood volume and flow under co2 manipulation', *Neuroimage* **39**(1), 107–118.

Pinggera, D. et al. (2017), 'Serious tumor seeding after brainstem biopsy and its treatmenta case report and review of the literature', *Acta neurochirurgica* **159**(4), 751–754.

Podoleanu, A. G. (2005), 'Optical coherence tomography', *The British journal of radiology* **78**(935), 976–988.

Proctor, M. R. & Black, P. M. (2005), *Minimally invasive neurosurgery*, Springer.

Qin, Y., Brockett, A., Ma, Y., Razali, A., Zhao, J., Harrison, C., Pan, W., Dai, X. & Loziak, D. (2010), 'Micro-manufacturing: research, technology outcomes and development issues', *The International Journal of Advanced Manufacturing Technology* **47**(9-12), 821–837.

Quicke, D. L. J. (2014), *The Braconid and Ichneumonid Parasitoid Wasps: Biology, Systematics, Evolution and Ecology*, web edn, Wiley-Blackwell.

Quigg, M. & Harden, C. (2014), 'Minimally invasive techniques for epilepsy surgery: stereotactic radiosurgery and other technologies: A review', *Journal of neurosurgery* **121**(Suppl 2), 232–240.

Rajan, V., Varghese, B., van Leeuwen, T. G. & Steenbergen, W. (2009), 'Review of methodological developments in laser doppler flowmetry', *Lasers in medical science* **24**(2), 269–283.

Reed, K. B., Okamura, A. M. & Cowan, N. J. (2009), 'Modeling and control of needles with torsional friction', *IEEE transactions on biomedical engineering* **56**(12), 2905–2916.

Reimers, N. & Gurevych, I. (2017), 'Optimal hyperparameters for deep lstm-networks for sequence labeling tasks', *arXiv preprint arXiv:1707.06799* .

Robert, A. L., Chagnon, G., Bricault, I., Cinquin, P. & Moreau-Gaudry, A. (2013), 'A generic three-dimensional static force distribution basis for a medical needle inserted into soft tissue', *Journal of the mechanical behavior of biomedical materials* **28**, 156–170.

Roesthuis, R. J., Kemp, M., van den Dobbelsteen, J. J. & Misra, S. (2014), 'Three-dimensional needle shape reconstruction using an array of fiber bragg grating sensors', *IEEE/ASME transactions on mechatronics* **19**(4), 1115–1126.

Rosenbluth, K. H., Luz, M., Mohr, E., Mittermeyer, S., Bringas, J. & Bankiewicz, K. S. (2011), 'Design of an in-dwelling cannula for convection-enhanced delivery', *Journal of neuroscience methods* **196**(1), 118–123.

Rossa, C., Lehmann, T., Sloboda, R., Usmani, N. & Tavakoli, M. (2017), 'A data-driven soft sensor for needle deflection in heterogeneous tissue using just-in-time modelling', *Medical & biological engineering & computing* **55**(8), 1401–1414.

Rossa, C. & Tavakoli, M. (2017), 'Issues in closed-loop needle steering', *Control Engineering Practice* **62**, 55–69.

Rucker, D. C., Das, J., Gilbert, H. B., Swaney, P. J., Miga, M. I., Sarkar, N. & Webster, R. J. (2013), 'Sliding mode control of steerable needles', *IEEE Transactions on Robotics* **29**(5), 1289–1299.

Sakes, A., Dodou, D. & Breedveld, P. (2016), 'Buckling prevention strategies in nature as inspiration for improving percutaneous instruments: a review', *Bioinspiration & biomimetics* **11**(2), 021001.

Schiavone, G., Jones, T., Price, D., McPhillips, R., Jiang, Y., Qiu, Z., Meggs, C., Mahboob, S. O., Eljamel, S., Button, T. W. et al. (2017), 'A highly compact packaging concept for ultrasound transducer arrays embedded in neurosurgical needles', *Microsystem Technologies* **23**(9), 3881–3891.

Secoli, R., Rodriguez, F. et al. (2018), Experimental validation of curvature tracking with a programmable bevel-tip steerable needle, *in* 'Medical Robotics (ISMR), 2018 International Symposium on', IEEE, pp. 1–6.

Seifabadi, R., Aalamifar, F., Iordachita, I. & Fichtinger, G. (2016), 'Toward teleoperated needle steering under continuous mri guidance for prostate percutaneous interventions', *The International Journal of Medical Robotics and Computer Assisted Surgery* **12**(3), 355–369.

Shahriari, N., Heerink, W., van Katwijk, T., Hekman, E., Oudkerk, M. & Misra, S. (2017), 'Computed tomography (ct)-compatible remote center of motion needle steering robot: Fusing ct images and electromagnetic sensor data', *Medical Engineering and Physics* **45**, 71–77.

Shahriari, N., Hekman, E., Oudkerk, M. & Misra, S. (2015), 'Design and evaluation of a computed tomography (ct)-compatible needle insertion device using an electromagnetic tracking system and ct images', *International journal of computer assisted radiology and surgery* **10**(11), 1845–1852.

Shukla, A. W. & Okun, M. S. (2016), 'State of the art for deep brain stimulation therapy in movement disorders: A clinical and technological perspective', *IEEE reviews in biomedical engineering* **9**, 219–233.

Sillay, K. A., Rusy, D., Buyan-Dent, L., Ninman, N. L. & Vigen, K. K. (2014), 'Wide-bore 1.5 t mri-guided deep brain stimulation surgery: initial experience and technique comparison', *Clinical neurology and neurosurgery* **127**, 79–85.

Sobocki, P., Lekander, I., Berwick, S., Olesen, J. & Jönsson, B. (2006), 'Resource allocation to brain research in europe (rabre)', *European Journal of Neuroscience* **24**(10), 2691–2693.

Su, H., Li, G., Rucker, D. C., Webster, R. J. & Fischer, G. S. (2016), 'A concentric tube continuum robot with piezoelectric actuation for mri-guided closed-loop targeting', *Annals of biomedical engineering* **44**(10), 2863–2873.

Swaney, P. J., Burgner, J., Gilbert, H. B. & Webster, R. J. (2013), 'A flexure-based steerable needle: high curvature with reduced tissue damage', *IEEE Transactions on Biomedical Engineering* **60**(4), 906–909.

Swaney, P. J., Mahoney, A. W., Remirez, A. A., Lamers, E., Hartley, B. I., Feins, R. H., Alterovitz, R. & Webster, R. J. (2015), Tendons, concentric tubes, and a bevel tip: Three steerable robots in one transoral lung access system, *in* 'Robotics and Automation (ICRA), 2015 IEEE International Conference on', IEEE, pp. 5378–5383.

Swensen, J. P., Lin, M., Okamura, A. M. & Cowan, N. J. (2014), 'Torsional dynamics of steerable needles: modeling and fluoroscopic guidance', *IEEE Transactions on Biomedical Engineering* **61**(11), 2707–2717.

Torabi, M., Gupta, R. & Walsh, C. J. (2014), 'Compact robotically steerable image-guided instrument for multi-adjacent-point (map) targeting', *IEEE Transactions on Robotics* **30**(4), 802–815.

Tran, D., Mac, H., Tong, V., Tran, H. A. & Nguyen, L. G. (2018), 'A lstm based framework for handling multiclass imbalance in dga botnet detection', *Neurocomputing* **275**, 2401–2413.

Umemura, A. et al. (2003), 'Deep brain stimulation for movement disorders: morbidity and mortality in 109 patients', *Journal of neurosurgery* **98**(4), 779–784.

Ungersböck, K., Grunert, P., Bohl, J., Müller-Forell, W. & Perneczky, A. (1992), 'Ct-guided stereotactic biopsy aided by doppler ultrasonic vascular monitoring', *Acta neurochirurgica* **115**(3-4), 152–155.

van de Berg, N. J., Dankelman, J. & van den Dobbelsteen, J. J. (2015), 'Design of an actively controlled steerable needle with tendon actuation and fbg-based shape sensing', *Medical engineering & physics* **37**(6), 617–622.

van de Berg, N. J., van Gerwen, D. J., Dankelman, J. & van den Dobbelsteen, J. J. (2015), 'Design choices in needle steeringa review', *IEEE/ASME Transactions on Mechatronics* **20**(5), 2172–2183.

Vayre, B., Vignat, F. & Villeneuve, F. (2012), 'Metallic additive manufacturing: state-of-the-art review and prospects', *Mechanics & Industry* **13**(2), 89–96.

Vincent, J. & King, M. (1995), 'The mechanism of drilling by wood wasp ovipositors', *Biomimetics (USA)* .

Vora, P., Derguti, F., Mumtaz, K., Todd, I. & Hopkinson, N. (2013), Investigating a semi-solid processing technique using metal powder bed additive manufacturing processes, *in* '24th Annual International Solid Freeform Fabrication Symposium-An Additive Manufacturing Conference, Austin, TX, USA'.

Vrooijink, G. J., Abayazid, M., Patil, S., Alterovitz, R. & Misra, S. (2014), 'Needle path planning and steering in a three-dimensional non-static environment using two-dimensional ultrasound images', *The International journal of robotics research* **33**(10), 1361–1374.

Waine, M., Rossa, C., Sloboda, R., Usmani, N. & Tavakoli, M. (2016), 'Three-dimensional needle shape estimation in trus-guided prostate brachytherapy using 2-d ultrasound images', *IEEE journal of biomedical and health informatics* **20**(6), 1621–1631.

Wang, L., Jacques, S. L. & Zheng, L. (1995), 'Mcmlmonte carlo modeling of light transport in multi-layered tissues', *Computer methods and programs in biomedicine* **47**(2), 131–146.

Wårdell, K., Hemm-Ode, S., Rejmstad, P. & Zsigmond, P. (2016), 'High-resolution laser doppler measurements of microcirculation in the deep brain structures: A method for potential vessel tracking', *Stereotactic and functional neurosurgery* **94**(1), 1–9.

Webster, R. J., Kim, J. S., Cowan, N. J., Chirikjian, G. S. & Okamura, A. M. (2006), 'Non-holonomic modeling of needle steering', *The International Journal of Robotics Research* **25**(5-6), 509–525.

Webster, R. J., Memisevic, J. & Okamura, A. M. (2005), Design considerations for robotic needle steering, *in* 'Robotics and Automation, 2005. ICRA 2005. Proceedings of the 2005 IEEE International Conference on', IEEE, pp. 3588–3594.

Webster, R. J., Okamura, A. M. & Cowan, N. J. (2006), Toward active cannulas: Miniature snake-like surgical robots, *in* 'Intelligent Robots and Systems, 2006 IEEE/RSJ International Conference on', IEEE, pp. 2857–2863.

Wedlick, T. R. & Okamura, A. M. (2012), Characterization of robotic needle insertion and rotation in artificial and ex vivo tissues, *in* 'Biomedical Robotics and Biomechatronics (BioRob), 2012 4th IEEE RAS & EMBS International Conference on', IEEE, pp. 62–68.

Weisstein, E. W. (2002*a*), 'Circle-circle tangents'. Last visited on 27/07/2018.
**URL:** *http://mathworld.wolfram.com/Circle-CircleTangents.html*

Weisstein, E. W. (2002*b*), 'Line-line distance'. Last visited on 13/08/2018.
**URL:** *http://mathworld.wolfram.com/Line-LineDistance.html*

Westbrook, P. S., Feder, K., Kremp, T., Taunay, T., Monberg, E., Puc, G. & Ortiz, R. (2015), Multicore optical fiber grating array fabrication for medical sensing applications, *in* 'Optical Fibers and Sensors for Medical Diagnostics and Treatment Applications XV', Vol. 9317, International Society for Optics and Photonics, p. 93170C.

Westebring-Van Der Putten, E., Goossens, R., Jakimowicz, J. & Dankelman, J. (2008), 'Haptics in minimally invasive surgery–a review', *Minimally Invasive Therapy & Allied Technologies* **17**(1), 3–16.

Woodworth, G. F. et al. (2006), 'Frameless image-guided stereotactic brain biopsy procedure: diagnostic yield, surgical morbidity, and comparison with the frame-based technique', *Journal of neurosurgery* **104**(2), 233–237.

Xingjian, S., Chen, Z., Wang, H., Yeung, D.-Y., Wong, W.-K. & Woo, W.-c. (2015), Convolutional lstm network: A machine learning approach for precipitation nowcasting, *in* 'Advances in neural information processing systems', pp. 802–810.

Xu, R., Yurkewich, A. & Patel, R. V. (2016), 'Curvature, torsion, and force sensing in continuum robots using helically wrapped fbg sensors', *IEEE Robotics and Automation Letters* **1**(2), 1052–1059.

Yamasaki, T., Moritake, K., Takaya, M., Kagawa, T., Nagai, H., Akiyama, Y. & Kawahara, M. (1994), 'Intraoperative use of doppler ultrasound and endoscopic monitoring in the stereotactic biopsy of malignant brain tumors', *Journal of neurosurgery* **80**(3), 570–574.

Yaroslavsky, A., Schulze, P., Yaroslavsky, I., Schober, R., Ulrich, F. & Schwarzmaier, H. (2002), 'Optical properties of selected native and coagulated human brain tissues in vitro in the visible and near infrared spectral range', *Physics in Medicine & Biology* **47**(12), 2059.

Yücel, M. A., Selb, J., Aasted, C. M., Lin, P.-Y., Borsook, D., Becerra, L. & Boas, D. A. (2016), 'Mayer waves reduce the accuracy of estimated hemodynamic response functions in functional near-infrared spectroscopy', *Biomedical optics express* **7**(8), 3078–3088.

Zahid Qamar, S. (2018), 'Extrusion of metals, polymers and food products'.

Zaremba, W., Sutskever, I. & Vinyals, O. (2014), 'Recurrent neural network regularization', *arXiv preprint arXiv:1409.2329* .

Zhang, M.-L., Li, Y.-K. & Liu, X.-Y. (2015), Towards class-imbalance aware multi-label learning., *in* 'Proceedings of the Twenty-Fourth International Joint Conference on Artificial Intelligence (IJCAI 2015)', pp. 4041–4047.

Zhang, M.-L., Li, Y.-K., Liu, X.-Y. & Geng, X. (2018), 'Binary relevance for multi-label learning: an overview', *Frontiers of Computer Science* pp. 1–12.

Zhang, M.-L. & Zhou, Z.-H. (2014), 'A review on multi-label learning algorithms', *IEEE transactions on knowledge and data engineering* **26**(8), 1819–1837.

Zhou, Q., Xu, X., Gottlieb, E. J., Sun, L., Cannata, J. M., Ameri, H., Humayun, M. S., Han, P. & Shung, K. K. (2007), 'Pmn-pt single crystal, high-frequency ultrasonic needle transducers for pulsed-wave doppler application', *IEEE transactions on ultrasonics, ferroelectrics, and frequency control* **54**(3).

# Appendix A

# Obtained Permission

## IOP Publishing LICENSE TERMS AND CONDITIONS

Jul 19, 2018

This is a License Agreement between Mr. Vani Virdyawan ("You") and IOP Publishing ("IOP Publishing") provided by Copyright Clearance Center ("CCC"). The license consists of your order details, the terms and conditions provided by IOP Publishing, and the payment terms and conditions.

**All payments must be made in full to CCC. For payment instructions, please see information listed at the bottom of this form.**

| | |
|---|---|
| License Number | 4377120581231 |
| License date | Jun 06, 2018 |
| Licensed content publisher | IOP Publishing |
| Licensed content title | Bioinspiration |
| Licensed content date | Jan 1, 2006 |
| Type of Use | Thesis/Dissertation |
| Requestor type | Author of requested content |
| Format | Electronic |
| Portion | chapter/article |
| The requesting person/organization is: | Vani Virdyawan/Imperial College London |
| Title or numeric reference of the portion(s) | The whole article |
| Title of the article or chapter the portion is from | Laser Doppler sensing for blood vessel detection with a biologically inspired steerable needle |
| Editor of portion(s) | N/A |
| Author of portion(s) | V Virdyawan, M Oldfield, and F Rodriguez y Baena |
| Volume of serial or monograph. | N/A |
| Issue, if republishing an article from a serial | N/A |
| Page range of the portion | |
| Publication date of portion | 16 February 2018 |
| Rights for | Main product |
| Duration of use | Current edition and up to 5 years |
| Creation of copies for the disabled | no |
| With minor editing privileges | yes |
| For distribution to | U.K. and Commonwealth (excluding Canada) |
| In the following language(s) | Original language of publication |
| With incidental promotional use | no |
| The lifetime unit quantity of new product | Up to 499 |
| Title | Laser Doppler sensing for blood vessel detection with a biologically inspired steerable needle |
| Instructor name | Vani Virdyawan |

| | |
|---|---|
| Institution name | other |
| Expected presentation date | Sep 2018 |
| Billing Type | Invoice |
| Billing Address | Mr. Vani Virdyawan<br>5 Cherrywood Drive<br><br>London, United Kingdom SW15 6DS<br>Attn: Mr. Vani Virdyawan |
| Total (may include CCC user fee) | 0.00 USD |

Terms and Conditions

## TERMS AND CONDITIONS

**The following terms are individual to this publisher:**

These special terms and conditions are in addition to the standard terms and conditions for CCC's Republication Service and, together with those standard terms and conditions, govern the use of the Works.

As the "User" you will make all reasonable efforts to contact the author(s) of the article which the Work is to be reused from, to seek consent for your intended use. Contacting one author who is acting expressly as authorised agent for their co-author(s) is acceptable.

User will reproduce the following wording prominently alongside the Work:

- the source of the Work, including author, article title, title of journal, volume number, issue number (if relevant), page range (or first page if this is the only information available) and date of first publication. This information can be contained in a footnote or reference note; and
- a link back to the article (via DOI); and
- if practicable, and IN ALL CASES for new works published under any of the Creative Commons licences, the words "© IOP Publishing. Reproduced with permission. All rights reserved"

Without the express permission of the author(s) and the Rightsholder of the article from which the Work is to be reused, User shall not use it in any way which, in the opinion of the Rightsholder, could: (i) distort or alter the author(s)' original intention(s) and meaning; (ii) be prejudicial to the honour or reputation of the author(s); and/or (iii) imply endorsement by the author(s) and/or the Rightsholder.

This licence does not apply to any article which is credited to another source and which does not have the copyright line '© IOP Publishing Ltd'. User must check the copyright line of the article from which the Work is to be reused to check that IOP Publishing Ltd has all the necessary rights to be able to grant permission. User is solely responsible for identifying and obtaining separate licences and permissions from the copyright owner for reuse of any such third party material/figures which the Rightsholder is not the copyright owner of. The Rightsholder shall not reimburse any fees which User pays for a republication license for such third party content.

This licence does not apply to any material/figure which is credited to another source in the Rightsholder's publication or has been obtained from a third party. User must check the Version of Record of the article from which the Work is to be reused, to check whether any of the material in the Work is third party material. Third party citations and/or copyright notices and/or permissions statements may not be included in any other version of the article from which the Work is to be reused and so cannot be relied upon by the User. User is solely responsible for identifying and obtaining separate licences and permissions from the copyright owner for reuse of any such third party material/figures where the Rightsholder is not the copyright owner. The Rightsholder shall not reimburse any fees which User pays for a republication license for such third party content.

User and CCC acknowledge that the Rightsholder may, from time to time, make changes or additions to these special terms and conditions without express notification, provided that

these shall not apply to permissions already secured and paid for by User prior to such change or addition.

User acknowledges that the Rightsholder (which includes companies within its group and third parties for whom it publishes its titles) may make use of personal data collected through the service in the course of their business.

If User is the author of the Work, User may automatically have the right to reuse it under the rights granted back when User transferred the copyright in the article to the Rightsholder. User should check the copyright form and the relevant author rights policy to check whether permission is required. If User is the author of the Work and does require permission for proposed reuse of the Work, User should select 'Author of requested content' as the Requestor Type. The Rightsholder shall not reimburse any fees which User pays for a republication license.

If User is the author of the article which User wishes to reuse in User's thesis or dissertation, the republication licence covers the right to include the Accepted Manuscript version (not the Version of Record) of the article. User must include citation details and, for online use, a link to the Version of Record of the article on the Rightsholder's website. User may need to obtain separate permission for any third party content included within the article. User must check this with the copyright owner of such third party content. User may not include the article in a thesis or dissertation which is published by ProQuest. Any other commercial use of User's thesis or dissertation containing the article would also need to be expressly notified in writing to the Rightsholder at the time of request and would require separate written permission from the Rightsholder.

User does not need to request permission for Work which has been published under a CC BY licence. User must check the Version of Record of the CC BY article from which the Work is to be reused, to check whether any of the material in the Work is third party material and so not published under the CC BY licence. User is solely responsible for identifying and obtaining separate licences and permissions from the copyright owner for reuse of any such third party material/figures. The Rightsholder shall not reimburse any fees which User pays for such licences and permissions.

As well as CCC, the Rightsholder shall have the right to bring any legal action that it deems necessary to enforce its rights should it consider that the Work infringes those rights in any way.

For STM Signatories ONLY (as agreed as part of the STM Guidelines)

Any licence granted for a particular edition of a Work will apply also to subsequent editions of it and for editions in other languages, provided such editions are for the Work as a whole in situ and do not involve the separate exploitation of the permitted illustrations or excerpts.

**Other Terms and Conditions:**

**STANDARD TERMS AND CONDITIONS**

1. Description of Service; Defined Terms. This Republication License enables the User to obtain licenses for republication of one or more copyrighted works as described in detail on the relevant Order Confirmation (the "Work(s)"). Copyright Clearance Center, Inc. ("CCC") grants licenses through the Service on behalf of the rightsholder identified on the Order Confirmation (the "Rightsholder"). "Republication", as used herein, generally means the inclusion of a Work, in whole or in part, in a new work or works, also as described on the Order Confirmation. "User", as used herein, means the person or entity making such republication.

2. The terms set forth in the relevant Order Confirmation, and any terms set by the Rightsholder with respect to a particular Work, govern the terms of use of Works in connection with the Service. By using the Service, the person transacting for a republication license on behalf of the User represents and warrants that he/she/it (a) has been duly authorized by the User to accept, and hereby does accept, all such terms and conditions on behalf of User, and (b) shall inform User of all such terms and conditions. In the event such person is a "freelancer" or other third party independent of User and CCC, such party shall be deemed jointly a "User" for purposes of these terms and conditions. In any event, User shall be deemed to have accepted and agreed to all such terms and conditions if User republishes the Work in any fashion.

**3. Scope of License; Limitations and Obligations.**

3.1 All Works and all rights therein, including copyright rights, remain the sole and exclusive property of the Rightsholder. The license created by the exchange of an Order Confirmation (and/or any invoice) and payment by User of the full amount set forth on that document includes only those rights expressly set forth in the Order Confirmation and in these terms and conditions, and conveys no other rights in the Work(s) to User. All rights not expressly granted are hereby reserved.

3.2 General Payment Terms: You may pay by credit card or through an account with us payable at the end of the month. If you and we agree that you may establish a standing account with CCC, then the following terms apply: Remit Payment to: Copyright Clearance Center, 29118 Network Place, Chicago, IL 60673-1291. Payments Due: Invoices are payable upon their delivery to you (or upon our notice to you that they are available to you for downloading). After 30 days, outstanding amounts will be subject to a service charge of 1-1/2% per month or, if less, the maximum rate allowed by applicable law. Unless otherwise specifically set forth in the Order Confirmation or in a separate written agreement signed by CCC, invoices are due and payable on “net 30” terms. While User may exercise the rights licensed immediately upon issuance of the Order Confirmation, the license is automatically revoked and is null and void, as if it had never been issued, if complete payment for the license is not received on a timely basis either from User directly or through a payment agent, such as a credit card company.

3.3 Unless otherwise provided in the Order Confirmation, any grant of rights to User (i) is “one-time” (including the editions and product family specified in the license), (ii) is non-exclusive and non-transferable and (iii) is subject to any and all limitations and restrictions (such as, but not limited to, limitations on duration of use or circulation) included in the Order Confirmation or invoice and/or in these terms and conditions. Upon completion of the licensed use, User shall either secure a new permission for further use of the Work(s) or immediately cease any new use of the Work(s) and shall render inaccessible (such as by deleting or by removing or severing links or other locators) any further copies of the Work (except for copies printed on paper in accordance with this license and still in User's stock at the end of such period).

3.4 In the event that the material for which a republication license is sought includes third party materials (such as photographs, illustrations, graphs, inserts and similar materials) which are identified in such material as having been used by permission, User is responsible for identifying, and seeking separate licenses (under this Service or otherwise) for, any of such third party materials; without a separate license, such third party materials may not be used.

3.5 Use of proper copyright notice for a Work is required as a condition of any license granted under the Service. Unless otherwise provided in the Order Confirmation, a proper copyright notice will read substantially as follows: “Republished with permission of [Rightsholder’s name], from [Work's title, author, volume, edition number and year of copyright]; permission conveyed through Copyright Clearance Center, Inc. ” Such notice must be provided in a reasonably legible font size and must be placed either immediately adjacent to the Work as used (for example, as part of a by-line or footnote but not as a separate electronic link) or in the place where substantially all other credits or notices for the new work containing the republished Work are located. Failure to include the required notice results in loss to the Rightsholder and CCC, and the User shall be liable to pay liquidated damages for each such failure equal to twice the use fee specified in the Order Confirmation, in addition to the use fee itself and any other fees and charges specified.

3.6 User may only make alterations to the Work if and as expressly set forth in the Order Confirmation. No Work may be used in any way that is defamatory, violates the rights of third parties (including such third parties' rights of copyright, privacy, publicity, or other tangible or intangible property), or is otherwise illegal, sexually explicit or obscene. In addition, User may not conjoin a Work with any other material that may result in damage to the reputation of the Rightsholder. User agrees to inform CCC if it becomes aware of any infringement of any rights in a Work and to cooperate with any reasonable request of CCC or the Rightsholder in connection therewith.

4. Indemnity. User hereby indemnifies and agrees to defend the Rightsholder and CCC, and their respective employees and directors, against all claims, liability, damages, costs and expenses, including legal fees and expenses, arising out of any use of a Work beyond the

scope of the rights granted herein, or any use of a Work which has been altered in any unauthorized way by User, including claims of defamation or infringement of rights of copyright, publicity, privacy or other tangible or intangible property.

5. Limitation of Liability. UNDER NO CIRCUMSTANCES WILL CCC OR THE RIGHTSHOLDER BE LIABLE FOR ANY DIRECT, INDIRECT, CONSEQUENTIAL OR INCIDENTAL DAMAGES (INCLUDING WITHOUT LIMITATION DAMAGES FOR LOSS OF BUSINESS PROFITS OR INFORMATION, OR FOR BUSINESS INTERRUPTION) ARISING OUT OF THE USE OR INABILITY TO USE A WORK, EVEN IF ONE OF THEM HAS BEEN ADVISED OF THE POSSIBILITY OF SUCH DAMAGES. In any event, the total liability of the Rightsholder and CCC (including their respective employees and directors) shall not exceed the total amount actually paid by User for this license. User assumes full liability for the actions and omissions of its principals, employees, agents, affiliates, successors and assigns.

6. Limited Warranties. THE WORK(S) AND RIGHT(S) ARE PROVIDED “AS IS”. CCC HAS THE RIGHT TO GRANT TO USER THE RIGHTS GRANTED IN THE ORDER CONFIRMATION DOCUMENT. CCC AND THE RIGHTSHOLDER DISCLAIM ALL OTHER WARRANTIES RELATING TO THE WORK(S) AND RIGHT(S), EITHER EXPRESS OR IMPLIED, INCLUDING WITHOUT LIMITATION IMPLIED WARRANTIES OF MERCHANTABILITY OR FITNESS FOR A PARTICULAR PURPOSE. ADDITIONAL RIGHTS MAY BE REQUIRED TO USE ILLUSTRATIONS, GRAPHS, PHOTOGRAPHS, ABSTRACTS, INSERTS OR OTHER PORTIONS OF THE WORK (AS OPPOSED TO THE ENTIRE WORK) IN A MANNER CONTEMPLATED BY USER; USER UNDERSTANDS AND AGREES THAT NEITHER CCC NOR THE RIGHTSHOLDER MAY HAVE SUCH ADDITIONAL RIGHTS TO GRANT.

7. Effect of Breach. Any failure by User to pay any amount when due, or any use by User of a Work beyond the scope of the license set forth in the Order Confirmation and/or these terms and conditions, shall be a material breach of the license created by the Order Confirmation and these terms and conditions. Any breach not cured within 30 days of written notice thereof shall result in immediate termination of such license without further notice. Any unauthorized (but licensable) use of a Work that is terminated immediately upon notice thereof may be liquidated by payment of the Rightsholder's ordinary license price therefor; any unauthorized (and unlicensable) use that is not terminated immediately for any reason (including, for example, because materials containing the Work cannot reasonably be recalled) will be subject to all remedies available at law or in equity, but in no event to a payment of less than three times the Rightsholder's ordinary license price for the most closely analogous licensable use plus Rightsholder's and/or CCC's costs and expenses incurred in collecting such payment.

8. **Miscellaneous.**

8.1 User acknowledges that CCC may, from time to time, make changes or additions to the Service or to these terms and conditions, and CCC reserves the right to send notice to the User by electronic mail or otherwise for the purposes of notifying User of such changes or additions; provided that any such changes or additions shall not apply to permissions already secured and paid for.

8.2 Use of User-related information collected through the Service is governed by CCC’s privacy policy, available online here: http://www.copyright.com/content/cc3/en/tools/footer/privacypolicy.html.

8.3 The licensing transaction described in the Order Confirmation is personal to User. Therefore, User may not assign or transfer to any other person (whether a natural person or an organization of any kind) the license created by the Order Confirmation and these terms and conditions or any rights granted hereunder; provided, however, that User may assign such license in its entirety on written notice to CCC in the event of a transfer of all or substantially all of User’s rights in the new material which includes the Work(s) licensed under this Service.

8.4 No amendment or waiver of any terms is binding unless set forth in writing and signed by the parties. The Rightsholder and CCC hereby object to any terms contained in any writing prepared by the User or its principals, employees, agents or affiliates and purporting to govern or otherwise relate to the licensing transaction described in the Order Confirmation, which terms are in any way inconsistent with any terms set forth in the Order

Confirmation and/or in these terms and conditions or CCC's standard operating procedures, whether such writing is prepared prior to, simultaneously with or subsequent to the Order Confirmation, and whether such writing appears on a copy of the Order Confirmation or in a separate instrument.

8.5 The licensing transaction described in the Order Confirmation document shall be governed by and construed under the law of the State of New York, USA, without regard to the principles thereof of conflicts of law. Any case, controversy, suit, action, or proceeding arising out of, in connection with, or related to such licensing transaction shall be brought, at CCC's sole discretion, in any federal or state court located in the County of New York, State of New York, USA, or in any federal or state court whose geographical jurisdiction covers the location of the Rightsholder set forth in the Order Confirmation. The parties expressly submit to the personal jurisdiction and venue of each such federal or state court.If you have any comments or questions about the Service or Copyright Clearance Center, please contact us at 978-750-8400 or send an e-mail to info@copyright.com.

v 1.1

**Questions? customercare@copyright.com or +1-855-239-3415 (toll free in the US) or +1-978-646-2777.**

Copyright Clearance Center RightsLink®

Home | Account Info | Help

IEEE Requesting permission to reuse content from an IEEE publication

Title: Flexible Needle Steering System for Percutaneous Access to Deep Zones of the Brain

Conference Proceedings: Proceedings of the IEEE 32nd Annual Northeast Bioengineering Conference

Author: J.A. Engh

Publisher: IEEE

Date: 2006

Copyright © 2006, IEEE

Logged in as:
Vani Virdyawan
Account #:
3001235364

LOGOUT

## Thesis / Dissertation Reuse

**The IEEE does not require individuals working on a thesis to obtain a formal reuse license, however, you may print out this statement to be used as a permission grant:**

*Requirements to be followed when using any portion (e.g., figure, graph, table, or textual material) of an IEEE copyrighted paper in a thesis:*

1) In the case of textual material (e.g., using short quotes or referring to the work within these papers) users must give full credit to the original source (author, paper, publication) followed by the IEEE copyright line © 2011 IEEE.
2) In the case of illustrations or tabular material, we require that the copyright line © [Year of original publication] IEEE appear prominently with each reprinted figure and/or table.
3) If a substantial portion of the original paper is to be used, and if you are not the senior author, also obtain the senior author's approval.

*Requirements to be followed when using an entire IEEE copyrighted paper in a thesis:*

1) The following IEEE copyright/ credit notice should be placed prominently in the references: © [year of original publication] IEEE. Reprinted, with permission, from [author names, paper title, IEEE publication title, and month/year of publication]
2) Only the accepted version of an IEEE copyrighted paper can be used when posting the paper or your thesis on-line.
3) In placing the thesis on the author's university website, please display the following message in a prominent place on the website: In reference to IEEE copyrighted material which is used with permission in this thesis, the IEEE does not endorse any of [university/educational entity's name goes here]'s products or services. Internal or personal use of this material is permitted. If interested in reprinting/republishing IEEE copyrighted material for advertising or promotional purposes or for creating new collective works for resale or redistribution, please go to http://www.ieee.org/publications_standards/publications/rights/rights_link.html to learn how to obtain a License from RightsLink.

If applicable, University Microfilms and/or ProQuest Library, or the Archives of Canada may supply single copies of the dissertation.

BACK CLOSE WINDOW

Copyright © 2018 Copyright Clearance Center, Inc. All Rights Reserved. Privacy statement. Terms and Conditions.
Comments? We would like to hear from you. E-mail us at customercare@copyright.com

Copyright Clearance Center RightsLink®

Home Account Info Help

| | |
|---|---|
| **Title:** | Towards human-controlled, real-time shape sensing based flexible needle steering for MRI-guided percutaneous therapies |
| **Author:** | Meng Li, Gang Li, Berk Gonenc, et al |
| **Publication:** | International Journal of Medical Robotics and Computer Assisted Surgery |
| **Publisher:** | John Wiley and Sons |
| **Date:** | Aug 4, 2016 |

Copyright © 2016, John Wiley and Sons

Logged in as:
Vani Virdyawan
Account #: 3001235364
LOGOUT

## Review Order

Please review the order details and the associated terms and conditions.

No royalties will be charged for this reuse request although you are required to obtain a license and comply with the license terms and conditions. To obtain the license, click the Accept button below.

| | |
|---|---|
| Licensed Content Publisher | John Wiley and Sons |
| Licensed Content Publication | International Journal of Medical Robotics and Computer Assisted Surgery |
| Licensed Content Title | Towards human-controlled, real-time shape sensing based flexible needle steering for MRI-guided percutaneous therapies |
| Licensed Content Author | Meng Li, Gang Li, Berk Gonenc, et al |
| Licensed Content Date | Aug 4, 2016 |
| Licensed Content Volume | 13 |
| Licensed Content Issue | 2 |
| Licensed Content Pages | 14 |
| Type of use | Dissertation/Thesis |
| Requestor type | University/Academic |
| Format | Electronic |
| Portion | Figure/table |
| Number of figures/tables | 1 |
| Original Wiley figure/table number(s) | 1 |
| Will you be translating? | No |
| Title of your thesis / dissertation | Sensorisation of a Novel Biologically Inspired Flexible Needle |
| Expected completion date | Sep 2018 |
| Expected size (number of pages) | 170 |
| Requestor Location | Mr. Vani Virdyawan<br>5 Cherrywood Drive<br><br>London, SW15 6DS<br>United Kingdom<br>Attn: Mr. Vani Virdyawan |
| Publisher Tax ID | EU826007151 |
| Total | 0.00 GBP |

Edit Order Details
Edit Requestor Location This location may be used to determine your tax liability.

I agree to these terms and conditions.

I understand this license is for reuse only and that no content is provided.

Customer Code (if supplied) APPLY

BACK DECLINE ACCEPT

Please click accept only once.

Copyright © 2018 Copyright Clearance Center, Inc. All Rights Reserved. Privacy statement. Terms and Conditions.
Comments? We would like to hear from you. E-mail us at customercare@copyright.com

Copyright Clearance Center RightsLink®

Home Account Info Help

KARGER

**Title:** High-Resolution Laser Doppler Measurements of Microcirculation in the Deep Brain Structures: A Method for Potential Vessel Tracking

**Author:** Wårdell Karin, Hemm-Ode Simone, Rejmstad Peter, et al

**Publication:** Stereotactic and Functional Neurosurgery

**Publisher:** Karger Publishers

**Date:** Jan 22, 2016

Copyright © 2016, © 2016 S. Karger AG, Basel

Logged in as:
Vani Virdyawan
Account #:
3001235364

LOGOUT

## Order Completed

Thank you for your order.

This Agreement between Mr. Vani Virdyawan ("You") and Karger Publishers ("Karger Publishers") consists of your license details and the terms and conditions provided by Karger Publishers and Copyright Clearance Center.

Your confirmation email will contain your order number for future reference.

printable details

| | |
|---|---|
| License Number | 4450190264080 |
| License date | Oct 15, 2018 |
| Licensed Content Publisher | Karger Publishers |
| Licensed Content Publication | Stereotactic and Functional Neurosurgery |
| Licensed Content Title | High-Resolution Laser Doppler Measurements of Microcirculation in the Deep Brain Structures: A Method for Potential Vessel Tracking |
| Licensed copyright line | Copyright © 2016, © 2016 S. Karger AG, Basel |
| Licensed Content Author | Wårdell Karin, Hemm-Ode Simone, Rejmstad Peter, et al |
| Licensed Content Date | Jan 22, 2016 |
| Licensed Content Volume | 94 |
| Licensed Content Issue | 1 |
| Special issue or supplement | |
| Type of use | Thesis/Dissertation |
| Requestor type | academic/educational institution |
| Format | Electronic |
| Portion | figures/tables/illustrations |
| Number of figures/tables/illustrations | 1 |
| Include Image file | no |
| Rights for | Main Product and other compilations/derivative products |
| Duration of use | Life of current edition/presentation |
| Creation of copies for the disabled | no |
| With minor editing privileges | yes |
| For distribution to | U.K. and Commonwealth (excluding Canada) |
| Lifetime unit quantity of new product | 100 |
| The requesting person/organization | Vani Virdyawan |

| | |
|---|---|
| Order reference number | |
| Title of your thesis / dissertation | Sensorisation of a Novel Biologically Inspired Flexible Needle |
| Expected completion date | Sep 2018 |
| Estimated size (number of pages) | 170 |
| Requestor Location | Mr. Vani Virdyawan<br>5 Cherrywood Drive<br><br>London, SW15 6DS<br>United Kingdom<br>Attn: Mr. Vani Virdyawan |
| Publisher Tax ID | 980406204 |
| Billing Type | Invoice |
| Billing address | Mr. Vani Virdyawan<br>5 Cherrywood Drive<br><br>London, United Kingdom SW15 6DS<br>Attn: Mr. Vani Virdyawan |
| Total | 0.00 GBP |

ORDER MORE CLOSE WINDOW

Copyright © 2018 Copyright Clearance Center, Inc. All Rights Reserved. Privacy statement. Terms and Conditions.
Comments? We would like to hear from you. E-mail us at customercare@copyright.com

Copyright Clearance Center RightsLink®

Home Account Info Help

| | |
|---|---|
| **Title:** | Real-Time 3-D Intracranial Ultrasound with an Endoscopic Matrix Array Transducer |
| **Author:** | Edward D. Light,Srinivasan Mukundan,Patrick D. Wolf,Stephen W. Smith |
| **Publication:** | Ultrasound in Medicine & Biology |
| **Publisher:** | Elsevier |
| **Date:** | August 2007 |

Copyright © 2007 World Federation for Ultrasound in Medicine & Biology. Published by Elsevier Inc. All rights reserved.

Logged in as:
Vani Virdyawan
Account #: 3001235364
LOGOUT

## Order Completed

Thank you for your order.

This Agreement between Mr. Vani Virdyawan ("You") and Elsevier ("Elsevier") consists of your license details and the terms and conditions provided by Elsevier and Copyright Clearance Center.

Your confirmation email will contain your order number for future reference.

printable details

| | |
|---|---|
| License Number | 4446531415247 |
| License date | Oct 12, 2018 |
| Licensed Content Publisher | Elsevier |
| Licensed Content Publication | Ultrasound in Medicine & Biology |
| Licensed Content Title | Real-Time 3-D Intracranial Ultrasound with an Endoscopic Matrix Array Transducer |
| Licensed Content Author | Edward D. Light,Srinivasan Mukundan,Patrick D. Wolf,Stephen W. Smith |
| Licensed Content Date | Aug 1, 2007 |
| Licensed Content Volume | 33 |
| Licensed Content Issue | 8 |
| Licensed Content Pages | 8 |
| Type of Use | reuse in a thesis/dissertation |
| Portion | figures/tables/illustrations |
| Number of figures/tables/illustrations | 2 |
| Format | electronic |
| Are you the author of this Elsevier article? | No |
| Will you be translating? | No |
| Original figure numbers | figure 1, figure 2.a |
| Title of your thesis/dissertation | Sensorisation of a Novel Biologically Inspired Flexible Needle |
| Publisher of new work | Imperial College London |
| Expected completion date | Sep 2018 |
| Estimated size (number of pages) | 170 |
| Requestor Location | Mr. Vani Virdyawan<br>5 Cherrywood Drive<br><br>London, SW15 6DS<br>United Kingdom<br>Attn: Mr. Vani Virdyawan |
| Publisher Tax ID | GB 494 6272 12 |

| | |
|---|---|
| Total | 0.00 USD |

ORDER MORE CLOSE WINDOW

Copyright © 2018 Copyright Clearance Center, Inc. All Rights Reserved. Privacy statement. Terms and Conditions.
Comments? We would like to hear from you. E-mail us at customercare@copyright.com

Copyright Clearance Center RightsLink®

Home Account Info Help

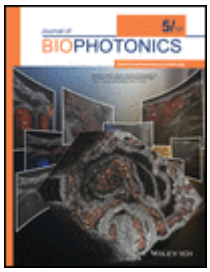

| | |
|---|---|
| **Title:** | Remission spectrometry for blood vessel detection during stereotactic biopsy of brain tumors |
| **Author:** | Niklas A. Markwardt, Herbert Stepp, Gerhard Franz, et al |
| **Publication:** | Journal of Biophotonics |
| **Publisher:** | John Wiley and Sons |
| **Date:** | Oct 7, 2016 |

Copyright © 2016, John Wiley and Sons

Logged in as:
Vani Virdyawan
Account #:
3001235364

LOGOUT

## Order Completed

Thank you for your order.

This Agreement between Mr. Vani Virdyawan ("You") and John Wiley and Sons ("John Wiley and Sons") consists of your license details and the terms and conditions provided by John Wiley and Sons and Copyright Clearance Center.

Your confirmation email will contain your order number for future reference.

printable details

| | |
|---|---|
| License Number | 4446590252812 |
| License date | Oct 12, 2018 |
| Licensed Content Publisher | John Wiley and Sons |
| Licensed Content Publication | Journal of Biophotonics |
| Licensed Content Title | Remission spectrometry for blood vessel detection during stereotactic biopsy of brain tumors |
| Licensed Content Author | Niklas A. Markwardt, Herbert Stepp, Gerhard Franz, et al |
| Licensed Content Date | Oct 7, 2016 |
| Licensed Content Volume | 10 |
| Licensed Content Issue | 8 |
| Licensed Content Pages | 15 |
| Type of use | Dissertation/Thesis |
| Requestor type | University/Academic |
| Format | Electronic |
| Portion | Figure/table |
| Number of figures/tables | 1 |
| Original Wiley figure/table number(s) | Figure 2.c |
| Will you be translating? | No |
| Title of your thesis / dissertation | Sensorisation of a Novel Biologically Inspired Flexible Needle |
| Expected completion date | Sep 2018 |
| Expected size (number of pages) | 170 |
| Requestor Location | Mr. Vani Virdyawan<br>5 Cherrywood Drive<br><br>London, SW15 6DS<br>United Kingdom<br>Attn: Mr. Vani Virdyawan |
| Publisher Tax ID | EU826007151 |

| | |
|---|---|
| Total | 0.00 GBP |

**Would you like to purchase the full text of this article? If so, please continue on to the content ordering system located here: Purchase PDF**

**If you click on the buttons below or close this window, you will not be able to return to the content ordering system.**

ORDER MORE CLOSE WINDOW

Copyright © 2018 Copyright Clearance Center, Inc. All Rights Reserved. Privacy statement. Terms and Conditions.
Comments? We would like to hear from you. E-mail us at customercare@copyright.com

Copyright Clearance Center RightsLink®

Home Create Account Help

IEEE Requesting permission to reuse content from an IEEE publication

**Title:** Ex-vivo navigation of neurosurgical biopsy needles using microultrasound transducers with M-mode imaging

**Conference Proceedings:** 2015 IEEE International Ultrasonics Symposium (IUS)

**Author:** Rachael McPhillips

**Publisher:** IEEE

**Date:** Oct. 2015

Copyright © 2015, IEEE

LOGIN

If you're a copyright.com user, you can login to RightsLink using your copyright.com credentials.

Already a RightsLink user or want to learn more?

## Thesis / Dissertation Reuse

**The IEEE does not require individuals working on a thesis to obtain a formal reuse license, however, you may print out this statement to be used as a permission grant:**

*Requirements to be followed when using any portion (e.g., figure, graph, table, or textual material) of an IEEE copyrighted paper in a thesis:*

1) In the case of textual material (e.g., using short quotes or referring to the work within these papers) users must give full credit to the original source (author, paper, publication) followed by the IEEE copyright line © 2011 IEEE.
2) In the case of illustrations or tabular material, we require that the copyright line © [Year of original publication] IEEE appear prominently with each reprinted figure and/or table.
3) If a substantial portion of the original paper is to be used, and if you are not the senior author, also obtain the senior author's approval.

*Requirements to be followed when using an entire IEEE copyrighted paper in a thesis:*

1) The following IEEE copyright/ credit notice should be placed prominently in the references: © [year of original publication] IEEE. Reprinted, with permission, from [author names, paper title, IEEE publication title, and month/year of publication]
2) Only the accepted version of an IEEE copyrighted paper can be used when posting the paper or your thesis on-line.
3) In placing the thesis on the author's university website, please display the following message in a prominent place on the website: In reference to IEEE copyrighted material which is used with permission in this thesis, the IEEE does not endorse any of [university/educational entity's name goes here]'s products or services. Internal or personal use of this material is permitted. If interested in reprinting/republishing IEEE copyrighted material for advertising or promotional purposes or for creating new collective works for resale or redistribution, please go to http://www.ieee.org/publications_standards/publications/rights/rights_link.html to learn how to obtain a License from RightsLink.

If applicable, University Microfilms and/or ProQuest Library, or the Archives of Canada may supply single copies of the dissertation.

BACK CLOSE WINDOW

Copyright © 2018 Copyright Clearance Center, Inc. All Rights Reserved. Privacy statement. Terms and Conditions.
Comments? We would like to hear from you. E-mail us at customercare@copyright.com

Copyright Clearance Center RightsLink®

Home | Account Info | Help

IEEE Requesting permission to reuse content from an IEEE publication

**Title:** Design Choices in Needle Steering—A Review
**Author:** Nick J. van de Berg
**Publication:** Mechatronics, IEEE/ASME Transactions on
**Publisher:** IEEE
**Date:** Oct. 2015
Copyright © 2015, IEEE

Logged in as:
Vani Virdyawan
Account #: 3001235364
LOGOUT

## Thesis / Dissertation Reuse

**The IEEE does not require individuals working on a thesis to obtain a formal reuse license, however, you may print out this statement to be used as a permission grant:**

*Requirements to be followed when using any portion (e.g., figure, graph, table, or textual material) of an IEEE copyrighted paper in a thesis:*

1) In the case of textual material (e.g., using short quotes or referring to the work within these papers) users must give full credit to the original source (author, paper, publication) followed by the IEEE copyright line © 2011 IEEE.
2) In the case of illustrations or tabular material, we require that the copyright line © [Year of original publication] IEEE appear prominently with each reprinted figure and/or table.
3) If a substantial portion of the original paper is to be used, and if you are not the senior author, also obtain the senior author's approval.

*Requirements to be followed when using an entire IEEE copyrighted paper in a thesis:*

1) The following IEEE copyright/ credit notice should be placed prominently in the references: © [year of original publication] IEEE. Reprinted, with permission, from [author names, paper title, IEEE publication title, and month/year of publication]
2) Only the accepted version of an IEEE copyrighted paper can be used when posting the paper or your thesis on-line.
3) In placing the thesis on the author's university website, please display the following message in a prominent place on the website: In reference to IEEE copyrighted material which is used with permission in this thesis, the IEEE does not endorse any of [university/educational entity's name goes here]'s products or services. Internal or personal use of this material is permitted. If interested in reprinting/republishing IEEE copyrighted material for advertising or promotional purposes or for creating new collective works for resale or redistribution, please go to http://www.ieee.org/publications_standards/publications/rights/rights_link.html to learn how to obtain a License from RightsLink.

If applicable, University Microfilms and/or ProQuest Library, or the Archives of Canada may supply single copies of the dissertation.

BACK CLOSE WINDOW

Copyright © 2018 Copyright Clearance Center, Inc. All Rights Reserved. Privacy statement. Terms and Conditions.
Comments? We would like to hear from you. E-mail us at customercare@copyright.com

**From:** pubscopyright <copyright@osa.org>
**Sent:** 22 October 2018 21:59
**To:** Virdyawan, Vani; pubscopyright
**Subject:** RE: Permission to use Figure at OSA articles

Dear Vani Virdyawan,

Thank you for contacting The Optical Society.

For the use of figure 1 from **[1]** Andréanne Goyette, Julien Pichette, Marie-Andrée Tremblay, Audrey Laurence, Michael Jermyn, Kelvin Mok, Keith D. Paulsen, David W. Roberts, Kevin Petrecca, Brian C. Wilson, and Frédéric Leblond, "Sub-diffuse interstitial optical tomography to improve the safety of brain needle biopsies: a proof-of-concept study," Opt. Lett. 40, 170-173 (2015), figure 1 from **[2]** Chia-Pin Liang, Jeremiah Wierwille, Thais Moreira, Gary Schwartzbauer, M. Samir Jafri, Cha-Min Tang, and Yu Chen, "A forward-imaging needle-type OCT probe for image guided stereotactic procedures," Opt. Express 19, 26283-26294 (2011), and figure 1 from **[3]** Chia-Pin Liang, Yalun Wu, Joe Schmitt, Paul E. Bigeleisen, Justin Slavin, M. Samir Jafri, Cha-Min Tang, and Yu Chen, "Coherence-gated Doppler: a fiber sensor for precise localization of blood flow," Biomed. Opt. Express 4, 760-771 (2013):

> OSA considers your requested use of its copyrighted material to be Fair Use under United States Copyright Law. It is requested that a complete citation of the original material be included in any publication.

While your publisher should be able to provide additional guidance, OSA prefers the below citation formats:

> For citations in figure captions:
>
> [Reprinted/Adapted] with permission from ref [x], [Publisher]. (with full citation in reference list)
>
> For images without captions:
>
> Journal Vol. #, first page (year published) An example: Biomed. Opt. Express 4, 760 (2013)

Please let me know if you have any questions.

Kind Regards,

Rebecca Robinson

Rebecca Robinson
October 22, 2018
Authorized Agent, The Optical Society

**The Optical Society (OSA)**
2010 Massachusetts Ave., NW
Washington, DC 20036 USA
www.osa.org

**Reflecting a Century of Innovation**

OSA The Optical Society | 100 Since 1916

---

**From:** Virdyawan, Vani <v.virdyawan14@imperial.ac.uk>
**Sent:** Friday, October 12, 2018 2:38 PM
**To:** pubscopyright <copyright@osa.org>
**Subject:** Permission to use Figure at OSA articles

Dear OSA Copyright Centre,

I am Vani Virdyawan, a PhD student at Imperial College London, United Kingdom. Currently, I am writing my PhD Thesis, entitle Sensorisation of a Novel Biologically Inspired Flexible Needle. The thesis will be in an electronic format.

For my PhD thesis, I need to reuse figures from the following articles:

1. Title: Sub-diffuse interstitial optical tomography to improve the safety of brain needle biopsies: a proof-of-concept study
   Author: Andréanne Goyette,et. al.
   Journal: Optics Letters, Vol. 40, No.2 January 15, 2015
   Figure: Figure 1
2. Title: A forward-imaging needle-type OCT probe for image guided stereotactic procedures
   Author: Chia-Pin Liang, et. al.
   Journal: Optics Express Vol. 19 Issue 27, pp. pp. 26283-26294 (2011)
   Figure: Figure 1
3. Title: Coherence-gated Doppler: a fiber sensor for precise localization of blood flow
   Author: Chia-Pin Liang, et. al.
   Journal: Biomedical Optics Express Vol. 4, Issue 5, pp. 760-771 (2013)
   Figure: Figure 1.b

Could you grant me the permission for using above mentioned figures?

Thank you

Regards,

Vani Virdyawan
Mechanical Engineering
Imperial College London